

Report No. CDOH-DTD-R-94-12

**Dynamic Measurements  
on Penetrometers for Determination  
of Foundation Design**

G. G. Goble  
Hasan Aboumatar  
University of Colorado  
Boulder, CO 80309

Final Report  
November 1994

Prepared in cooperation with the  
U.S. Department of Transportation  
Federal Highway Administration

The contents of this report reflect the views of authors who are responsible for the facts and the accuracy of the data presented herein. The contents do not necessarily reflect the official views of the Colorado Department of Transportation or the Federal Highway Administration. This report does not constitute a standard, specification, or regulation.

**Technical Report Documentation Page**

1. Report No. CDOH-DTD-R-94		2. Government Accession No.		3. Recipient's Catalog No.	
4. Title and Subtitle DYNAMIC MEASUREMENTS ON PENETROMETERS FOR DETERMINATION OF FOUNDATION DESIGN PARAMETERS				5. Report Date November, 1994	
				6. Performing Organization Code HPR-1488A/ 72.56	
7. Author(s) G. G. Goble, Hasan Aboumatar				8. Performing Organization Rpt.No. CDOH-DTD-R-94	
9. Performing Organization Name and Address University of Colorado Dept. of Civil, Envir. & Arch. Engrg. Boulder, CO 80309-0428				10. Work Unit No. (TRAI5)	
				11. Contract or Grant No. HPR 1488A	
12. Sponsoring Agency Name and Address Colorado Department of Transportation 4201 East Arkansas Avenue Denver, CO 80222				13. Type of Rpt. and Period Covered Final Report	
				14. Sponsoring Agency Code 270.01	
15. Supplementary Notes Prepared in Cooperation with the U.S. Department of Transportation, Federal Highway Administration					
16. Abstract  <p><b>The historical background of the Standard Penetration Test (SPT) is reviewed with particular emphasis of those efforts to make dynamic measurements during the driving operation. The mechanics of one dimensional wave propagation is reviewed with emphasis on those aspects of the theory that applies to SPT operations. During the course of the project it was discovered that the accuracy of measurements produced by available accelerometers was questionable. A major effort was devoted to testing accelerometers in the laboratory and evaluating the results. A wave of mechanics analysis of both the Safety Hammer and the CME Automatic Hammer is presented and shown to agree closely with measurements. The conclusion was reached that the measurement system is now accurate and reasonably reliable.</b></p> <p><b>Measurements were made at field sites to evaluate the ability to calculate Wave Equations soil constants. Force and motion was calculated at the sampler from the top measurements. Results are presented for two different conditions. These results must be considered as preliminary, but they offer justification for optimism in the future use of the method.</b></p>					
17. Key Words dynamic, response, acceleration, force, SPT			18. Distribution Statement No Restrictions: This report is available to the public through the National Information Service. Springfield, VA 22161		
19. Security Classif. (report) Unclassified		20. Security Classif. (page) Unclassified		21. No. of Pages 140	22. Price

## Contents

I	INTRODUCTION	1
1.1	Introduction . . . . .	1
1.2	Scope and Objective . . . . .	2
II	REVIEW OF PREVIOUS WORK	4
2.1	Standard Penetration Test . . . . .	4
2.2	History of the SPT . . . . .	6
2.3	Uses of the SPT . . . . .	7
2.4	Reliability of Blow Count of the SPT . . . . .	15
2.5	Energy Measurements . . . . .	16
2.6	Computation of Bottom Velocity, Displacement and Reaction Force .	18
III	WAVE PROPAGATION IN THE SPT	22
3.1	One Dimensional Wave Mechanics . . . . .	22
3.1.1	Boundary Conditions . . . . .	23
3.1.2	Discontinuity in Bar Properties . . . . .	24
3.2	Proportionality of Force and Velocity . . . . .	25
3.3	Generation of Waves in the SPT Procedure . . . . .	28
3.3.1	Generation of Waves in the Rod . . . . .	28
IV	MEASURING AND PROCESSING EQUIPMENT	37

	ii
4.1 Introduction . . . . .	37
4.2 Transducer Description . . . . .	38
4.3 Data Processing . . . . .	42
4.4 Dynamic Calibration . . . . .	51
4.5 Frequency Response. . . . .	57
V EVALUATION OF RESULTS	66
5.1 Laboratory Tests . . . . .	66
5.1.1 Energy Absorbed by Soil . . . . .	70
5.2 Field Tests . . . . .	73
5.2.1 Stress Peak Evaluation . . . . .	81
5.2.2 Bottom Analysis . . . . .	86
VI CONCLUSIONS AND DISCUSSION	92
REFERENCES	94
APPENDIX A ONE DIMENSIONAL STRESS WAVE MECHANICS IN A ROD UNDER IMPACT	96
APPENDIX B ACCELEROMETER CALIBRATION FACTOR	119

**List of Tables**

2.1	Relative Density of Sand . . . . .	8
2.2	Consistency of Cohesive Soil . . . . .	8
4.1	Specifications for Model EGCS-240D Entran Accelerometer, Supplied by Entran. . . . .	43

## List of Figures

2.1	A typical split-spoon sampler by ASTM D1586-67. . . . .	5
2.2	Correlation Between SPT Blow Count and Relative Density of Cohesionless Soils as Given by Gibbs, Holtz and Bazarra. . . . .	9
2.3	Estimation of $\phi$ (Angle of Internal Friction) from the SPT Blow Count. (After Schmertmann) . . . . .	10
2.4	Empirical Relation between Ultimate Point Resistance of Piles and Standard Penetration Resistance in Cohesionless Soil (1 tsf = 95.8 kn/m <sup>2</sup> ) . . . . .	12
2.5	Empirical Relation between Ultimate Skin Friction of Piles and Standard Penetration Resistance in Cohesionless Soil (1 tsf = 95.8 kn/m <sup>2</sup> )	13
2.6	Correlation between Stress Ratio Causing Liquefaction in Field and Penetration Resistance of Sand. . . . .	14
2.7	Schematic of First Compression Wave Reflecting at Sampler and Then at Hammer.(after Schmertmann and Palacios) . . . . .	19
3.1	Proportionality of Force and Velocity . . . . .	27
3.2	Safety Hammer and Drill Rod, with Dimensions . . . . .	29
3.3	Schematic of a Blow in the SPT with Safety Hammer . . . . .	31
3.4	Wave Propagation in the Safety Hammer System . . . . .	32
3.5	Theoretical Wave form Against Experimental Data. . . . .	36

4.1	Strain Gages Layout. . . . .	39
4.2	Static Calibration of the Force Measuring Device Using the MTS Testing Machine. . . . .	40
4.3	Static Calibration Results of Force Measuring Device for AW-rod. . . . .	41
4.4	Flowchart for Processing Program. . . . .	45
4.5	Plot of Force, Velocity and Energy of a Record Taken in the Laboratory Using the R.C. Data Acquisition System. . . . .	46
4.6	Plot of Force and Velocity Record Taken Through the PDA. . . . .	48
4.7	Radar and the Hammer Performance Analyzer. . . . .	50
4.8	Impact Velocity Measurement During an SPT Field Testing. . . . .	50
4.9	Drawing of the Pendulum Test Setup. . . . .	52
4.10	Wave Propagation in the Pendulum Test Performance. . . . .	54
4.11	Theoretical Form of Stress and Velocity Waves in the Pendulum Test Performance. . . . .	55
4.12	Measurement of the Impact Velocity. . . . .	56
4.13	Stress and Velocity Records in Comparison with the Theoretical Form. . . . .	56
4.14	Stress and Velocity Waves Using the New Calibration Constants. . . . .	58
4.15	Calibration Curve of the M437 Accelerometer. . . . .	61
4.16	Calibration Curve of the M438 Accelerometer. . . . .	62
4.17	Comparison Between Theoretical and Experimental Data of the M437 Calibration curve. . . . .	63
4.18	Comparison Between Theoretical and Experimental Data of the M438 Calibration curve. . . . .	63
4.19	Flowchart for the Frequency Domain Processing Program. . . . .	64

4.20 Comparison Between the Velocity Calculated Using the Calibration Function and the Velocity Calculated Using the Calibration Factor . . .	65
5.1 Drawing of the Laboratory Testing Setup . . . . .	67
5.2 Laboratory Test Results, Test # 1 . . . . .	69
5.3 Laboratory Test Results, Test # 2 . . . . .	69
5.4 Comparison Between the Actual Rod and the Free Rod Solution . .	71
5.5 Comparison Between Calculated and Measured Bottom Reaction . .	71
5.6 Bottom Velocity and Comparison Between Calculated and Measured Displacement . . . . .	72
5.7 Force, Velocity and Energy Obtained from Top Transducers . . . . .	74
5.8 Superposed Force Records . . . . .	74
5.9 Superposed Velocity Records . . . . .	75
5.10 Force, Velocity and Energy Obtained from the Reflected Wave . . .	75
5.11 Calculation of the Energy absorbed by the Soil . . . . .	76
5.12 Picture of the Data Acquisition Systems Used in the Field Tests. . .	77
5.13 Field Test # 10, Blow No. 50, Length Below Gages is 77.5 ft, Taken Through the RC During the CME Automatic Hammer test, June 1990.	79
5.14 Field Test # 10, Blow No. 128, Length Below Gages is 77.5 ft, Taken Through the RC During the CME Automatic Hammer test, June 1990.	79
5.15 Field Test # 8, Blow No. 5, Length Below Gages is 47.5 ft, Taken Through the RC During the CME Automatic Hammer test, June 1990.	80
5.16 Field Test # 8, Blow No. 9, Length Below Gages is 82.5 ft, Taken Through the PDA During the Pilcon Hammer test, August 1990. . . .	80
5.17 Effect of Using One Accelerometer Instead of Two. . . . .	82

5.18	Dimensions of the CME Automatic Hammer System. . . . .	84
5.19	Wave Propagation in the CME Hammer System. . . . .	85
5.20	Bottom Resistance for the Blow Taken in the Sandy Clay Soil . . . .	87
5.21	Bottom Resistance for the Blow Taken in the Soft Rock Strata . . .	87
5.22	Bottom Velocity and Displacement for the Blow in the Sandy Clay .	88
5.23	Bottom Velocity and Displacement for the Blow in the Soft Rock . .	88
5.24	Bottom Reaction Versus Displacement for the Record Taken in the Sandy Clay Soil . . . . .	89
5.25	Bottom Reaction Versus Displacement for the Record Taken in the Soft Rock . . . . .	89
5.26	Energy Delivered to the Soil for the Record Taken in the Soft Rock .	92
A.1	Derivation of Wave Equation. . . . .	97
A.2	Reflection of Displacement and Stress Waves at Free End . . . . .	102
A.3	Reflection of Displacement and Stress Waves at Fixed End . . . . .	104
A.4	Impact Force Applied at an Intermediate Point Along the Rod . . . .	106
A.5	Wave Reflection and Refraction at Discontinuity . . . . .	115
B.1	Entran's EGCS-240D Accelerometer Cutaway. . . . .	120
B.2	Accelerometer model . . . . .	120
B.3	Plot of the Magnification Factor $R$ for Various Values of the Damping Ratio $\xi$ . . . . .	125

## CHAPTER I

### INTRODUCTION

#### 1.1 Introduction

Penetrometers are widely used throughout the world by civil engineers for in-situ measurements of soil properties. A wide variety of penetrometers have been developed over the years, and the interpretation of results is therefore dependent on the type of penetrometer used and the testing procedure. In the classification of penetrometers, a distinction between static and dynamic penetrometers is made. A static penetrometer uses a static force to penetrate an object into the soil, while dynamic penetrometers utilize an impact force for the penetration. The Standard Penetration Test (SPT) is one form of dynamic penetration test. The practice of driving a one-inch diameter open-end into the bottom of a bore hole to recover drive samples of soil was introduced in 1902 and make the beginning of dynamic penetration testing and sampling of soils. Between the late 1920's and the early 1930's, the attempt was made to standardize the test. The term "standardization" is a misnomer since many versions of the actual SPT system (hammer, rod and sampler) are being used throughout the country.

Since the SPT blow count is inversely proportional to the energy delivered to the rod (Schmertmann and Palacios 1979), different methods and procedures have been suggested and used to calculate this energy so that the blow count could be adjusted to a standard energy. From wave mechanics theory, an accurate measurement of the energy transferred to the rod

can be obtained by integrating the product of the force and velocity measured at the top of the rod as a function of time during a hammer blow. In addition to the energy a force-displacement relationship is also available.

Research in the pile driving area on pile capacity and pile-soil interaction has successfully utilized dynamic measurements of force and acceleration at the top of a pile during driving. This has been a major contribution to the advancement of the state-of-the-art in the pile dynamics area (Goble et al. 1975). From the records of force and acceleration, a prediction of the soil resistance forces along the pile was developed. Also, a calculation of the reaction and velocity at the pile toe was made from these records.

Because of the obvious similarity between the Standard Penetration Test procedure and the mechanics of pile driving, attempts have been made to measure the dynamic event of a blow in the SPT, utilizing knowledge from the pile driving area. In this project, a measurement system similar to that used for piles was transferred to the hammer-rod system used in the SPT. This system was then tested in the laboratory. When good measurements were obtained the system was tested in the field during actual SPT operations.

## **1.2 Scope and Objective**

The origin of the Standard Penetration Test, its applications to soil formations, the interpretation of data, and the limitations of the test are discussed in Chapter II along with a description of different procedures to measure the energy. A description of the calculation of force and displacement at the toe of the rod from the records of force and velocity at the top, is also given in this chapter. In Chapter III there is a theoretical discussion of wave propagation in SPT systems and a derivation of a means of calculating the wave form generated in the rod by a hammer blow is presented. Measuring systems, data acquisition

systems and processing procedures used for the tests in this project are described in Chapter IV. Evaluation of the results from laboratory and field tests are given in Chapter V, and the conclusions are summarized in the following chapter.

This thesis describes the attempt to measure force and acceleration at a point in the rod during an SPT blow. No attempt has been made to study the sampler-soil interaction or to correlate SPT blow count to the engineering properties of soils. With an accurate measurement system of this kind, a better understanding and prediction of the above mentioned characteristics can be developed.

## **CHAPTER II**

### **REVIEW OF PREVIOUS WORK**

#### **2.1 Standard Penetration Test**

The Standard Penetration Test (SPT), defined by the American Society for Testing and Materials (ASTM) D-1586-67, is widely used in the United States for the investigation of subsurface soil properties. The test has developed from being an individually designed and locally used test into a nationally standardized and widely used test for soil exploration.

The test consists of dropping a 140 lb hammer for a free fall of 30 inches to impact the top of a rod to which a split-spoon sampler is connected at the lower end (Fig. 2.1). The number of blows required to drive the sampler 12 inches into the ground is known as the standard penetration number, the N-value, or the blow count. The usual procedure is to drive the rod into the bottom of a borehole and to record the number of blows each 6 inch interval for the first 18 inches of driving. The blow count is taken as the sum of the last two 6 inch increments. The reason for this is that the drilling operation is assumed to have disturbed the soil directly below the bottom of the boring, giving an erroneous blow count for about the first 6 inches.

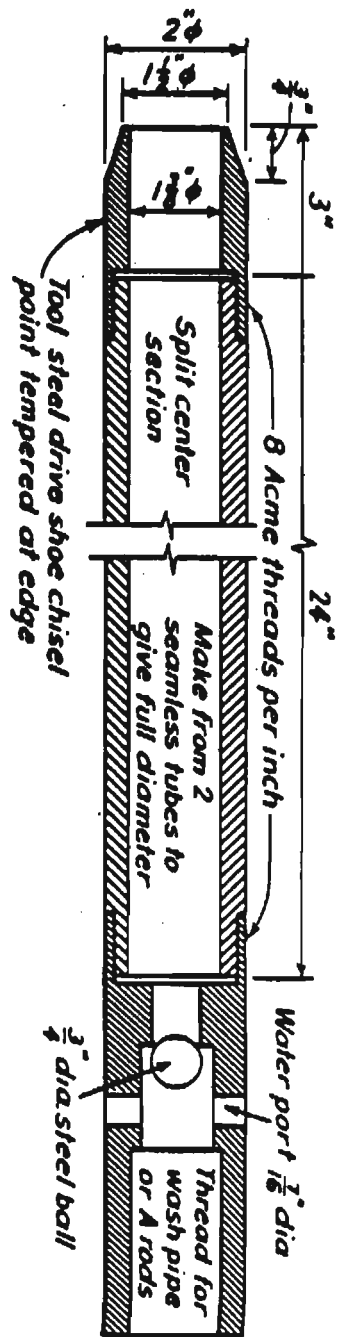


Figure 2.1: A typical Split-Spoon Sampler by ASTM D1586-67.

## 2.2 History of the SPT

The Standard Penetration Test came into being as a result of the development of dry sample recovery techniques. Previously, subsurface investigations were performed primarily through the use of wash borings. A wash boring involves the circulation of a water and/or drilling mud mixture to remove the cuttings from the boring as the hole is advanced. In 1902, Charles R. Gow introduced the first method of dry sample recovery (Fletcher 1965). He used a 110 lb weight to drive a one inch outside diameter sampling pipe. After this method was used for a short time, it became apparent that the resistance to driving the sampler was influenced by the condition and properties (e.g., strength and density) of the soil. Thus, the term, "penetration resistance", was used to define the number of blows required to drive the sampler a given distance.

In 1922, the Charles R. Gow Company merged with the Raymond Concrete Pile Company where L. Hart and G.A. Fletcher devised a split-spoon sampler (1927) of 2 inches diameter which is very similar to the current Standard Penetration Test (ASTM D-1586). In the late 1920's through the efforts of Gordon Fletcher, Linton Hart and Harry Mohr, the first steps towards standardization were undertaken. The drive weight was changed from 110 lb to 140 lb and the drop height was set at 30 inches. After extensive field and laboratory work, the number of blows required to drive the sampler into the soil a distance of 12 inches was established as an official record of the test. After the initial work in the later 1920's the test remained essentially unchanged until 1954 when James Parsons introduced a new method of recording the blow count. Instead of a penetration of 12 inches the sampler was driven 18 inches into the soil and the blow count was noted for each increment of 6 inches. The two smallest 6 inch incremental blow counts were then added and recorded as the blow count.

Since 1954, the only feature of the test to change significantly has been the method

of recording the blow count. The sampler is still driven 18 inches into the soil. The blow count for the first 6 inches of penetration is recorded but is considered a seating drive. The blows required to drive the sampler the final 12 inches are recorded as the blow count (N value) although the number of blows required for each six inch increment is normally recorded.

### **2.3 Uses of the SPT**

The original purpose of the SPT was to obtain an approximate correlation between the blow count and expected behavior of the soil under load. However, as the popularity of the test increased, so did the uses in which it was employed.

Researchers and engineers have made a great deal of effort to correlate the results of the SPT to the determinations of material properties and the development of design aids. The SPT is performed in granular and cohesive soil to obtain an indication of the in-situ soil properties. Terzaghi and Peck (1948) proposed a correlation between the N value, the relative density and bearing capacity of sand (Table 2.1); also a correlation between the N-value, the consistency and the unconfined compressive strength of cohesive soil (Table 2.2). Research on this subject was performed by Gibbs and Holtz (1957) and later by Marcuson and Bieganousky (1977) to estimate the in-situ relative density from the N-value. They also performed correlation studies between blow count, relative density of sand and the effective overburden pressure. See Figure 2.2.

The blow count has also been shown to have a correlation with the shear strength parameters of soil (Fig. 2.3). De Mello (1971) and others found by statistical analysis of data that curves such as the ones in Figure 2.3 agree reasonably well with reality, provided the SPT blow count is not from very shallow depths.

Table 2.1: Relative Density of Sand

Blow Count N	Relative density	Allowable Bearing Capacity $q_u$ (tons/ft <sup>2</sup> )
Less than 10	Loose	Requires Compaction
10 - 30	Medium	0.7 - 2.5
30 - 50	Dense	2.5 - 4.5
Over 50	Very Dense	over 4.5

Table 2.2: Consistency of Cohesive Soil

Blows N	Consistency	Unconfined Compressive Strength (tons/ft <sup>2</sup> )
0 - 1	very soft	< 0.25
2 - 4	soft	0.25 - 0.5
5 - 8	medium	0.5 - 1.00
9 - 15	stiff	1.00 - 2.00
16 - 30	very stiff	2.00 - 4.00
Over 30	hard	over 4.00

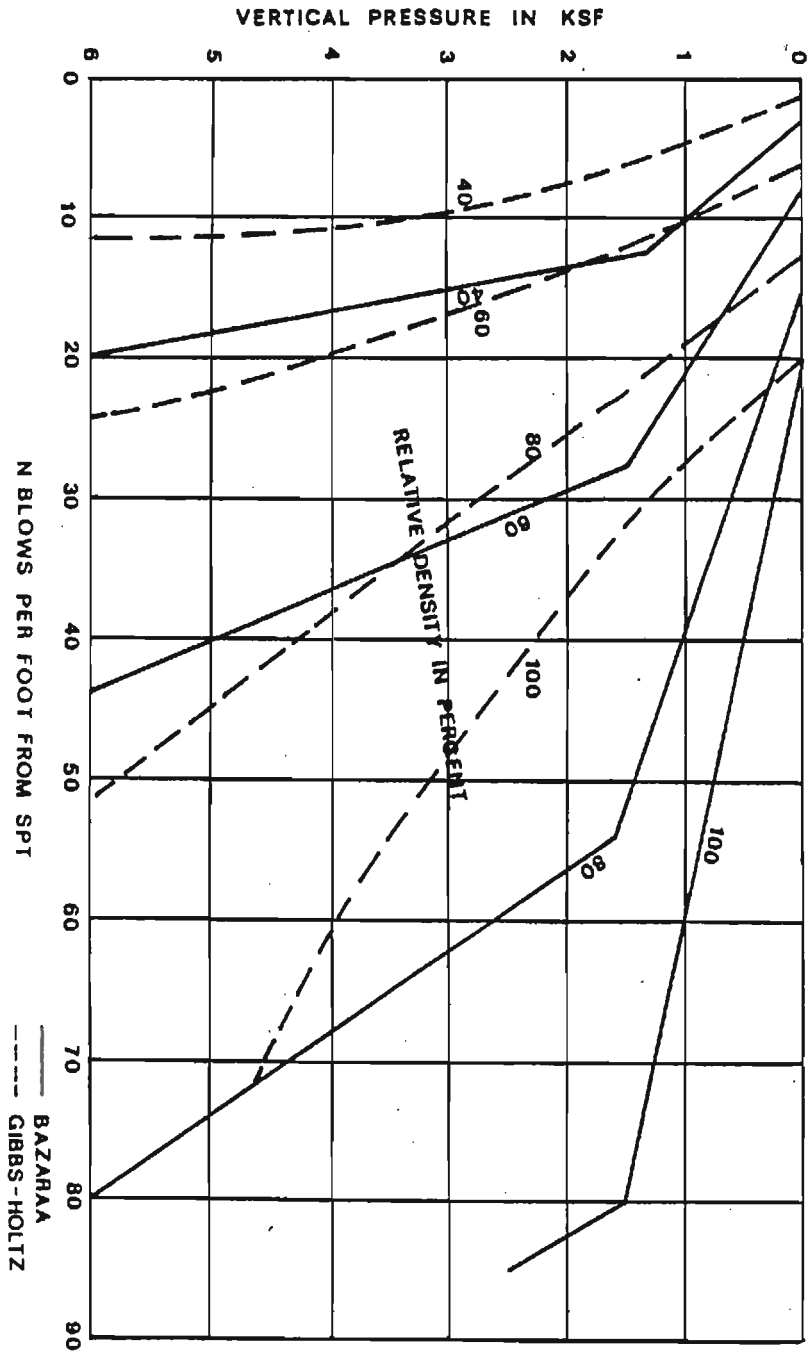


Figure 2.2: Correlation Between SPT Blow Count and Relative Density of Cohesionless Soils as Given by Gibbs, Holtz and Bazarrá.

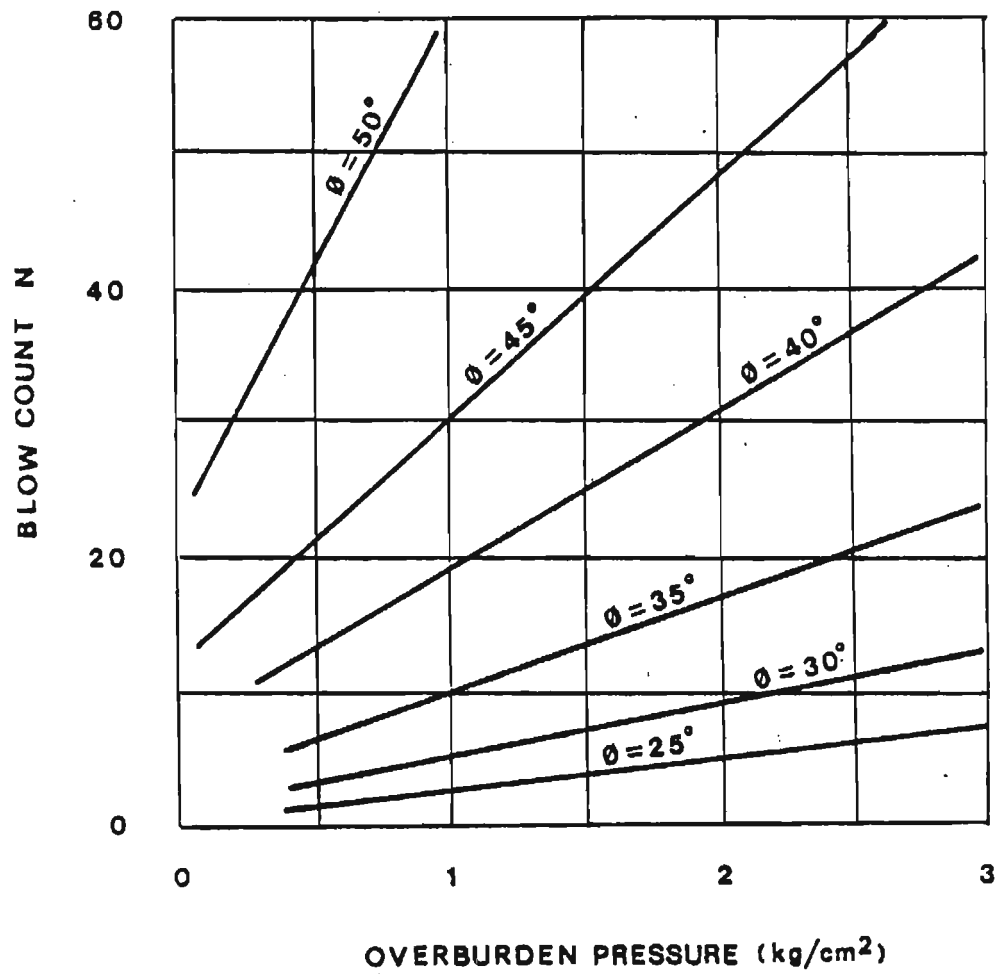


Figure 2.3: Estimation of  $\phi$  (Angle of Internal Friction) from the SPT Blow Count. (After Schmertmann)

The test is also very useful in the design of pile foundations. It is used to simulate the pile during driving in an attempt to discover any problems that may occur when the actual driving takes place. Most pile foundations in granular soils are initially analyzed on the basis of SPT N-value. Meyerhof (1976) suggested that the ultimate point resistance in a homogeneous granular soil can be obtained from standard penetration resistance (Fig. 2.4); also he indicated that the average unit frictional resistance for driven high-displacement piles can be obtained from average standard penetration resistance values  $\bar{N}$  (Fig. 2.5). In which  $\bar{N} = N$  when  $N \leq 15$  and  $\bar{N} = 15 + 1/2(N-15)$  when  $N > 15$ . The test is very useful in determining in-situ soil coefficients commonly used in computer programs that use the one-dimensional wave equation to model a pile during driving.

The Standard Penetration Test is also used for evaluating the liquefaction characteristics of a sand deposit. It was found that the most significant property of a soil affecting its liquefiability was the relative density, and as previously mentioned the SPT can give an indication of this. Schmertmann (1977) indicated such a relation, and Seed et al. (1977) found the correlation shown in Figure 2.6 where N-value was corrected to an overburden pressure of 1 ton/sq.ft, because of the effects of increasing overburden pressure on penetration resistance.

In addition to the information obtained during the performance of the test the sample can yield some very useful data. Since the sample is highly disturbed, only identification tests are usually performed. From the sample the engineer can determine color, macrostructure, strata delineation, water content, Atterberg limits, specific gravity and texture.

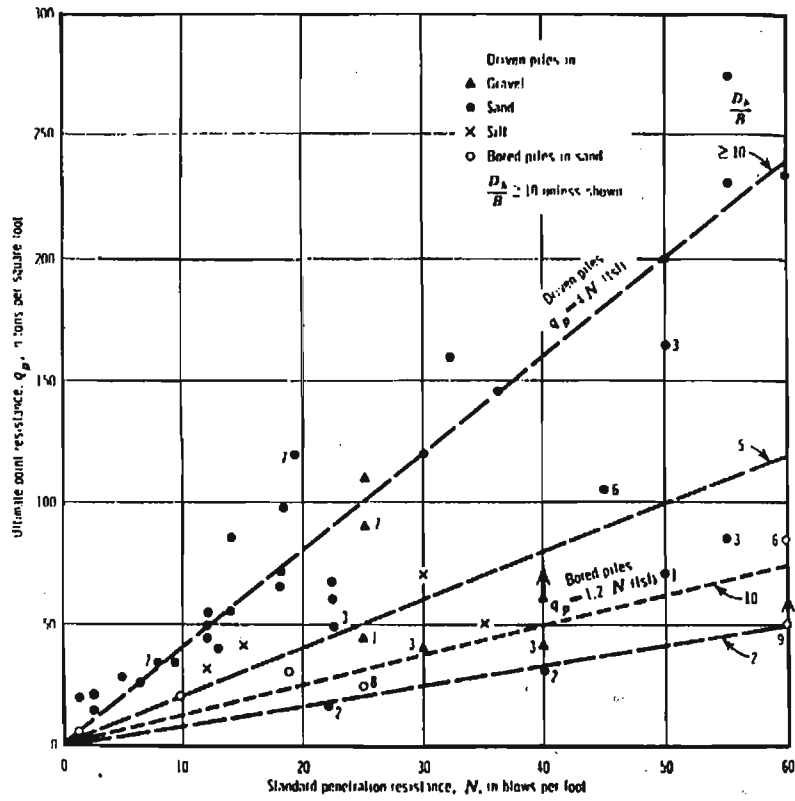


Figure 2.4: Empirical Relation between Ultimate Point of Piles and Standard Penetration Resistance in Cohesionless Soil (1 tsf = 95.8 kn/m<sup>2</sup>)

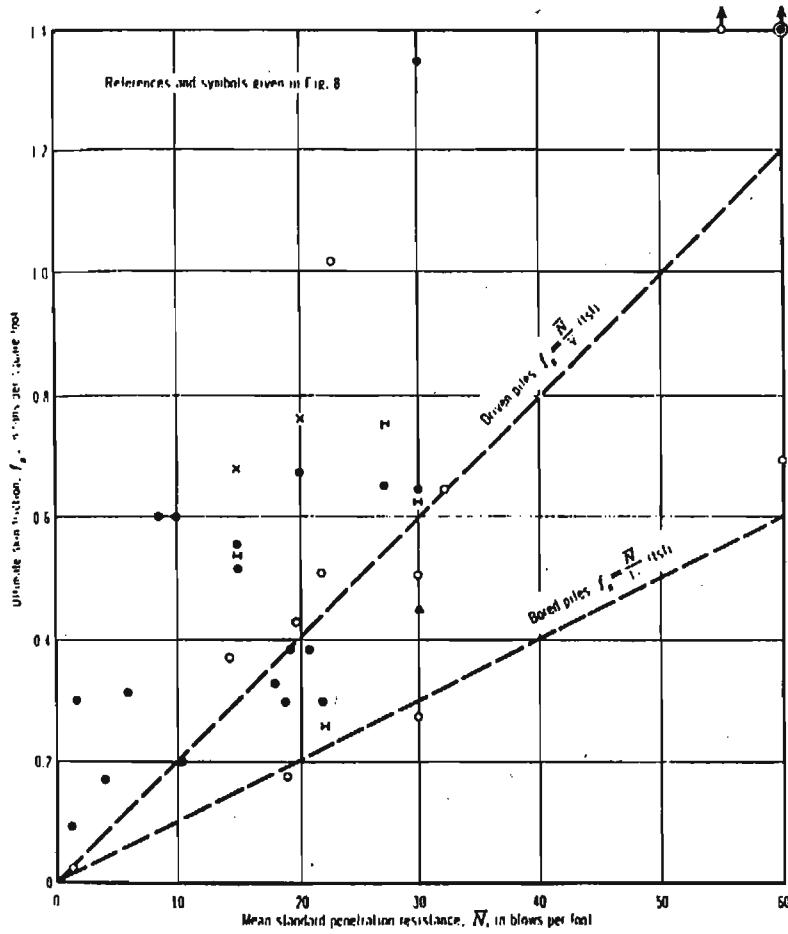
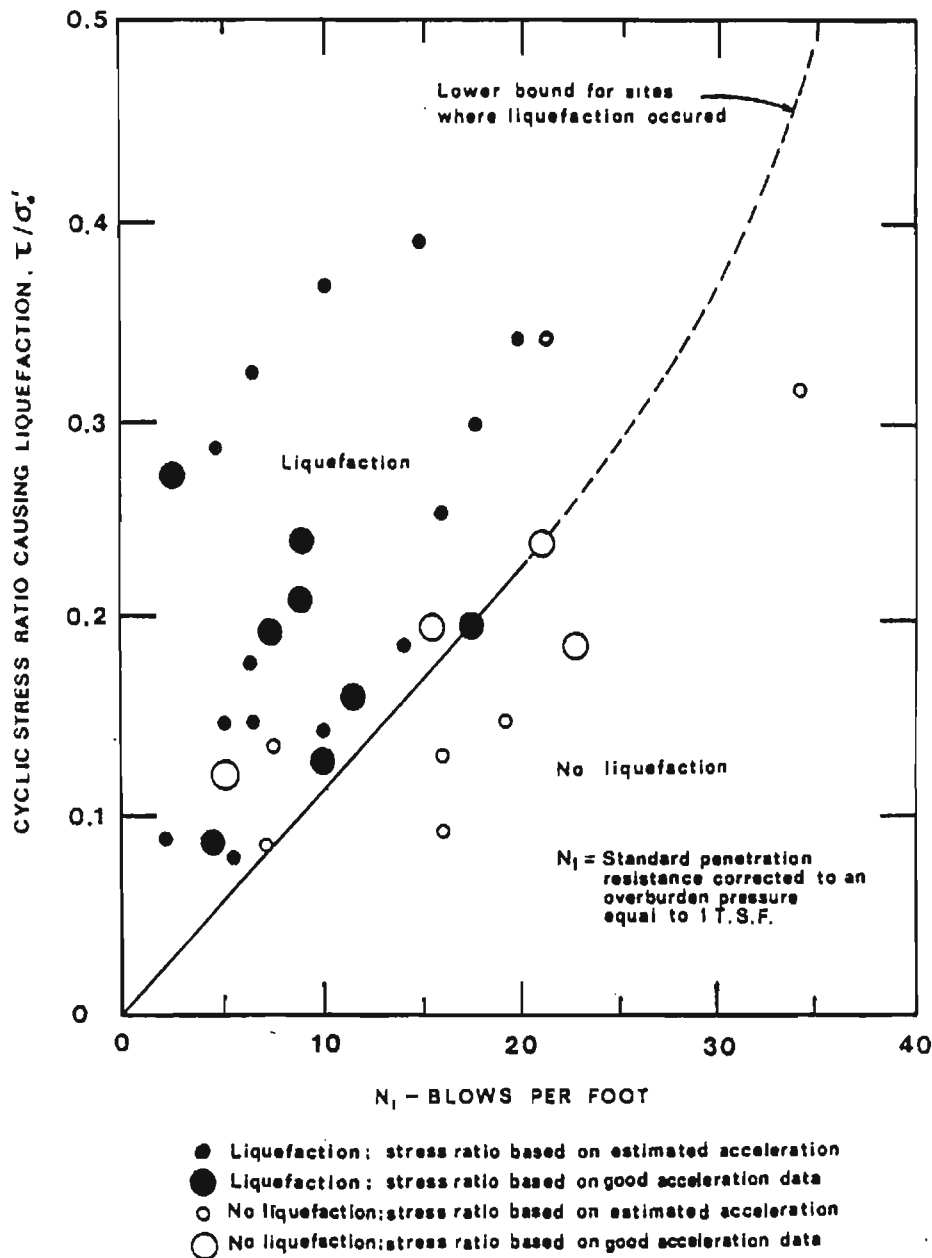


Figure 2.5: Empirical Relation between Ultimate Skin Friction of Piles and Standard Penetration Resistance in Cohesionless Soil (1 tsf = 95.8 kn/m<sup>2</sup>)



$\tau_{av}$  is the average horizontal shear stress induced by earthquake shaking.

$\sigma'_v$  the initial effective overburden pressure.

$N_1$  is the corrected N-value.

Figure 2.6: Correlation Between Stress Ratio Causing Liquefaction in Field and Penetration Resistance of Sand.

## **2.4 Reliability of Blow Count of the SPT**

The reliability of the blow count depends on the ability to maintain consistent delivered energy in driving systems. Different delivered energies may result in significantly different blow counts in the same deposit at the same overburden pressure because the SPT blow count has been shown to be inversely proportional to the delivered energy (Schmertmann and Palacios 1979). An understanding of the factors which affect the penetration resistance values and procedures which cause the wide variation in delivered energy of drill rigs is therefore necessary.

Factors affecting the reproducibility of the Standard Penetration Test include: personnel, equipment and procedure. A. Casagrande and L. Casagrande (1968) noticed considerable differences in penetration resistance N values obtained by two different drilling contractors in sands at the same depth on the same site in Michigan adjacent to Lake Michigan. Also from a research study at the University of Colorado (Goble and Ruchti 1981) on the performance of safety hammers operated by cathead and rope, it was found that the height of the drop as well as the delivered energy varied between different operators and also for the same operator. In a comparison study between the cathead and rope system and the Mobile Drilling Company's automatic winch and cable operated driving system, Kovacs et al. (1975) performed additional testing to evaluate several parameters that effect the impact velocity. These parameters included fall height, hammer type, inclination of the drill stem, number of wraps on the cathead, cathead speed, rope age, method of release of the rope, sampler type and hammer stroke. Kovacs also presented a useful summary of available research on the SPT.

The effect of in-situ stresses will change the blow count accordingly, but this is the in-situ state of the soil at a particular site and the blow count itself is correct. Other factors

affecting the blow count and leading to erroneous results are the actual mechanical performance of the SPT procedure. These factors are inherent in the present procedure and are sometimes difficult to avoid. They were pointed out by several authors and are:

1. Inadequate cleaning of borehole.
2. Upward seepage of water into borehole.
3. The height of drop of hammer.
4. The friction between hammer and rods during drop.
5. Weight (type) and length of drill rods.
6. Monitoring number of blows.

The most significant of these is probably (3) because this determines the impact velocity of the hammer. From the study at the University of Colorado where the velocity of the hammer at impact was measured, and the height of drop showed great influence on the velocity. Kovacs, et al. (1978) also found similar results and proposed a new testing procedure.

## **2.5 Energy Measurements**

In any field or laboratory testing procedure, the ability to reproduce results is important. In the case of the SPT, the main source of the unreliability of the blow count is the difficulty in producing identical drops to maintain the same impact velocity as well as delivered energy. From a study done by Schmertmann and Palacios (1979), it was found that the blow count is inversely proportional to the energy absorbed by the soil during a test. In order to determine experimental results of this kind, a way of measuring the energy in the rods was developed.

It appears that the work of Schmertmann et al. (1978) was the first that sought to more directly evaluate the variations in ram impact velocity. He made strain measurements in the drill rod and calculated delivered energy. In his procedure he assumed that the kinetic energy of the driving system is fully transmitted to the drill rod before the reflected stress wave arrives back at the top. Thus, the transferred energy is

$$E(t') = \frac{c}{EA} \int_0^{t'} F(t)^2 dt \quad (2.1)$$

where  $c$  is the speed of the stress wave propagation,  $E$  is the modulus of elasticity of the drill rod,  $A$  its cross-sectional area,  $F$  is the force measured near the top of the drill rod given as a function of time and  $t'$  is the time when the first force record passes through zero. The analytical basis of Equation 2.1 is presented in Chapter III.

The primary weakness of Schmertmann's approach is that for short drill strings the reflected wave will arrive at the top before all of the transmitted wave has been input. If there is a loose connection in the drill string, an early zero is also possible.

Kovacs et al. (1978) attempted to measure the velocity of the hammer at the instant of impact. This will give a measure of the energy available just before impact occurs. Measurements of this type, however, do not include energy losses at impact, and more important, do not give a time history record of the event. Therefore, a method from the pile dynamics area was used. It is known from pile dynamics that the energy delivered to the rod can be expressed as a function of time

$$E_i(t) = \int_0^t F(t)v(t)dt \quad (2.2)$$

where  $v$  is velocity measured as a function of time. These quantities can be measured using strain gages for the force while the velocity can be obtained by integration of the output of accelerometers. From this setup a force-displacement relationship of the event also would be available. This method, however, has been unsuccessful since problems involving the acceleration measurement occurred. This was said to be due to high vibration frequencies resulting from metal to metal impact (Hauge 1979).

In an attempt to measure the energy absorbed by the soil during an SPT test, Schmertmann and Palacios (1979) used two force transducers, one at the top and one at the bottom of the drill string. In this way the incident and reflected energy could be obtained from force measurements at the top and the bottom, respectively. The difference between the two would then be the energy absorbed by the soil. With this method, a successful way of measuring the energy was obtained. Figure 2.7 shows a schematic sequence of the hammer-impact wave pulse moving up and down the rods and through the two load cells mentioned previously.

## 2.6 Computation of Bottom Velocity, Displacement and Reaction Force

From a research program at Case Western Reserve University by Goble, et al. (1975) and Teferra (1977), a procedure of finding resistance forces acting at the pile tip during driving has been developed. This method makes use of measured force and acceleration at the pile top as input quantities. The computational procedure is based on the superposition of different boundary conditions. A free pile is defined to have the prescribed measured

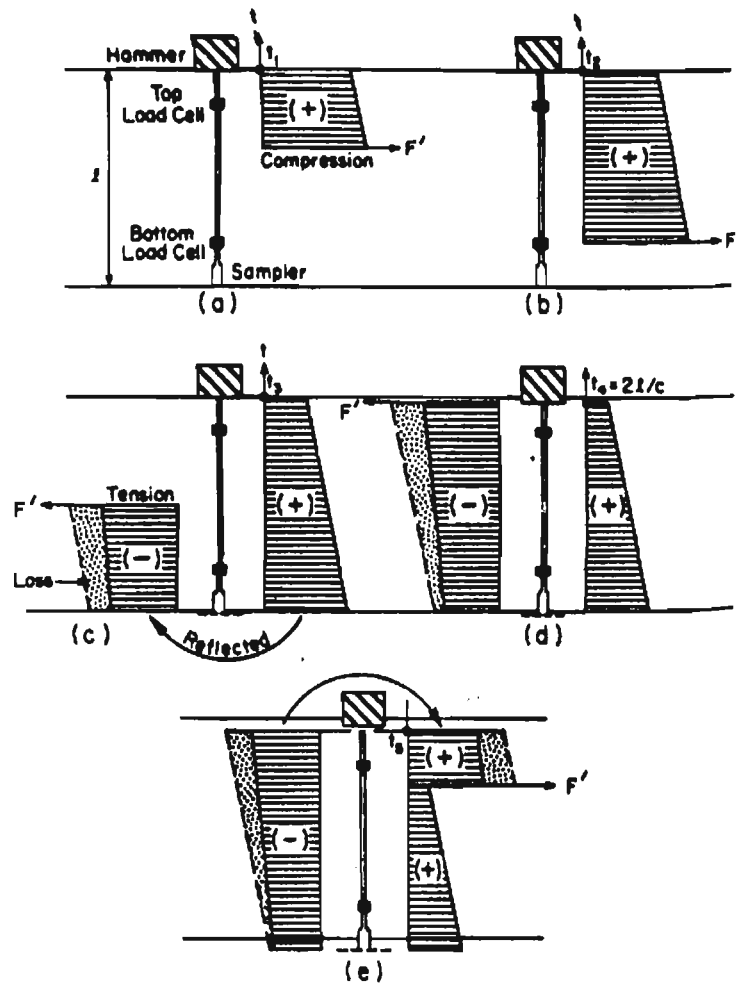


Figure 2.7: Schematic of First Comprehensive Wave at Sampler and Then at Hammer. (After Schmertmann and Palacios)

velocity (or acceleration) at the top and zero forces acting along its length and toe end. The actual pile is defined as a pile which has the measured velocity at the top and the real resistance forces acting along its length and toe end. Thus, the difference between the measured top force of the actual pipe and that of the free pile will be the top force for a pile whose top is fixed, and to which the actual resistance forces are applied. This difference has been referred to as the Measured Delta Curve. Here, the effect of the actual resistance forces on the force at the pile top has been separated from the forces due to the applied velocity. In this analysis the skin resistance forces are assumed to be zero, which actually corresponds better to the SPT than to pile driving because the hole is augered down to the desired depth in the SPT procedure. Therefore, all side friction should be eliminated.

In order to obtain the Measured Delta Curve an expression must be obtained for the free pile solution. This can be obtained from Equation (A.14) in Appendix A.

$$F_f(t) = \frac{EA}{c} [v_r(t) - 2v_r(t - \frac{2L}{c}) + 2v_r(t - \frac{4L}{c}) \dots + \dots] \quad (2.3)$$

Here  $F_f(t)$  is the free pile solution,  $v_r(t)$  is the measured top velocity,  $L/c$  is the time required for the wave to travel the length of the pile, and  $A$  is the cross-sectional area of the pile. Thus, with the aid of Equation 2.3, a curve of the free pile solution is available. The difference between this curve and the measured top force is the Measured Delta Curve which represents the effect of the tip reaction forces on the pile top force. In the case where no skin friction forces are available, as in the SPT procedure, the reaction at the toe can be computed from the Measured Delta Curve using Equation A.16 in Appendix A, by letting  $x$  equal  $L$  (i.e., the load acts at the toe of the pile). The following expression is obtained:

$$F(t) = 2R(t - \frac{L}{c}) - 2R(t - \frac{2L}{c}) + 2R(t - \frac{5L}{c}) - 2R(t - \frac{7L}{c}) + \dots \quad (2.4)$$

where  $F(t)$  is the top force effect (Measured Delta Curve) and  $R(t-L/c)$  is the toe reaction.

By rearranging this equation the expression for the toe reaction is obtained.

$$R(t - \frac{L}{c}) = \frac{1}{2}F(t) + R(t - \frac{3L}{c}) - R(t - \frac{5L}{c}) + R(t - \frac{7L}{c}) - \dots \quad (2.5)$$

The bottom velocity is computed by superimposing the measured top velocity produced by the impacting hammer and the velocity effect produced by the toe reaction forces, assuming fixed top and a free toe pile model.

$$\begin{aligned} v_b(t) = & 2v_i(t - \frac{L}{c}) - \frac{c}{EA}R(T) - 2v_i(t - \frac{3L}{c}) + \frac{c}{EA}2R(t - \frac{2L}{c}) \\ & + 2v_i(t - \frac{5L}{c}) - \frac{c}{EA}2R(t - \frac{4L}{c}) \end{aligned} \quad (2.6)$$

Now, with an expression for the toe velocity as a function of time, the toe displacement can be computed by the integration of the toe velocity.

$$d_{toe}(t') = \int_0^{t'} v_b(t) dt \quad (2.7)$$

where  $d_{toe}$  is the toe displacement and the time  $t$  is measured at the bottom of the pile.

With records of the toe displacement, Equation 2.7, and toe reaction force, Equation 2.5, a means of determining the force-displacement relationship, which yields the spring constant of the soil, can be obtained. The method described above was applied to the pile driving procedure, but since, as mentioned before, the main assumption for this derivation is the assumed zero resistance force along the pile (i.e., only toe resistance), the method seems to have the ability to apply well to the SPT procedure. A basis for such an analysis, however, is accurate records of the measured force and velocity at the top of the rod.

## CHAPTER III

### WAVE PROPAGATION IN THE SPT

#### 3.1 One Dimensional Wave Mechanics

When a rod is struck at the end by a mass a small zone of material is first compressed. This compression causes a strain,  $\epsilon$ , and, therefore, a force  $F = \epsilon AE$  ( $A$  is cross sectional area and  $E$  is Young's Modulus of the rod). The force,  $F$ , then compresses a neighboring particle. However, since material is compressed a motion of the particles is also necessary, and a particle velocity,  $v$ , is generated in the rod. Whenever a velocity is given to a particle of mass  $m$  within a time period  $\Delta t$  the particle has to be accelerated causing an inertia force  $mv/\Delta t$ . This inertia force is in balance with the strain force and because it takes time to accelerate the particles, the strain will be transferred at a certain speed,  $c$ , called the wave speed. From the assumption that the wave propagates in the longitudinal direction only, (i.e. the transverse effect in a rod, where the ratio of radius to length is small, will be insignificant) the governing equation for the wave transmission is, from (Goble 1988)

$$\frac{\partial^2 u}{\partial t^2} = c^2 \frac{\partial^2 u}{\partial x^2} \quad (3.1)$$

Derivation and solution of this equation and a discussion of the boundary conditions are given in Appendix A, adapted from (Rausche 1988), (Goble 1988) and (Fischer 1984).

The speed of wave propagation is only dependent on the material properties of the

rod, and not on boundary conditions or the physical behavior of the hammer impact. It is equal to  $\sqrt{E/\rho}$ , where  $\rho$  is the mass density of the material. For the AW steel rods used in this project,  $c$  was taken as 16,800 ft/sec.

### 3.1.1 Boundary Conditions

In a uniform, elastic rod, where no external forces act, the stress gradient will travel through the rod without being changed in magnitude. In Equation (3.1) an infinite rod was assumed for the derivation. An important consideration is to deal with what happens when a stress wave arrives at the end of a rod. Two cases will be dealt with, namely a wave approaching a free and a fixed end.

#### a) Free End:

When a stress wave arrives at an end, the stress gradient will be changed. At a free end, the particles will be subjected to higher accelerations since no further material is strained in front of the wave. Now, due to higher accelerations, a new stress gradient will build up between particles next to the end. A new stress wave will thus be generated traveling away from the end, and is called a reflected wave. The particles will move in the same direction, while the sign of the stresses will change. Thus, a compression stress wave arriving at a free end will be reflected back as a tension wave, having the same absolute magnitude as the compression wave, and the same form. Since the stress wave is not instantaneous, but has a finite rise and decay time, a portion of this reflected tension wave is superimposed back on the still oncoming part of the compression wave. Because the velocity in the oncoming and reflected wave has the same direction, the total velocity in the immediate region of the tip will double during the time of reflection.

**b)Fixed End:**

For the case of a wave approaching a fixed end, opposite conditions result. Acceleration of the particles at the tip is not possible, and thus the superposition of motions at the tip will result in zero velocities. The stress wave will reflect with the same sign, and the stress will build up to twice its original magnitude at the point of reflection. A compression wave will reflect as a compression wave, and therefore the direction of particle motion will be opposite in oncoming and reflecting waves.

### 3.1.2 Discontinuity in Bar Properties

A sudden change in the bar properties will impose a disturbance in the wave transmission. Depending on the nature of the change, for example, if an increase or decrease in area is encountered by the oncoming wave, part of this wave will be transmitted and part will be reflected at the point of change. Two continuity conditions are imposed at the juncture, namely, that the force and displacement at both sides of the juncture must at all times be equal. From these facts the reflected and the transmitted wave can be calculated in terms of force and particle velocity, (see Appendix A).

$$F_t = \frac{2\alpha}{1 + \alpha} F_i \quad v_t = \frac{2}{1 + \alpha} v_i \quad (3.2)$$

$$F_r = -\frac{1 - \alpha}{1 + \alpha} F_i \quad v_r = -\frac{1 - \alpha}{1 + \alpha} v_i \quad (3.3)$$

Where,

$v_t$  and  $F_t$  are the velocity and the force in the transmitted wave,

$v_r$  and  $F_r$  are the velocity and the force in the reflected wave,

$v_i$  and  $F_i$  are the velocity and force in the incident wave,

$\alpha$  is the ratio of the rod mechanical properties and is equal to  $Z_2/Z_1$ ;  $Z_i = E_i A_i / c_i$ , where indices 1 and 2 are for oncoming and transmitted section, respectively.

These relations show that the transmitted wave always has the same sign as the incident one. The sign of the force and the velocity in the reflected wave is dependent on the material ratio  $\alpha$ . For a wave approaching a decrease in area,  $\alpha < 1$ , and the sign of the reflected stress will be opposite to that of the incident, while the velocity will be in the same direction. When a wave approaches an increase in area,  $\alpha > 1$ , the opposite condition results. For  $\alpha = 1$ , that is, there is no change in the relative material constants, there is of course no reflection and the transmitted wave equals the incident. It is here also interesting to note that in the extreme cases when  $\alpha = 0$  or infinity, we have reflection at free and fixed end respectively.

### 3.2 Proportionality of Force and Velocity

At impact between hammer and rod a stress gradient is introduced at the end of the rod, producing a stress wave that travels down the rod. In a uniform rod this stress gradient will cause the same particle velocities independent of the location on the rod. One must here distinguish between particle velocity and stress wave velocity. By particle velocity reference is made to the motion of a particle point in the rod during the passage of the stress wave. This stress wave has a velocity of propagation referred to as  $c$ . From wave mechanics one can develop a relationship between the stress at a point on the rod and the particle velocity. In Figure 3.1 the wave has already traveled to a point which is still at rest. During a time interval  $\Delta t$  the wave travels additional distance  $\Delta L = c \Delta t$  and since the material below became compressed, the point moved a distance  $\delta$ . This deformation  $\delta$  was caused by a strain  $\epsilon$  over a distance  $\Delta L$  and therefore

$$\epsilon = \frac{\delta}{\Delta L}$$

But replacing  $\Delta L$  by  $c\Delta t$  leads to

$$\epsilon = \frac{\delta}{c\Delta t}$$

Since the point traveled a distance  $\delta$  during a time  $\Delta t$  it had a velocity

$$v = \frac{\delta}{\Delta t} \quad \text{or} \quad \delta = v\Delta t$$

Substituting for  $\delta$  in  $\epsilon$  we find

$$\epsilon = \frac{v}{c}$$

Thus, the strain at a point in the rod material is proportional to the particle velocity of the same point. The relation can be expanded to cover stress

$$\sigma = v \frac{E}{c}$$

and force

$$F = v \frac{EA}{c} \tag{3.4}$$

The proportionality constant  $EA/c$  is commonly referred to as the rod impedance because it is that force with which a rod opposes a sudden change of velocity by one unit.

Equation (3.4) is valid for an infinitely long uniform rod or, applied to our case with finite rod length. It is valid when a single wave passage is considered. This means it is only valid within the first  $2L/c$  time, or the time required for the stress wave to travel down the rod, reflect at the bottom and then return to the point under consideration.

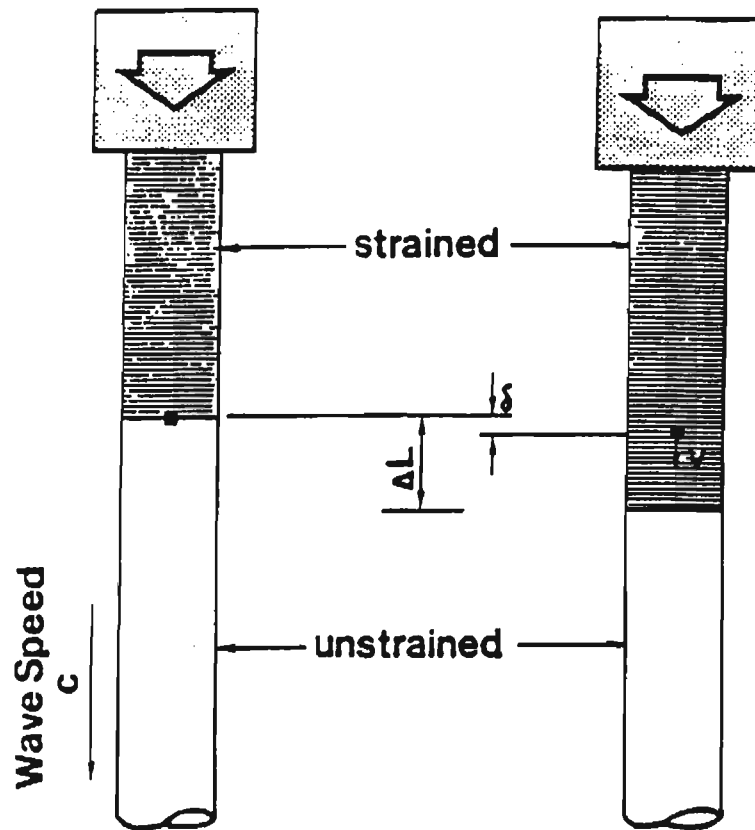


Figure 3.1: Proportionality of Force and Velocity.

### 3.3 Generation of Waves in the SPT Procedure

When the hammer impacts on the rod, it creates a compression wave traveling down the rod, and at the same time, a stress wave is generated in the hammer. Since the force and the velocity are proportional, the shape and the magnitude of the stress waves can be determined by looking at the velocity. Fairhurst (1961) describes what ideally happens when two similar materials impact. Across the plane of contact two conditions must be fulfilled during impact:

- (i) the force in the hammer must equal the force in the rod
- (ii) the absolute spatial velocities of the striking end of the hammer and the struck end of the rod must be equal at all times that the two surfaces are in contact.

From these conditions the particle velocity in the rod and the hammer can be written in terms of the impact velocity.

$$v_h = \left( \frac{\alpha}{1 + \alpha} \right) v \quad (3.5)$$

$$v_r = \left( \frac{1}{1 + \alpha} \right) v \quad (3.6)$$

where,  $v$  is the impact velocity,  
 $v_h$  is the particle velocity in the hammer,  
 $v_r$  is the particle velocity in the rod,  
 $\alpha$  is the material ratio.

#### 3.3.1 Generation of Waves in the Rod

Consider now a hammer blow in the SPT procedure, using a safety hammer and AW rods. The hammer and the driving rod are shown with their dimensions in Figure 3.2. The

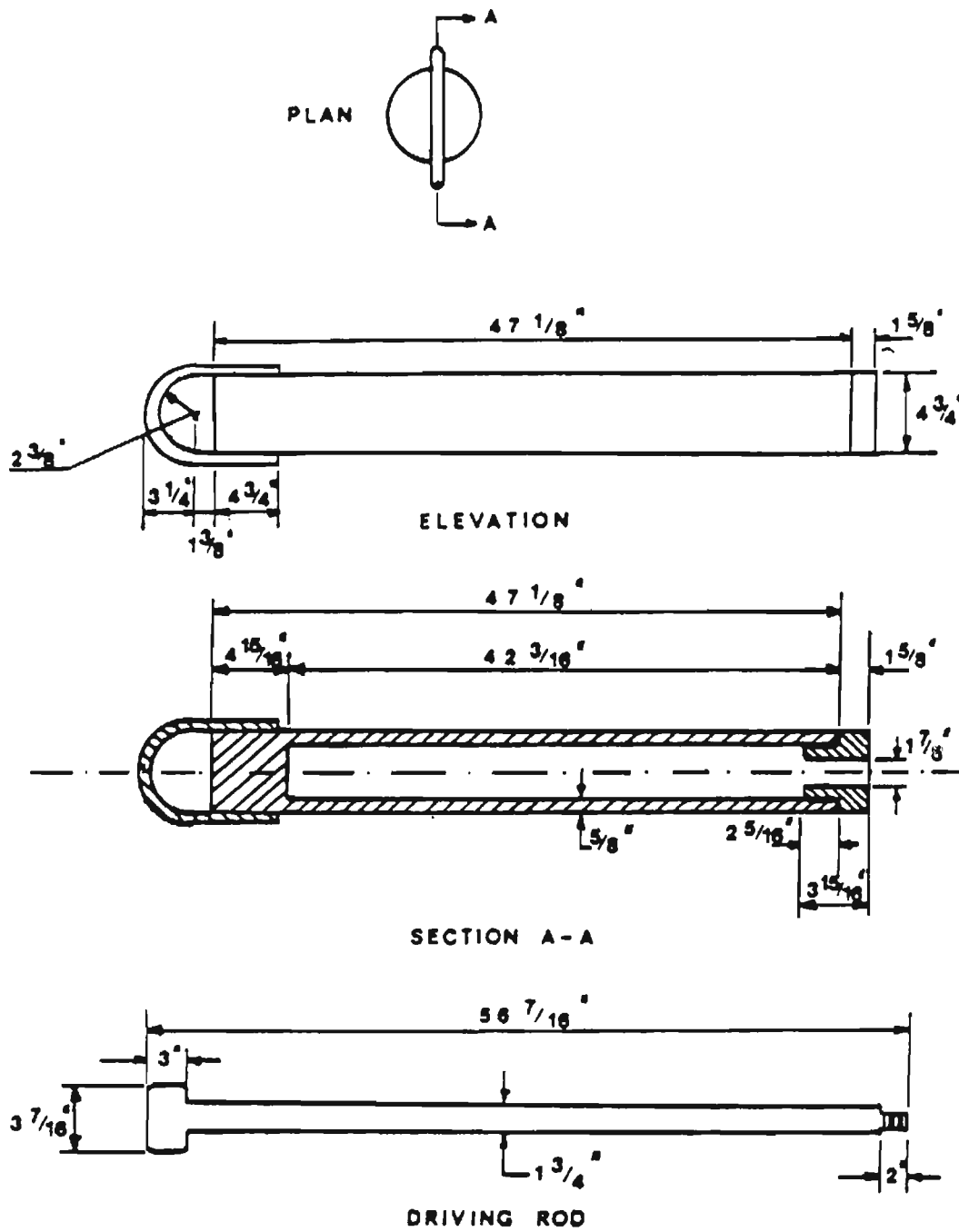


Figure 3.2: Safety Hammer and Drill Rod, with Dimensions.

AW rods come in five foot segments and are connected by threads to make up the total length required for the borehole to be tested. The schematic of a blow is shown in Figure 3.3.

In (a), the hammer is lifted up to a height of 30 inches then dropped onto the top of the driving rod, (b). Impact between hammer and rod occurs at point A. A compression stress wave is generated in the rod, propagating downward with speed  $c$  and two stress waves are generated in the hammer emerging from this point. One is going upward and is a compression wave, the other traveling downward creating tension in the hammer. The distance from the point of impact, A, to the top of hammer, B, is very short and since a free end reflection takes place at B, the stresses in section A-B will at most times be canceled due to superposition of waves. For convenience and practical purposes, one can thus ignore the part A-B and say a tension wave is generated, traveling down the hammer. The wave propagation in the system is shown in Figure 3.4. The hammer and the drive rod are of same material, which means that the material ratio  $\alpha$  equals the ratio between the areas, which in this case is 0.3. Then from Equation (3.6) the particle velocity in the drive rod  $v_r$  would be  $0.77v$  ( $v$  is the impact velocity). Just before impact, the particle velocity in the hammer is equal to the impact velocity and at impact this velocity will decrease by  $0.23v$  (Eq. 3.5) to make the particle velocity in the hammer equal to that in the rod which is  $0.77v$  (Fig. 3.4b). The same values would represent the stresses. When the downwards moving tension wave reaches the bottom of the hammer, D, a free end reflection takes place. The additional mass at the bottom of the hammer is very small compared to the hammer weight and the stress due to the inertia forces of this mass is negligible. This tension wave reflects as a compression wave of same magnitude which cancels the oncoming tension wave (Fig. 3.4c). At the juncture E between the drive rod and the AW-rods, a decrease in area is encountered by the oncoming wave. Again the two rods are of the same material, so the material ratio  $\alpha$  equals

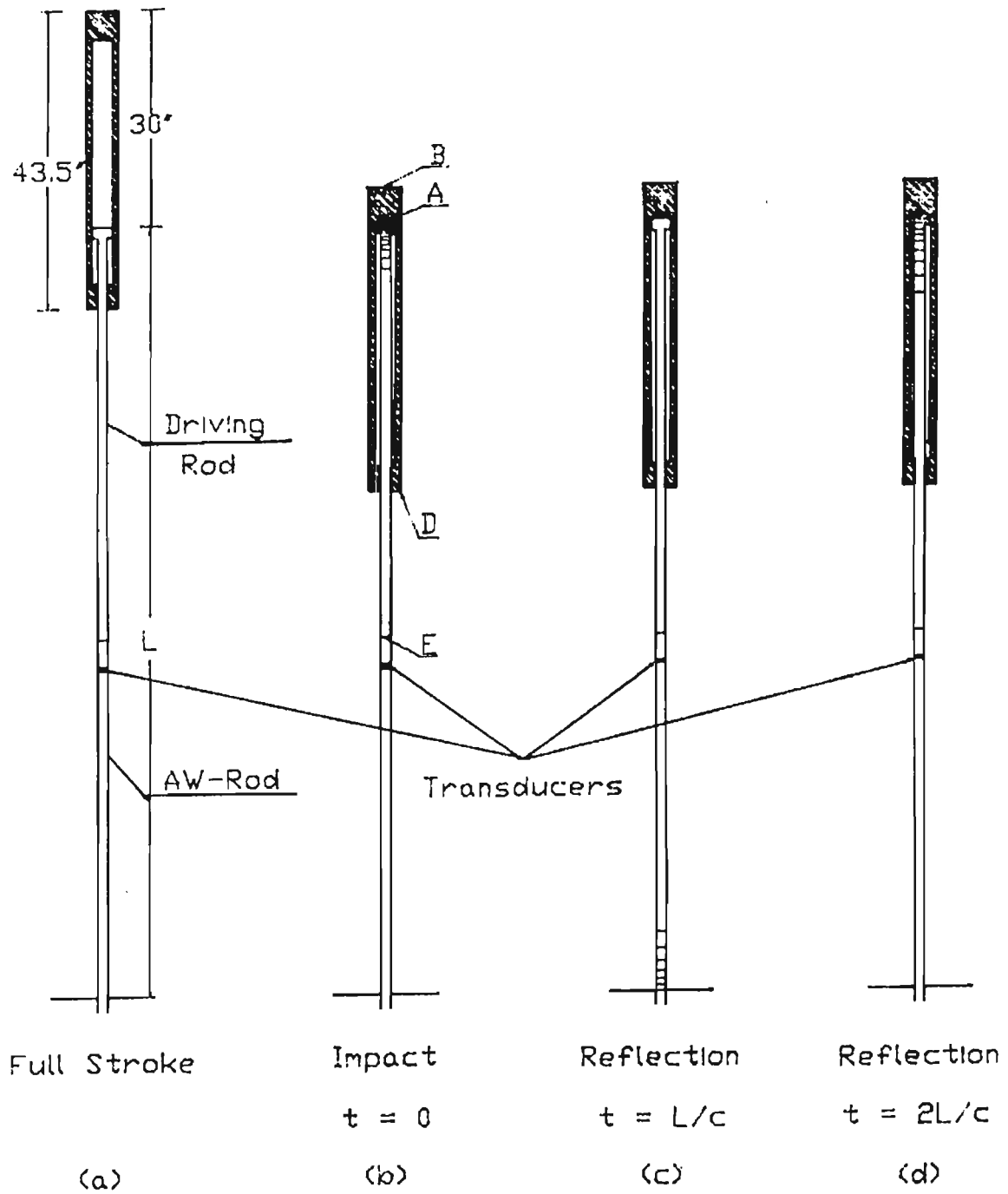


Figure 3.3: Schematic of a Blow in the SPT with Safety Hammer.

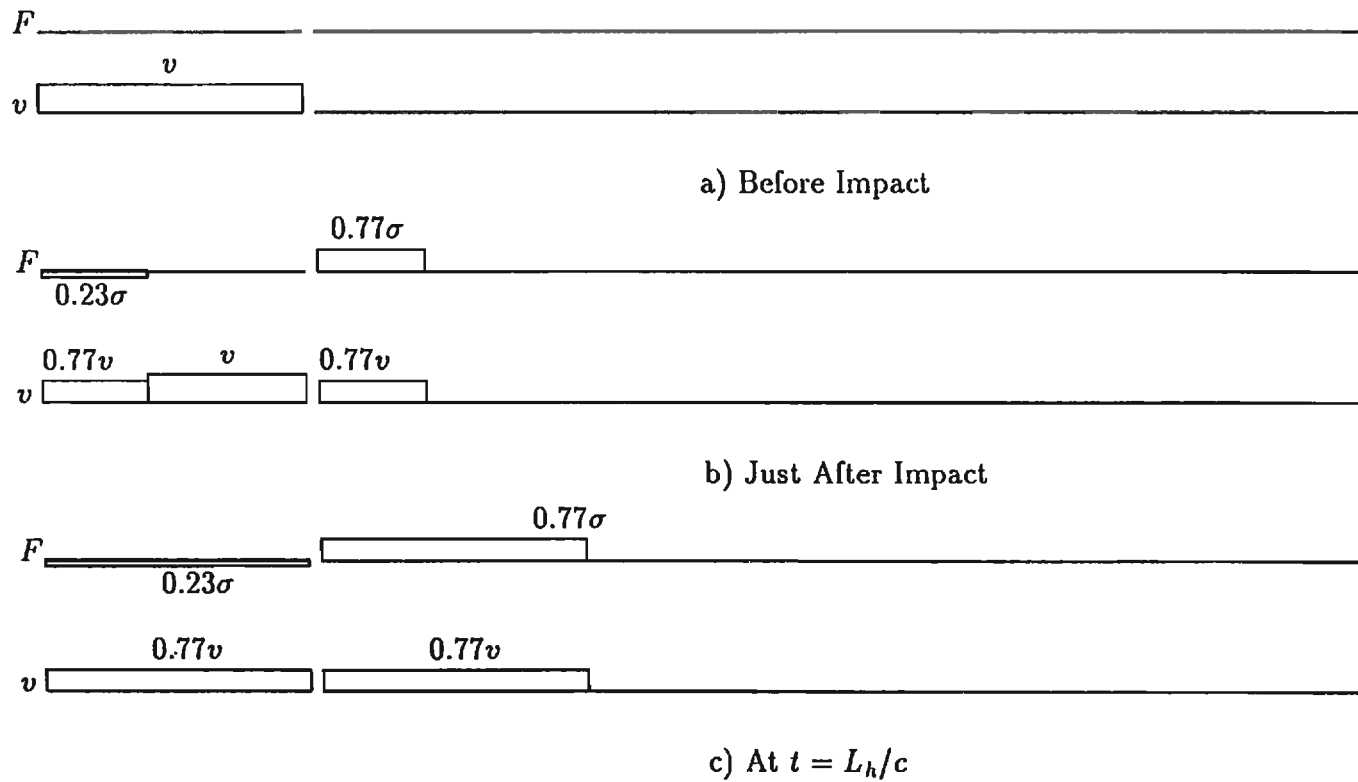
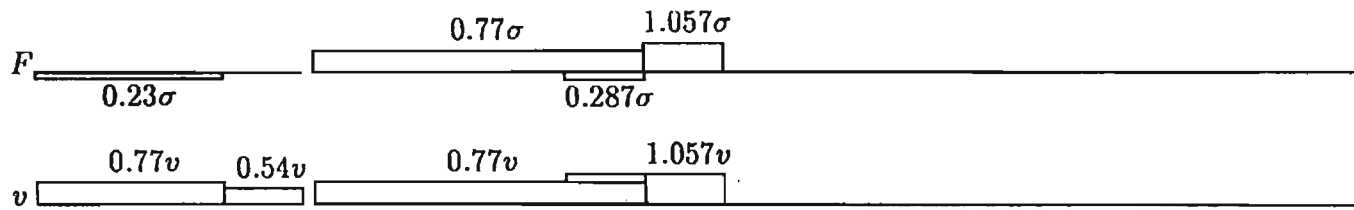
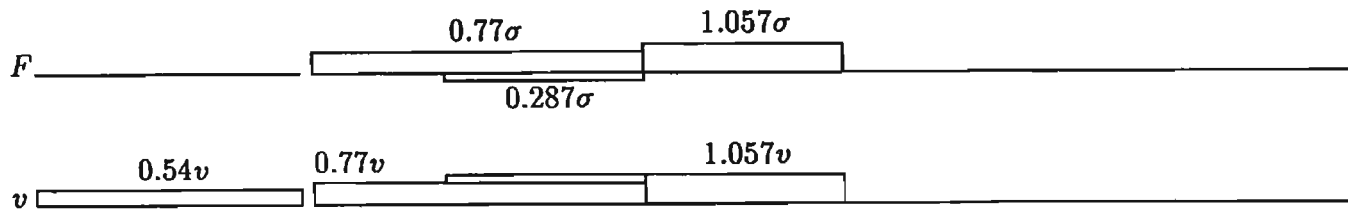


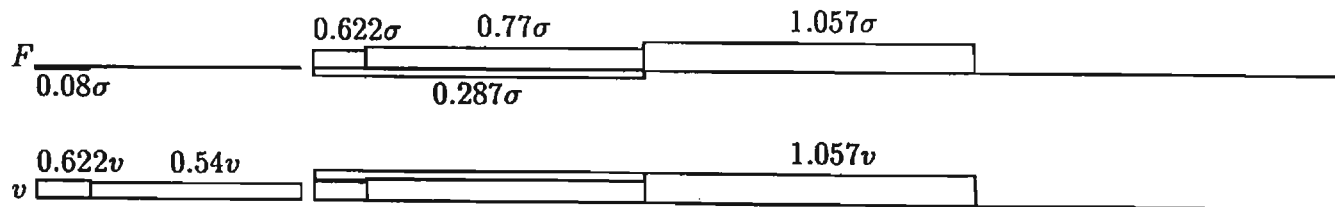
Figure 3.4: Wave Propagation in the Safety Hammer System.



d) At  $t = L_{dr}/c$



e) At  $t = 2L_h/c$



f) At  $t = 2L_{dr}/c$

Figure 3.4: Wave Propagation in the Safety Hammer (Continue).

the ratio between the areas, which is 0.457. This results in a reflection and transmission of waves according to Equations (3.2) and (3.3), which yields 63% of the compression wave force transmitted and 37% reflected back up as tension. From Equation (3.2) the transmitted particle velocity is  $1.373v_i$ , where  $v_i$ , in this case, is  $v$ , which equals to  $0.77v$  (Fig. 3.4d).

The transmitted wave propagates down the rod and encounters the transducers located six inches below juncture E. At the joint between two AW-rods, a new change in area is encountered. This change, however, is so small that the disturbance resulting from it have minimal effect on the wave transmission. When the downward moving wave reaches the bottom of the rod (Fig. 3.3c), it is reflected according to the boundary conditions, and travels back up the rod. It is again sensed by the transducers, and then it comes to juncture E where again a change in area is felt (in this case an enlargement). Therefore a reflection and transmission takes place. The transmitted wave proceeds to the top of the driving rod where it is reflected back down the rod. At this time an impact is also felt by the hammer. The cycle is then repeated.

The initially downward moving compression wave was transmitted and reflected at juncture E. The reflected wave is in tension and its value from Eq. (3.3) is  $0.373v_i$ , where  $v_i$  equals to  $0.77v$ ; then its value in terms of the impact velocity is  $0.287v$ . This tension wave moves up the rod until it is reflected on top. Before this wave reaches the top and at  $2L_h/c$  time ( $L_h$  is the hammer length), the compression wave moving up the hammer would reach point A where reflection and transmission will take place. The wave transmitted to the drive rod is in tension and its value from Equation (3.6) is  $0.148\sigma$  and the wave reflected down the hammer is also in tension and its value is  $0.08\sigma$  (Fig. 3.4e). Shortly after that the wave reflected at the juncture E will reach point A and again transmission and reflection take place. From Equations (3.5) and (3.6), the reflected and the transmitted waves are both in

tension and their values are  $0.185\sigma$  and  $0.102\sigma$ , respectively (Fig. 3.4f). The upward and the downward moving tension waves superimpose on each other to give a total value of  $0.62\sigma$ . The original downward moving compression wave ( $0.77\sigma$ ) will be reduced by  $0.62\sigma$  and the result is a downward moving compression wave of value  $0.15\sigma$ . Again transmission and reflection takes place at the juncture E. The resultant transmitted wave is still in compression of value  $(1.373)(0.15\sigma) = 0.206\sigma$ . The downward moving tension wave ( $.185\sigma$ ) is reflected as a compression wave of value  $0.07\sigma$  which moves up the rod until it is reflected on top as a compression wave. When it reaches the juncture E it repeats the cycle of reflection and transmission as described earlier.

Since at the top, and at the bottom, one can see irregularities in the hammer geometry, many small reflections and transmissions will take place in these regions. Due to these facts, a thorough description of the wave propagation in the hammer is very complicated and frustrating. Superposition of waves will in some instances cancel their effects, and a consideration of waves generated in the hammer longer than the  $2L/c$  time of the hammer is believed to be unnecessary. Reflections and impacts will also cause losses in wave intensity, and the overall effect of waves in the hammer will therefore diminish quite rapidly.

The signals sensed by the transducers will at all times be dependent on the superposition of waves passing this section. A blow will first be sensed when the wave transmitted down through section E passes the transducers. Now, depending on the length of rods, a reflection from the bottom or from the top will get to the location of transducers, and their intensity will be superimposed on the ones existing. A theoretical estimation of the wave sensed by the transducers in a 20 ft long rod is shown in Figure 3.5 along with a plot of stress and velocity waves from experimental data.

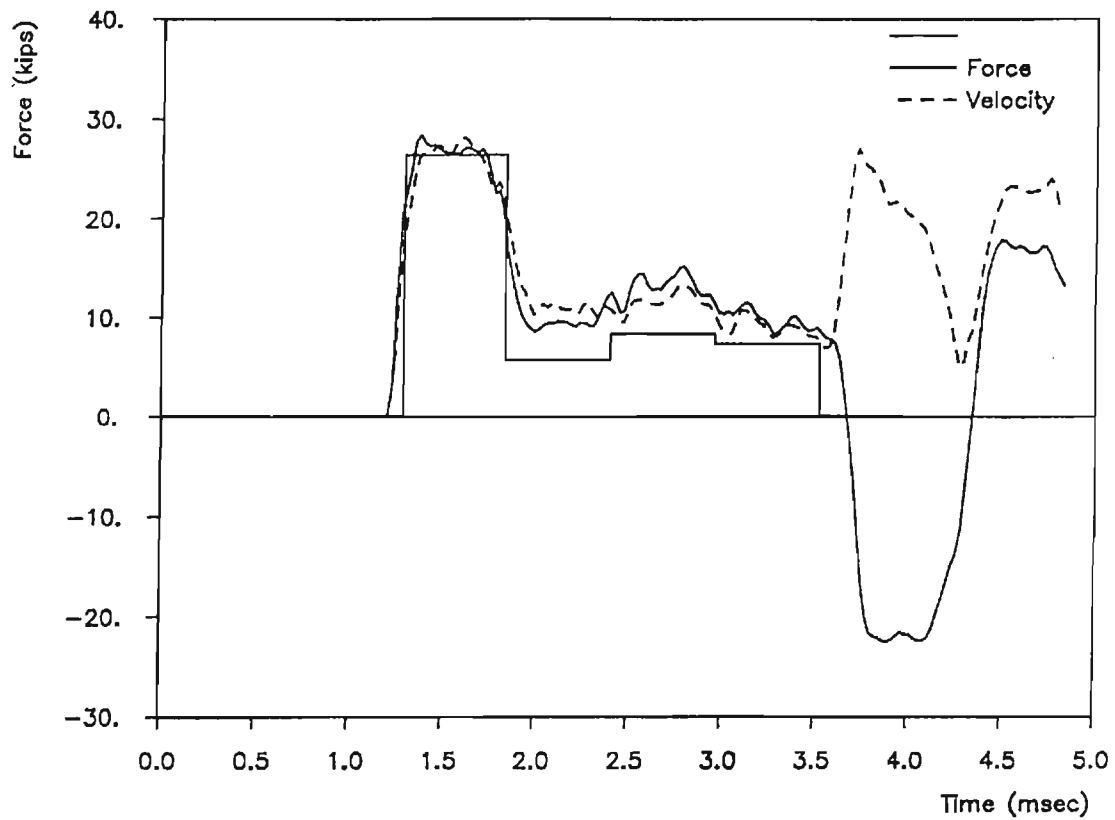


Figure 3.5: Theoretical Wave Form Against Experimental Data.

The force will oscillate about its static value, with smaller and smaller intensity after the impact forces cease, and gradually damp out. For an actual rod in the SPT, the velocity will oscillate about the value prescribed by Newton's second law since it is not fixed on top, but moves some distance into the soil.

## CHAPTER IV

### MEASURING AND PROCESSING EQUIPMENT

#### 4.1 Introduction

The SPT is a dynamic soil exploration test, and the understanding of the SPT requires an understanding of its dynamics. This involves an investigation of the dynamic interaction between hammer, drill rod, sampler and soil. The standard penetration number is dependent on the energy delivered to the sampler (Schmertmann and Palacios 1979). This energy is determined by the velocity of the hammer at impact, and can be determined, if measurements are made on the drill rod by Eq.2.2,

$$E(t') = \int_0^{t'} F(t)v(t)dt$$

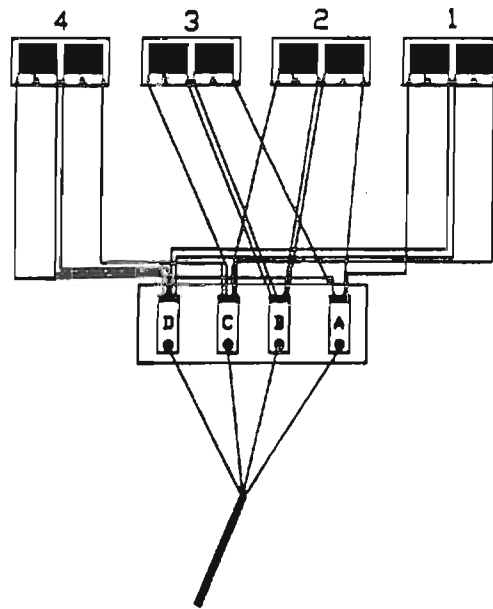
Force and velocity are denoted by  $F$  and  $v$ , respectively, where the measurements are made above the ground surface as a function of time during a hammer blow. The force and velocity describes the dynamic motion of a point on the rod. The knowledge of the motion at one point can be transferred to another by the aid of one dimensional wave mechanics. The requirements for getting a quantitative insight of the dynamics of the SPT are to have accurate records of the force and velocity as a function of time at a point on the rod. By measuring these quantities in the rod, and not the velocity of the hammer at impact, an accurate measurement of the phenomenon is obtained, and it is not necessary to account for energy losses resulting from the hammer impact and rope friction, heat loss at impact and so on.

## 4.2 Transducer Description

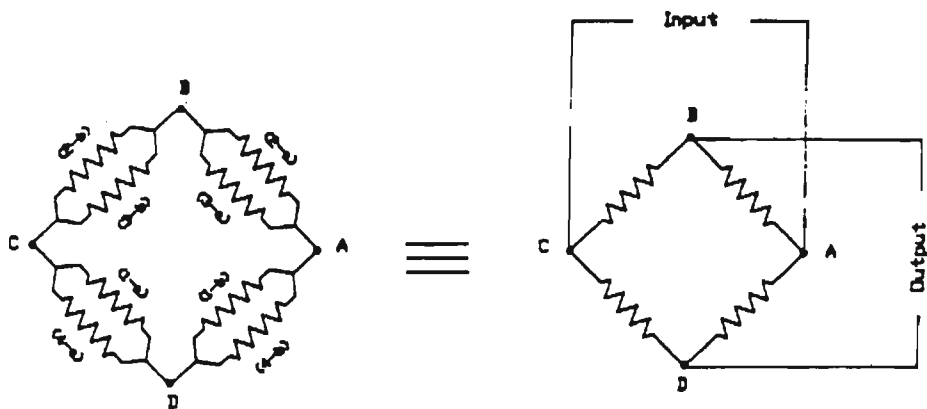
From the pile dynamics area the capability had been developed to measure force and velocity in the pile during driving. Goble and Ruchti (1981) found that the output from the load cell does represent not only the forces in the pile, but also the inertia forces due to the load cell weight. Goble et al. (1975) developed two types of force transducers; one type introduces a force measuring device between the pile and the hammer, and the second type can more accurately be described as a strain transducer. Good accuracy was achieved by mounting strain transducer and accelerometer near the pile top. Because of the similarity between pile driving and the SPT procedures, it is assumed that the same measuring system can be transferred to the hammer-rod system used in the SPT. The measuring system used for piles is described by Goble et al. (1975) and the system used on the SPT system will be described here.

For the force measuring device four 350 Ohm strain gages were mounted directly on a five foot long rod about six inches from the top. Gages were mounted at 90 degree intervals to minimize local bending and to obtain the average force in the rod. Each gage is a two-element gage, one element is parallel and the other is transverse to the axis of the rod. The gages were then arranged into a full bridge and directly calibrated using a bridge amplifier. Schematic of the gage hook-up and the equivalent bridge are shown in Figure 4.1. The rod was then placed in the MTS testing machine for static calibration (Fig. 4.2) and the results shown in Figure 4.3. There is a good linear response within the range tested. A strain gage signal conditioner was used for the amplification of the signals coming from the gages during the calibration.

The acceleration of the rod was measured by mounting two accelerometers diametrically opposite on the rod at about the same level as the strain gages. In this way any bending effects



a) Arrangement of Strain Gages.

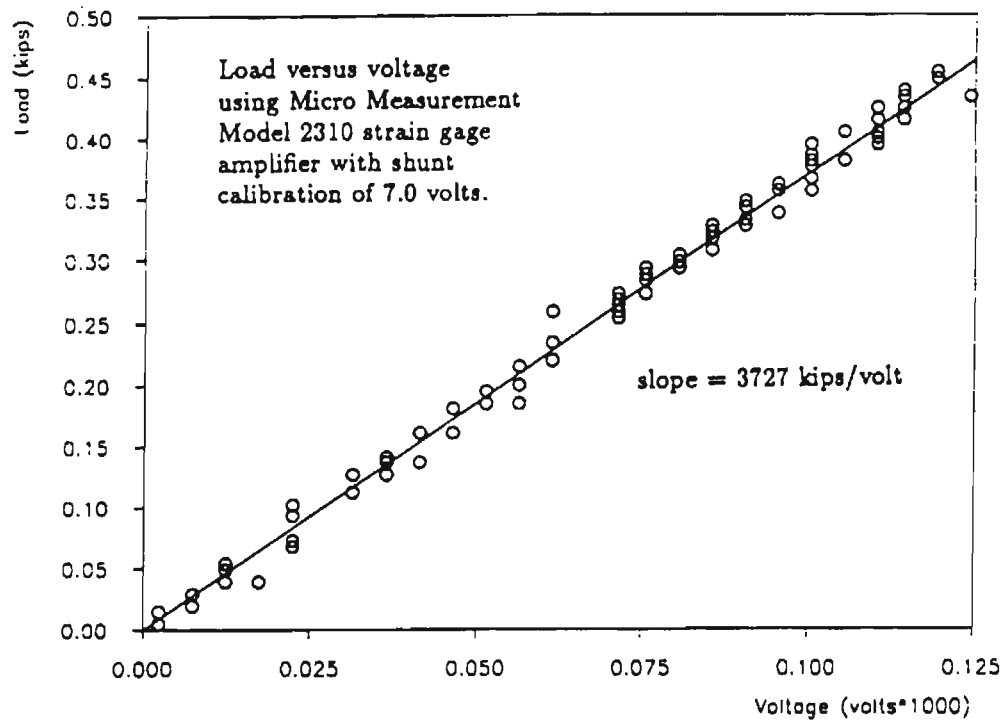


b) Equivalent Bridge.

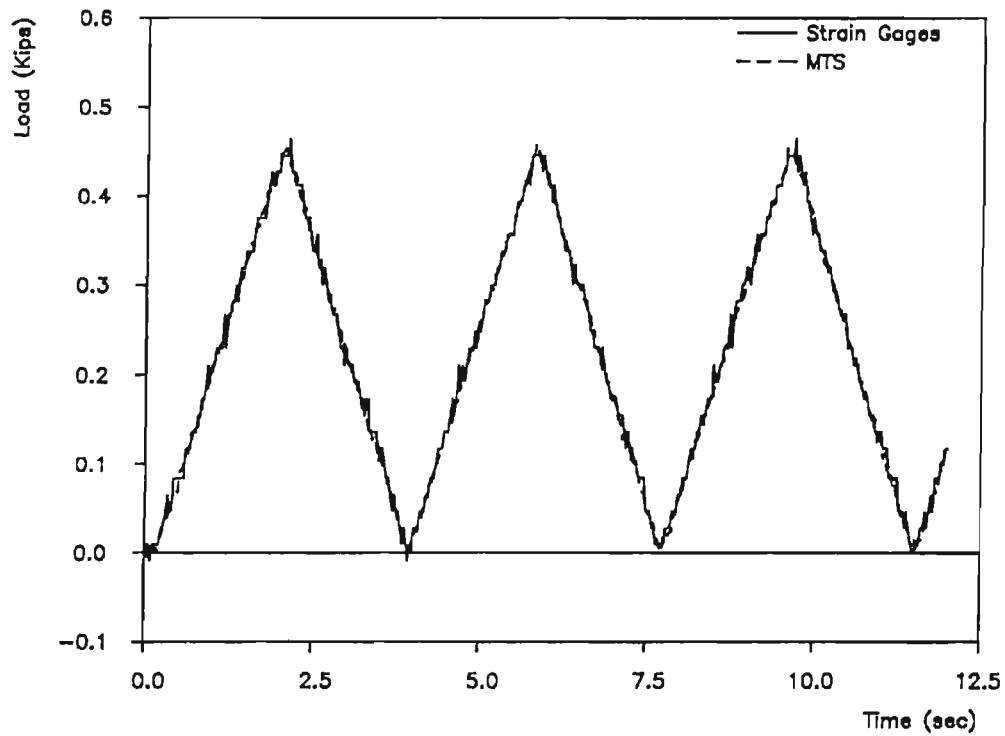
Figure 4.1: Strain Gages Layout.



Figure 4.2: Static Calibration of the Force Measuring Device Using the MTS Testing Machine.



a) Load Versus Voltage.



b) Load from Gages and MTS versus Time.

Figure 4.3: Static Calibration Results of Force Measuring Device for AW-rod.

during a blow could be canceled by taking the average of the two acceleration signals. Commercially available Entran accelerometers were used. The type used is EGCS-240D. The nominal range of this device is from 5g to 5000g for 15 volts excitation and a frequency range of 30% to 50% of the resonant frequency which is 7 kHz. The calibrations of the accelerometers were performed by Entran and the results supplied by them. The technical specifications for the accelerometer are shown in Table 4.1. The rod was shaped in such a way that the accelerometers can be glued to the rod itself on a flat surface.

With these two electronic devices mounted on the rod a fairly convenient and portable way of measuring the dynamic response of the SPT system was available. The rod could be taken out in the field during a regular test and mounted on top of the string of drill rods used, or it could also be used for experimental testing in the laboratory.

### **4.3 Data Processing**

The electronic signals coming from the transducers were amplified and filtered by running them through the strain gage amplifier. The excitation voltage was always set to the same voltage as that used during the calibration performance and, therefore, no changes in the calibration constant is required. The output signals from the amplifier can be recorded by the two data acquisition systems used in this project.

The acquisition systems used are the Computerscope ISC-16 manufactured by R.C. Electronics, Inc. and the Pile Driving Analyzer (PDA) manufactured by Pile Dynamics, Inc. The Computerscope ISC-16 data acquisition system is a fully integrated hardware and software package that consists of a 16-channel A/D (Analog/Digital) board, and external Instrument Interface and Scope Driver software. The package is capable of receiving up to 16 channels of data input at an aggregate sampling rate of up to 1MHz. The hardware is installed into a

## SPECIFICATIONS

MODEL	EGCS-2400 -5	EGCS-2400 -10	EGCS-2400 -20	EGCS-2400 -50	EGCS-2400 -100	EGCS-2400 -200	EGCS-2400 -500	EGCS-2400 -1000	EGCS-2400 -2000	EGCS-2400 -5000
RANGE	± 5g	± 10g	± 20g	± 50g	± 100g	± 200g	± 500g	± 1000g	± 2000g	± 5000g
<sup>1,7</sup> OVERRANGE	± 50g	± 100g	± 200g	± 500g	± 1000g	± 2000g	± 5000g	± 10000g	± 20000g	± 50000g
SENS. mV/g nom.	25	20	10	4	2	1	0.4	0.2	0.1	0.04
<sup>2</sup> RES. FREQ. nom.	370 Hz	500 Hz	800 Hz	1000 Hz	2300 Hz	2800 Hz	3500 Hz	4000 Hz	5000 Hz	7000 Hz

NON-LINEARITY	± 1%
TRANS. SENS.	3% max.
THERMAL ZERO	<sup>4,5</sup> ± 1% F.S./100°F (± 1% F.S./55°C)
THERMAL SENS.	± 2½%/100°F (± 2½%/55°C)
DAMPING	<sup>3</sup> 0.7cr nom.
USEFUL FREQ. RANGE	<sup>2</sup> 30% to 50% Res. Freq.

INPUT IMPEDANCE nom.	2000 Ω typ (1500 Ω min.)
OUTPUT IMPED. nom.	1000 Ω
EXCITATION	<sup>6</sup> 15VDC
COMPENSATED TEMP.	<sup>6</sup> 70°F to 170°F (21°C to 77°C) OPTION 2: 32°F to 140°F (0°C to 60°C)
OPERATING TEMP.	<sup>6</sup> -40°F to 250°F (-40°C to 121°C)
WEIGHT (w/o cable) nom.	Type D: 4 grams Type D1 & D2: 10 grams

<sup>1</sup>Overtime valid at all frequencies. <sup>2</sup>Useful frequency range is 30% of Resonant Frequency minimum, but may be as high as 50%. <sup>3</sup>Damping is nominally 0.7cr at 80°F but can range from 0.3 to 1cr. <sup>4</sup>Zero offset of ± 25mV max at 80°F after warm-up. Lower values available on request. <sup>5</sup>± 2½% F.S./100°F for 5g Model. <sup>6</sup>Other Excitations and Temperature Ranges available on request. <sup>7</sup>Overtime of 10000g available as an option.

Table 4.1: Specifications for Model EGCS-240D Entran Accelerometer, Supplied by Entran.

COMPAQI PC with graphics monitor where the signals could be viewed and then saved on a floppy disk in digital form. A processing program can now use these records to calculate force, velocity and energy in the rod. A flowchart for the program is shown in Figure 4.4. The actual program is written in FORTRAN 77 with interactive data input. In order to clarify the computation of these values the processing program will be discussed in detail.

The digitized data on disk is already sorted out in such a way that each channel is written in a separate column. Amplifier setting and calibration constants for force and velocity must be given first to scale the records. If two accelerometers were used, the average of the two is calculated. Now the zero levels of the two signals must be determined. Some fluctuation in the static state is always present in the transducers, so this variation is averaged for both signals and subtracted from them. When the zero level is determined, the acceleration can be integrated to obtain the velocity. For this process, the trapezoidal method was used. Now using Eq. (2.2) the energy can be computed as a function of time.

An example plot of the results obtained from this program is shown in Figure 4.5. The velocity is multiplied by  $EA/c$  to give the velocity in force units. The record shown was taken on a 20-foot long rod in the laboratory. As can be seen, the graphical plot gives a better description of and insight into the dynamic event of a hammer blow and is a good visual aid in the comparison.

The only disadvantage of the R.C. data acquisition system is the inability to save every blow during a regular SPT operation. But for research work in the lab where the hammer is lifted and dropped manually the R.C. is very useful. For field testing the PDA is more practical.

The PDA was designed originally for pile driving analysis, but because of the similarity between pile driving and the Standard Penetration Test the PDA was used to take measurements during SPT performance. The model used in this project is the GCX. This model has the ability

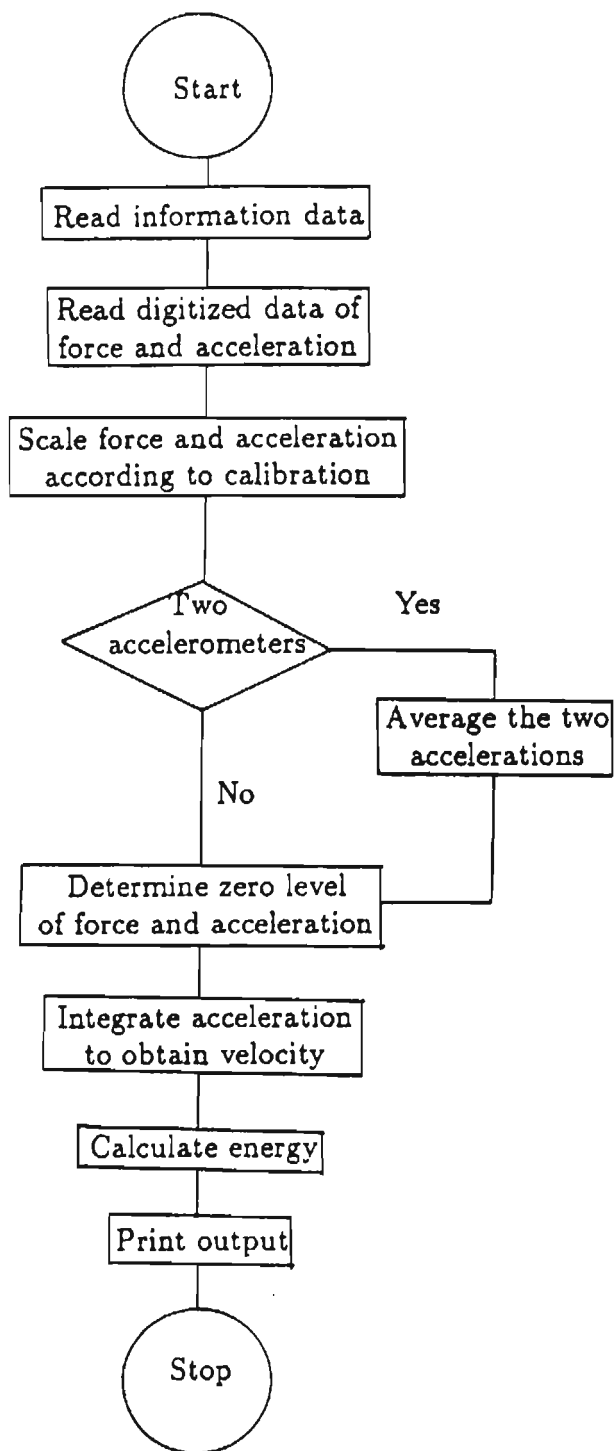


Figure 4.4: Flowchart for Processing Program.

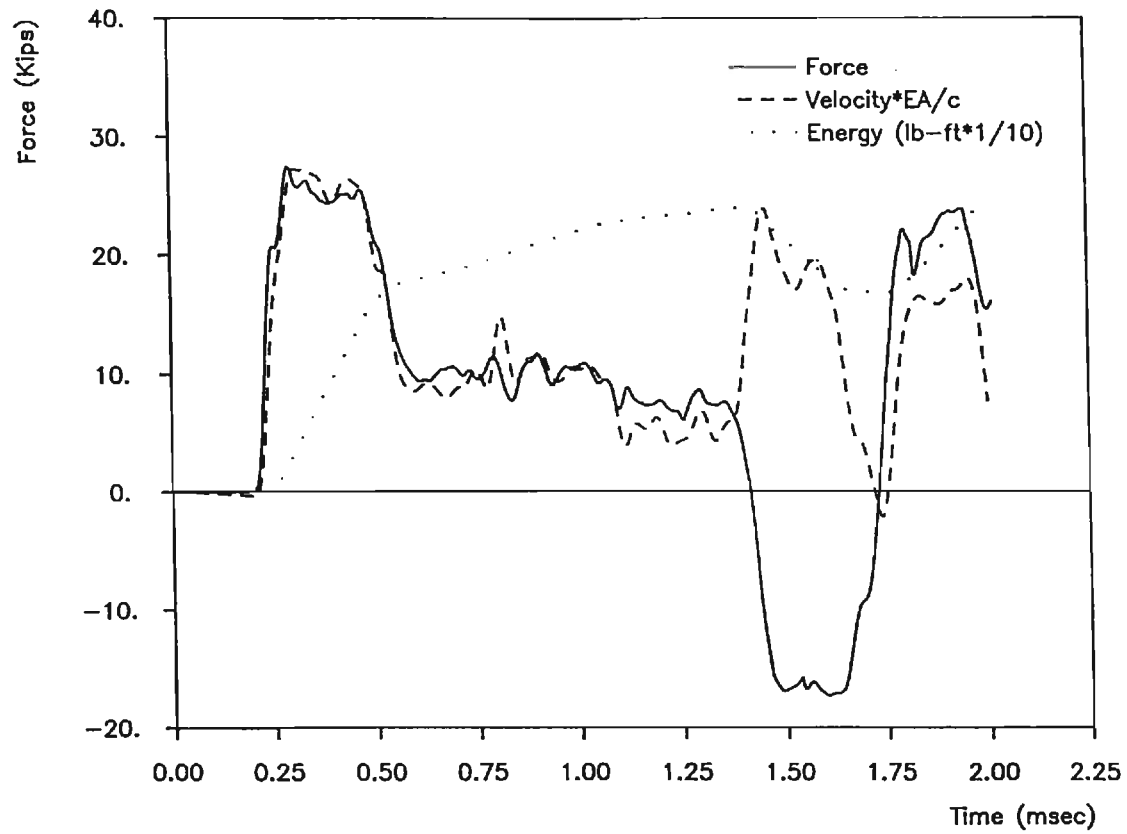


Figure 4.5: Plot of Force, Velocity and Energy of a Record Taken in the Laboratory Using the R.C. Data Acquisition System.

to save every single, second, fifth or tenth blow for up to a total of ninety blows if two channels are used or eighty blows otherwise. The records are saved in a digital form. The saved blows can be sent to the PC then saved on a floppy disk. The PDA does all the required analysis; it scales the force and the acceleration, averages the accelerations (if two channels were used), integrates the acceleration to get the velocity and calculates the energy in the rod either by integrating  $Fv$ ,  $F^2$  or  $v^2$  depending on the selected method. For this analysis force and velocity calibration, impedance ratio  $EA/c$ , and  $l/c$  should be calculated and set properly. Figure 4.6 shows a plot of force and velocity for a record taken on a 20-foot long rod recorded on the PDA. The smoothness of the curves is due to the low pass filter of the PDA.

Force and velocity signals can be viewed on an oscilloscope connected to the PDA; also a printout of certain values such as maximum energy, maximum force, maximum velocity etc. can be obtained. The PDA provides analog output of force, average velocity, average acceleration and velocity, and acceleration from each accelerometer. This analog output can be recorded on an FM magnetic tape recorder, and later processed and analyzed in a more comfortable environment. This has the obvious advantage that records all of the signals, not only force and average velocity, of successive blows taken in the field can be automatically stored. In this way the dynamic event can be recreated in the laboratory.

The tape recorder used for this project was a TEAC R71 with a capacity of recording seven separate channels, simultaneously. Six channels were used for recording of the dynamic event and one channel for flutter compensation; one of the six channels was also used for voice notations. Two channels were used for accelerations, two channels for force and velocity, and the other two channels for force and energy measured by the SPT Calibrator (discussed later.). Any technical information such as the set for each blow, length of rods in hole and site description was recorded on the voice channel for ease in the reproduction process.

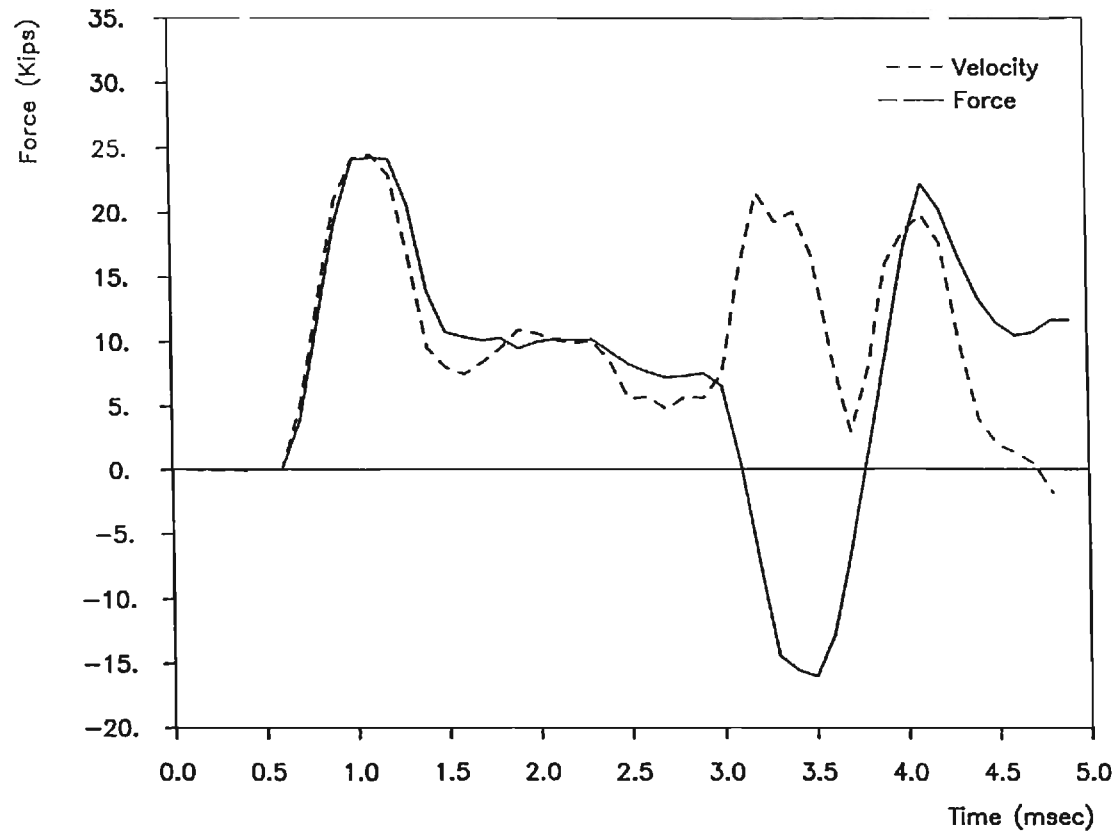


Figure 4.6: Plot of Force and Velocity Record Taken Through the PDA.

The Standard Penetration Test Calibrator is a complete system, manufactured by Binary Instruments, Inc., to measure force and energy in the drill rods during the SPT. The Model 102 SPT Calibrator was used in this project. It consists of a 40,000 pound capacity load cell and an instrument to compute the energy from the dynamic force and the properties of the drill rods, according to the relationship

$$E(t) = \frac{c}{EA} \int_{t_1}^{t_2} F(t)^2 dt$$

where

$E(t)$  = energy in the rod.

$A$  = area of rod cross section.

$c$  = velocity of the compression wave in the rod.

$E$  = Young's modulus for the rod.

$F(t)$  = measured axial force in rod.

$t$  = time from hammer impact.

The displayed energy is computed as a percent of the theoretical 4200 inch-pounds available from the impact of a 140 pound weight falling 30 inches. The load cell was attached to the drill rod at about 2 feet from the point of hammer impact.

The velocity of the hammer was measured by radar and plotted by the Hammer Performance Analyzer (HPA). A picture of the radar and the HPA is shown in Figure 4.7. An output from the HPA taken during a field testing is shown in Figure 4.8. The velocity of the hammer starts from zero and increases until it gets its maximum value at impact. The peak of this plot is the impact velocity. The calibration of the HPA is 2 ft/sec per division. Therefore, the impact velocity shown by this plot is 11.9 ft/sec.

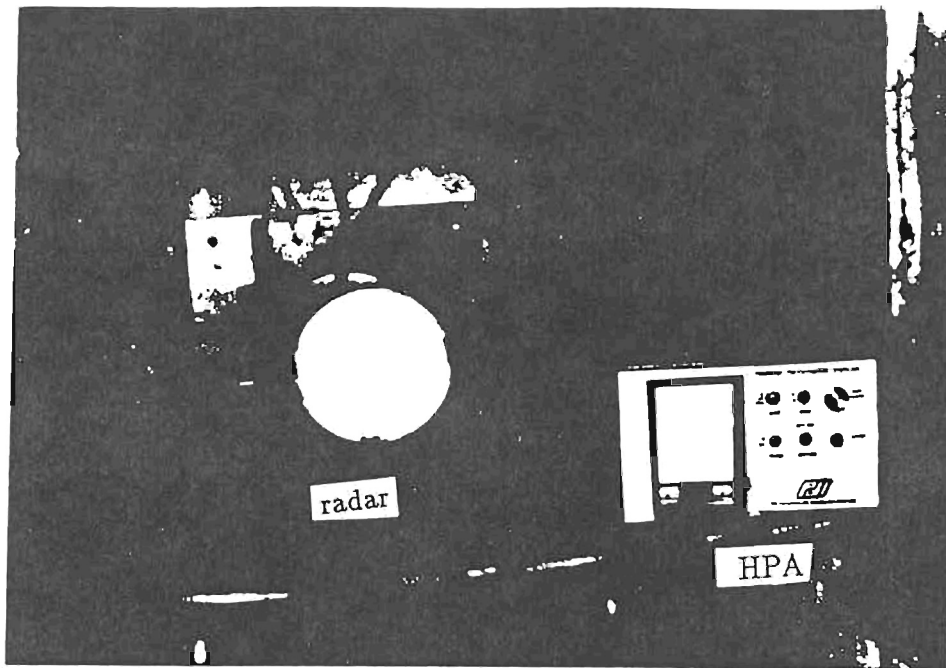


Figure 4.7: Radar and the Hammer Performance Analyzer.

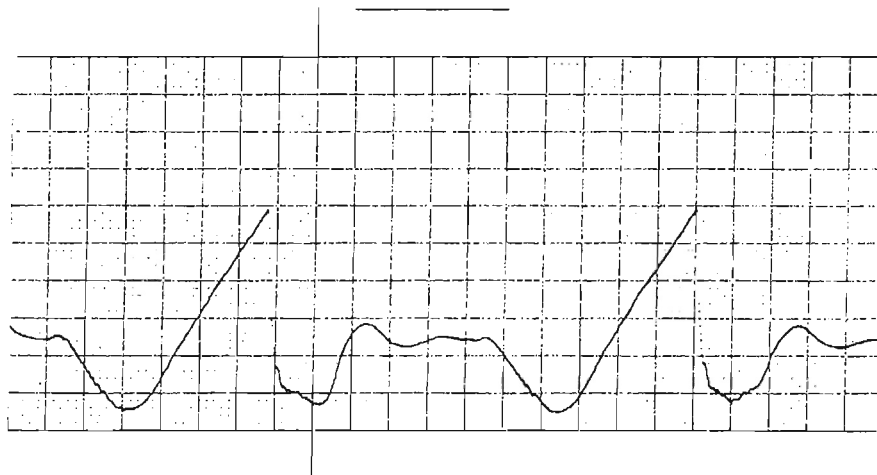


Figure 4.8: Impact Velocity Measurement During an SPT Field Testing.

#### 4.4 Dynamic Calibration

The calibration of the force measuring device was determined under a static load where a good linear response was obtained; and the calibration of the accelerometers was given by Entran. Having this information it was thought that the rod was ready for testing. However, the force and velocity were not proportional due to an error in the calibration constants. The question was; which of the signals is incorrect if not both? This question can not be answered easily from measurements taken during an SPT blow due to the complicated wave behavior in the SPT system. To be able to answer this question the instrumented rod was tested in a simple dynamic test. The test and the results will be described and discussed in detail.

The apparatus is shown in Figure 4.9. The instrumented rod was connected to another two five foot rods to make a total of fifteen feet long rod and then it was suspended by four wires (two at 8 inches and two at 150 inches from the impacted end). A four foot long AW-rod was also suspended by four wires and used as a pendulum hammer. An adjustable guide was used to connect the drill rods and the hammer to the wires. The hammer and the rods were aligned carefully to ensure uniform contact across the striking surface. The signals were taken through the R.C. data acquisition system and the impact velocity was measured by the radar.

The hammer rod was lifted about one foot then allowed to fall freely and impact the rod creating two compression stress waves traveling in the rod and in the hammer simultaneously. Since the hammer and the rod are made of same material and have same cross-sectional area, the impedance ratio  $h$  equals one. Equations (3.5) and (3.6) show that the particle velocities as well as the stresses in the rod and the hammer are equal to half the initial values (i.e half the impact velocity). When the stress wave reaches the free end of the hammer it reflects back as a tension wave with the same magnitude as the incident compression wave which reduces the stresses to zero. At the moment the reflected wave comes back to the point of contact with the drill rod,

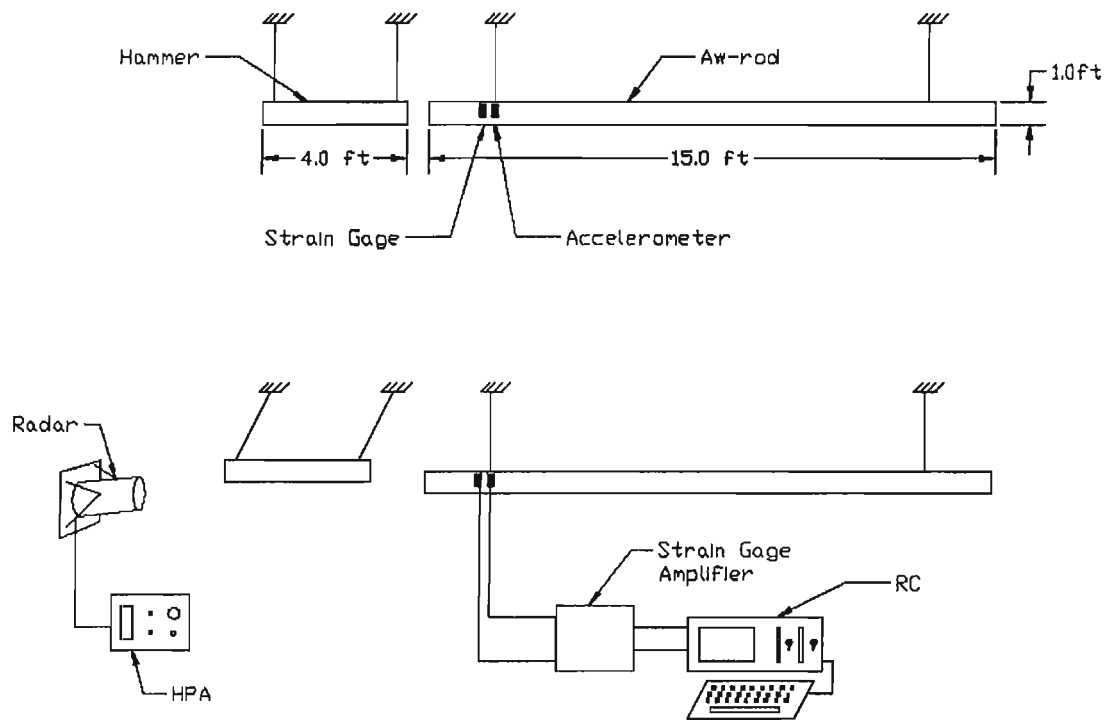


Figure 4.9: Drawing of the Pendulum Test Setup.

the hammer will be unstressed and a reduction in stress between hammer and rod results. Since the waves in the hammer and the rod are equal the stress in the rod becomes zero and thus, a rectangular wave of length  $2L_h/c$  is generated in the rod, propagating with the speed  $c$  ( $L_h$  is the hammer length). The phenomenon is shown in Figure 4.10. The wave then reflects from the free end of the rod and after a time  $2L_r/c$  is again sensed by the transducers ( $L_r$  is the length of the drill rod measured from the gages). The reflected stress wave is a tension wave and shortly after it is sensed by the transducers it reflects from the impacted end of the rod as a compression wave. This compression wave cancels the arriving tension wave and after a time  $1/c$  (twice the length from the transducers to the impacted end of the rod divided by  $c$ ) the strain gage senses a zero stress and stays unstressed for  $2L_h/c$  (until the entire arriving wave passes), then senses the tail of the compression wave.

A different phenomenon is observed for the velocity wave. The velocity reflects from the free end with the same sign and magnitude. Then after  $2L_r/c$  the velocity sensed at the accelerometer equals the incident velocity or one half the hammer impact velocity. It immediately reflects from the impacted end with same sign and magnitude. After  $1/c$  the transducer senses double the velocity for a time equals to  $2L_h/c$  then senses the tail of the reflected wave before it drops to zero. A theoretical form of the stress and velocity waves that are sensed by the transducers is shown in Figure 4.11.

The theoretical impact velocity due to a fall of 12 inches is 8.02 ft/sec (calculated from  $v = \sqrt{2gh}$ ). But for accuracy, the velocity used to calculate the waves in the rod was taken from the radar measurements. Figure 4.12 shows the output obtained from the HPA. The impact velocity for this blow is about 8.05 ft/sec. The records from the transducers and the theoretical form of the stress and velocity waves are shown in Figure 4.13. Velocity1 and Velocity2 are the velocities computed from the accelerations taken from the two accelerometers

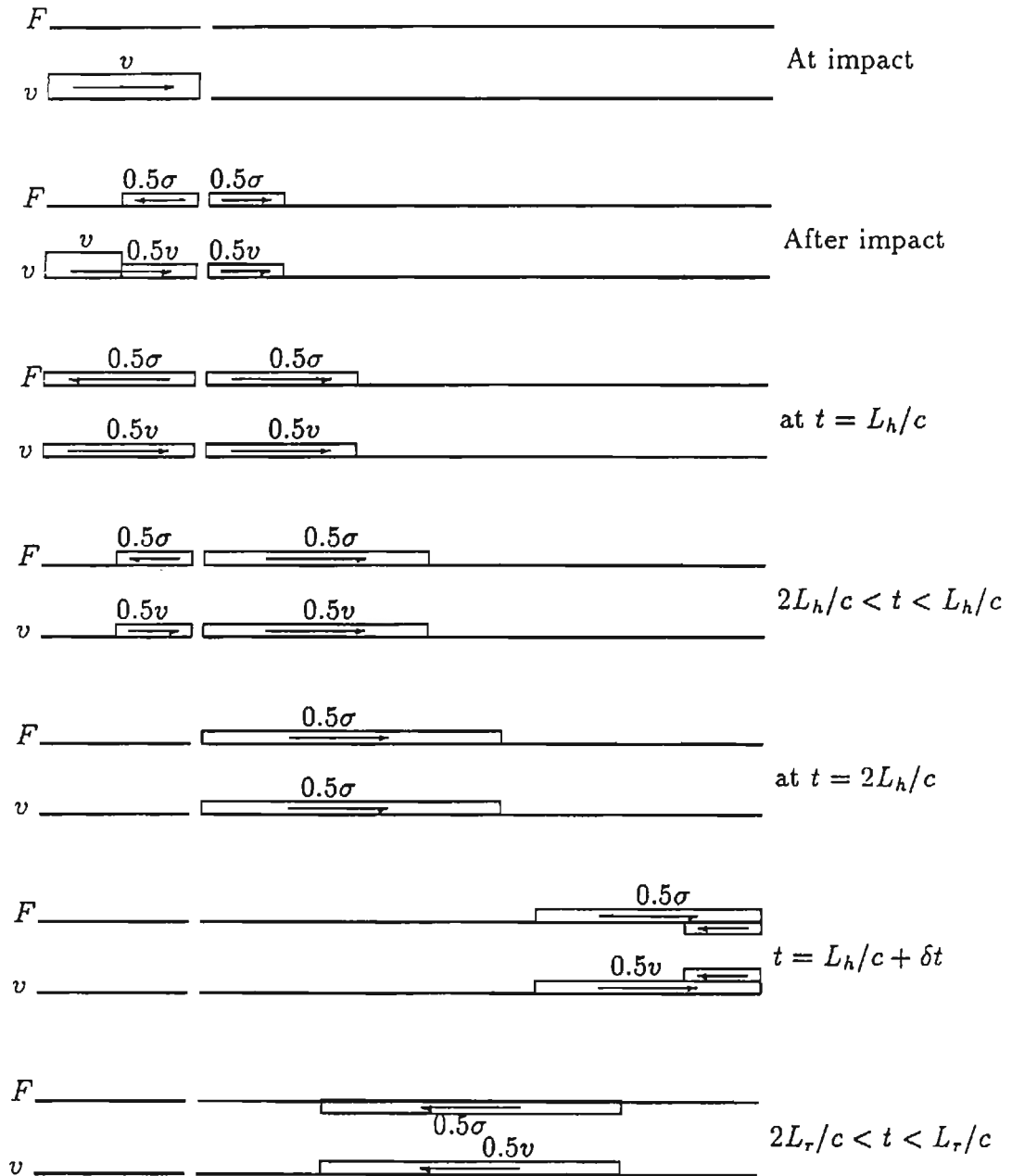


Figure 4.10: Wave Propagation in the Pendulum Test Performance.

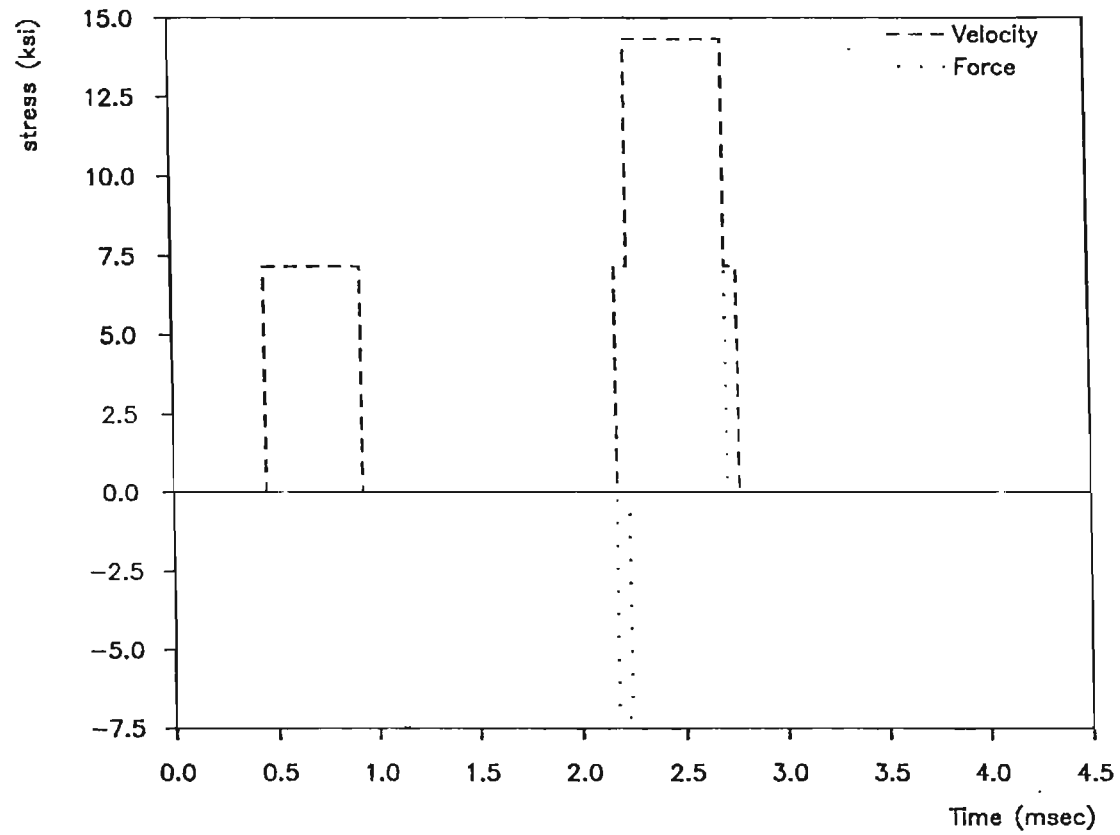


Figure 4.11: Theoretical Behavior of Stress and Velocity Waves in the Pendulum Test Performance.

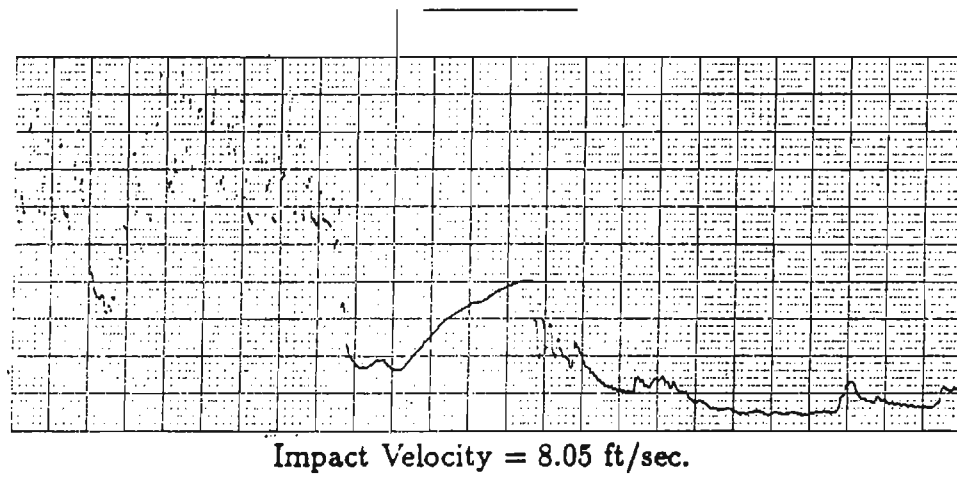


Figure 4.12: Measurement of the Impact Velocity.

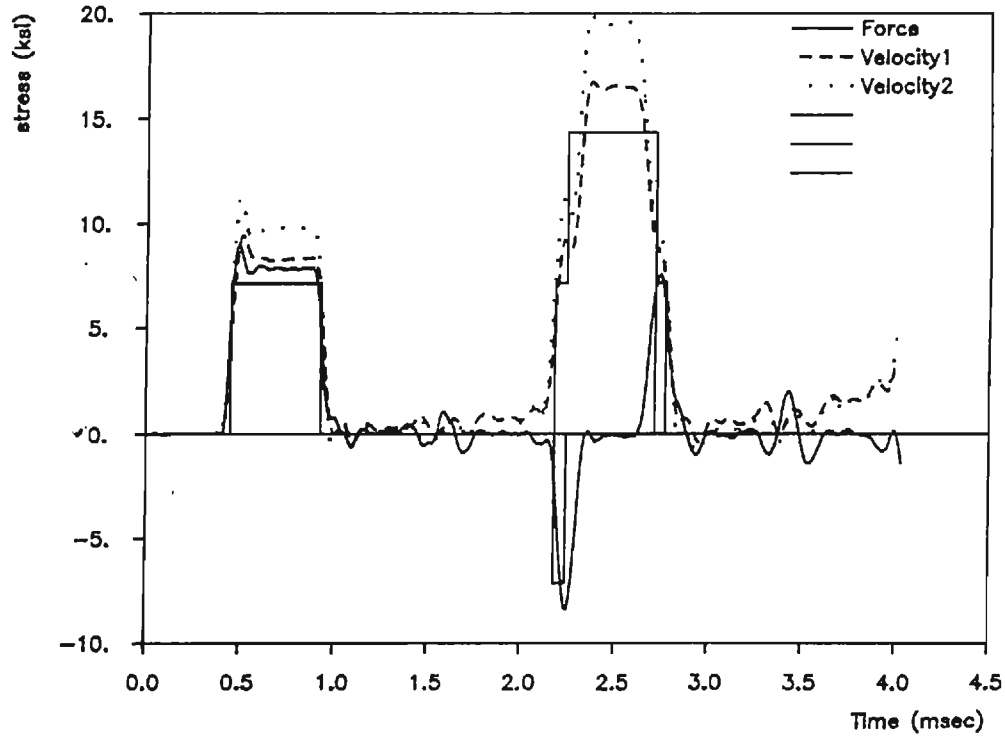


Figure 4.13: Stress and Velocity Records in Comparison with the Theoretical Form.

for the same blow. These results are obtained by using the static calibration constant for the force and the calibrations provided by Entran for the velocity. But as can be seen that the stresses as well as the velocities are higher than the theoretical waves which are calculated using the measured impact velocity. Therefore, new calibration constants are required. The calibration for the force was decreased by 3.4% to become 3600 kips/volt instead of 3727 kips/volt. The calibrations for the accelerometers were increased by 15% and 27% to become 0.0447 and 0.0456 *mv/g* instead of 0.038 and 0.0333 *mv/g*, respectively. The new calibration constants were used to calculate the stresses and the velocities of the same blow and the plot is shown in Figure 4.14. There is a very good proportionality between force and velocity; also a very good match with the theoretical form.

#### 4.5 Frequency Response

The metal to metal impact in the SPT produces signals with some very high frequency content. In order to reproduce the actual event, the frequency response of the measuring and processing system as a whole must be such that it can handle the significant part of these frequencies. The sensitivity and frequency response of the measuring system is determined not only by the transducers but also by the strain gage amplifier and the data acquisition system. The strain gage amplifier used has a low pass filter of 10kHz, while the frequency range of the PDA is 1.2 kHz. This means that the signals taken through the PDA will have a maximum frequency content of 1.2 kHz, and the PDA will therefore act as a low pass filter. The frequency contents of signals taken through the RC data acquisition system depends on the amplifier filter selection, and it can be as high as 10 kHz. From (Oran 1988) one finds that, in order to represent the actual analog curve exactly with a digital record, it is necessary to take samples of the analog signal at a rate greater than twice its highest frequency. The highest sampling frequency of the

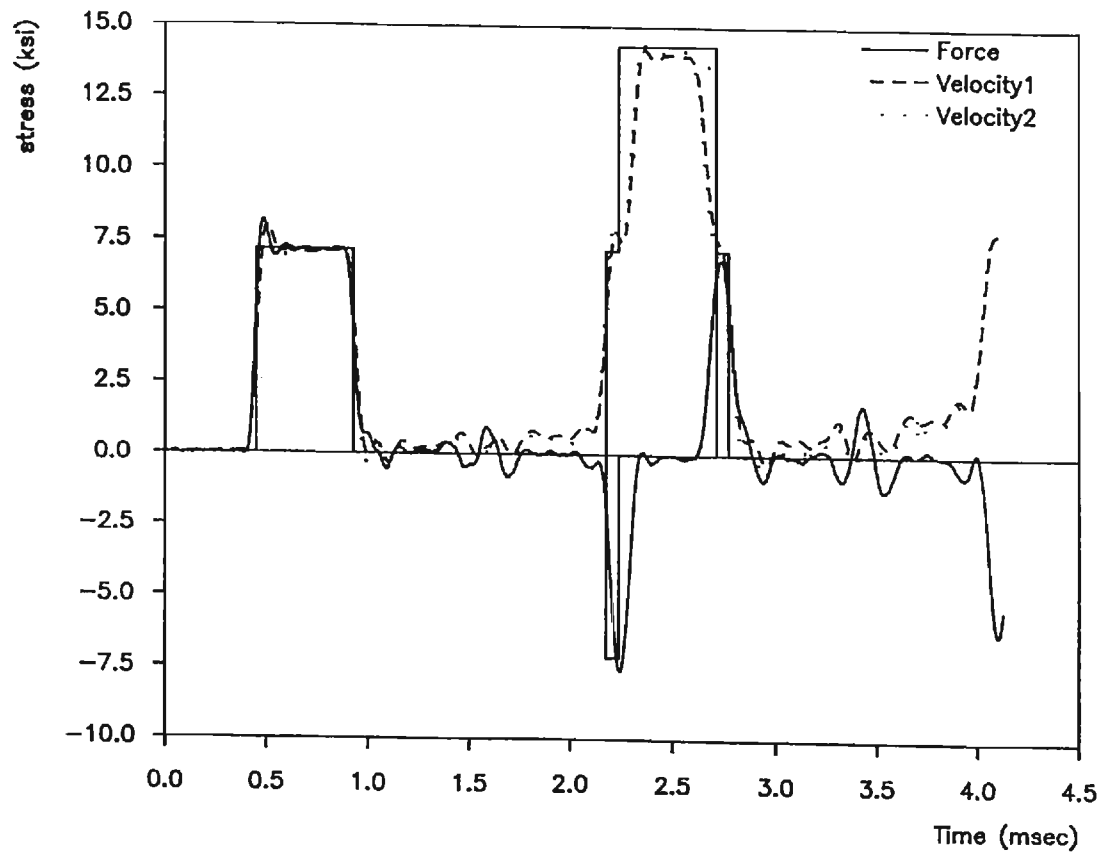


Figure 4.14: Stress and Velocity Waves Using the New Calibration Constants.

RC data acquisition system is 1MHz which is 100 times the highest frequency of the analog signal (10 kHz).

The calibration curves of the accelerometers (See Figures 4.15 and 4.16) show that for the calibration factor provided by Entran the useful frequency is 1.2kHz, and after that the calibration factor becomes a nonlinear function of the frequency. Providing the calibration curve plotted up to 10kHz this function can be determined and used to process signals of 10kHz frequency contents. These signals can be handled by using the RC data acquisition system. To determine the calibration function the accelerometer is considered to act as a single degree of freedom system of mass  $m$ , stiffness  $k$ , and viscous damping coefficient,  $c$ . The natural frequency and the damping ratio of the accelerometers have been determined by matching theoretical output to the experimental data. Figures 4.17 and 4.18 show a plot of the experimental data provided by Entran and the best match of the theoretical output as well as the natural frequency and the damping ratio for this match. Derivation and discussion of the calibration factor is given in detail in Appendix B.

Since the calibration factor is a function of frequency, the acceleration, which is a function of time, must be transferred to the frequency domain. For this process the Fast Fourier Transform has been used. Now, having both the calibration function and the acceleration in the frequency domain, the acceleration can be scaled; then transferred back to time domain using an Inverse Fast Fourier Transfer. A processing program similar to the one discussed before is used. A flow chart of the program is shown in Figure 4.19. Results obtained from this program are shown in Figure 4.20. The plot shows a comparison between the velocity that has been calculated using the calibration factor provided by Entran and the one calculated from this program. The corrections that have been made on the calibration factor has a slight effect on the

velocity signal and thus, the error in using the constant calibration factor provided by Entran up to 10 KHz can be neglected.

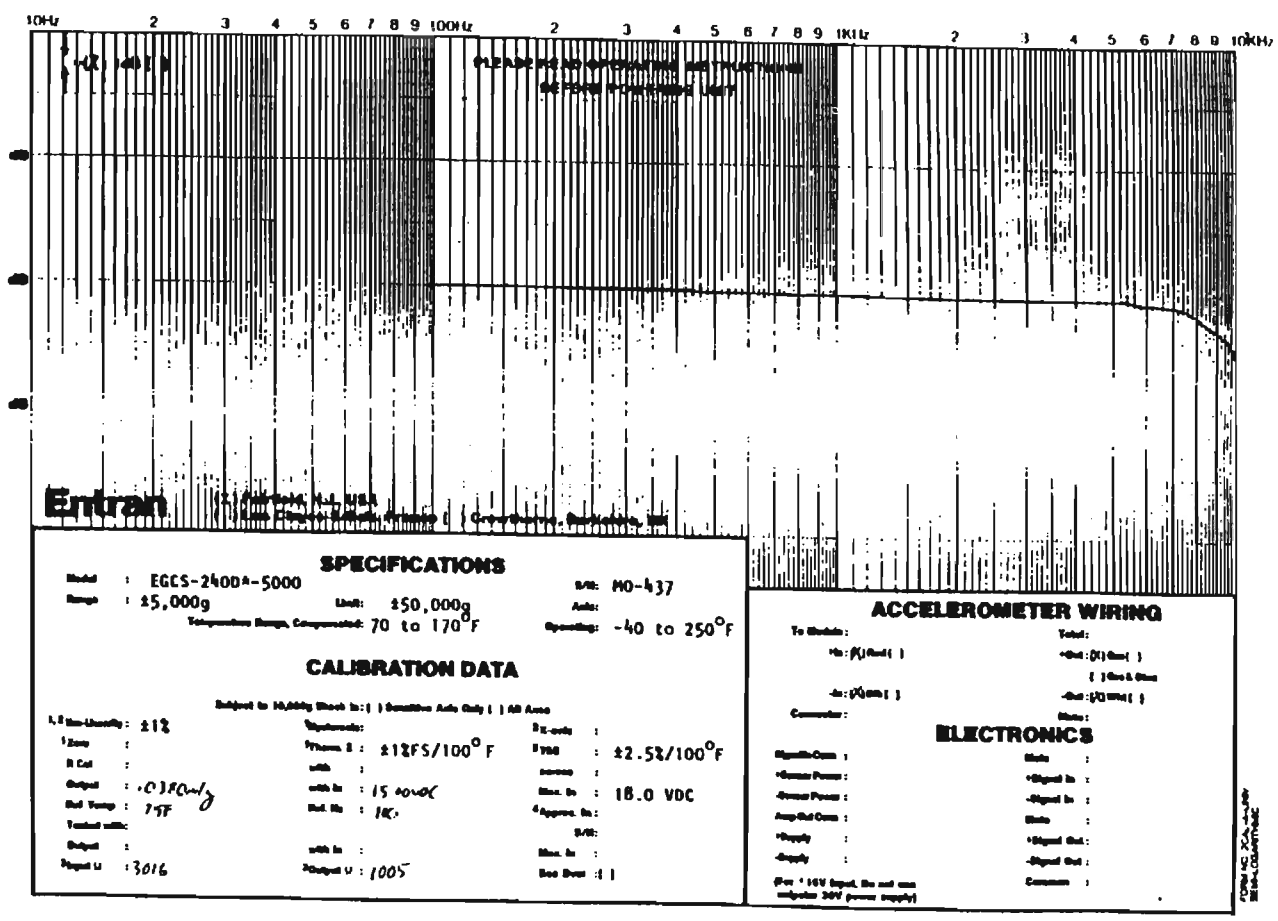


Figure 4.15: Calibration Curve of the M437 Accelerometer.



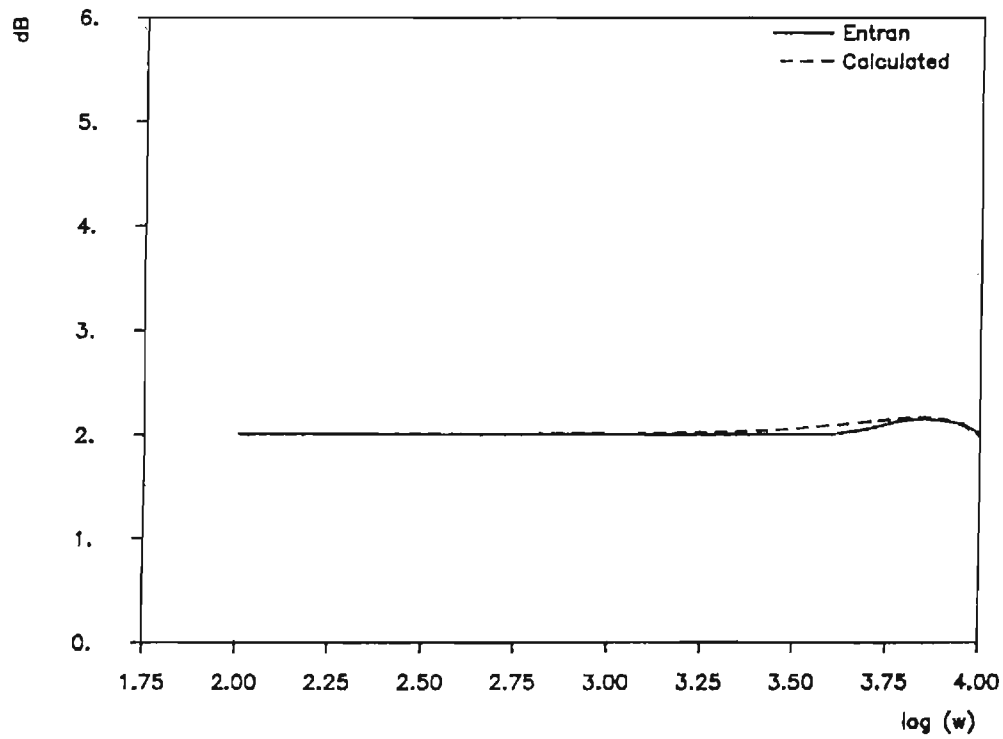


Figure 4.17: Comparison Between Theoretical and Experimental Data of the M437 Calibration curve.

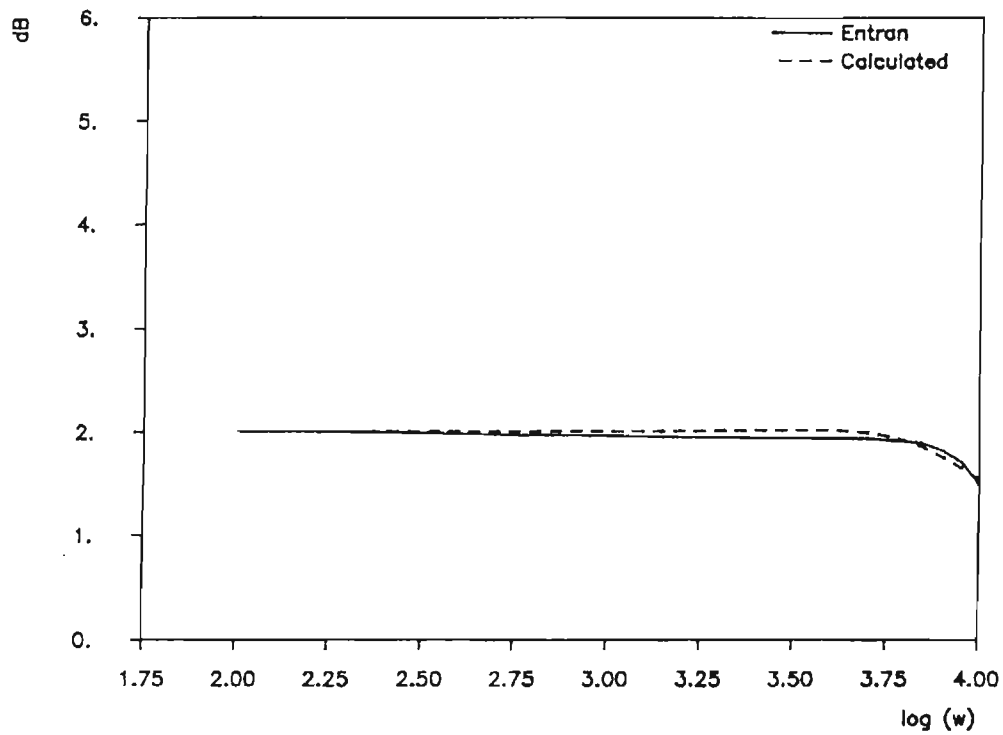


Figure 4.18: Comparison Between Theoretical and Experimental Data of the M438 Calibration curve.

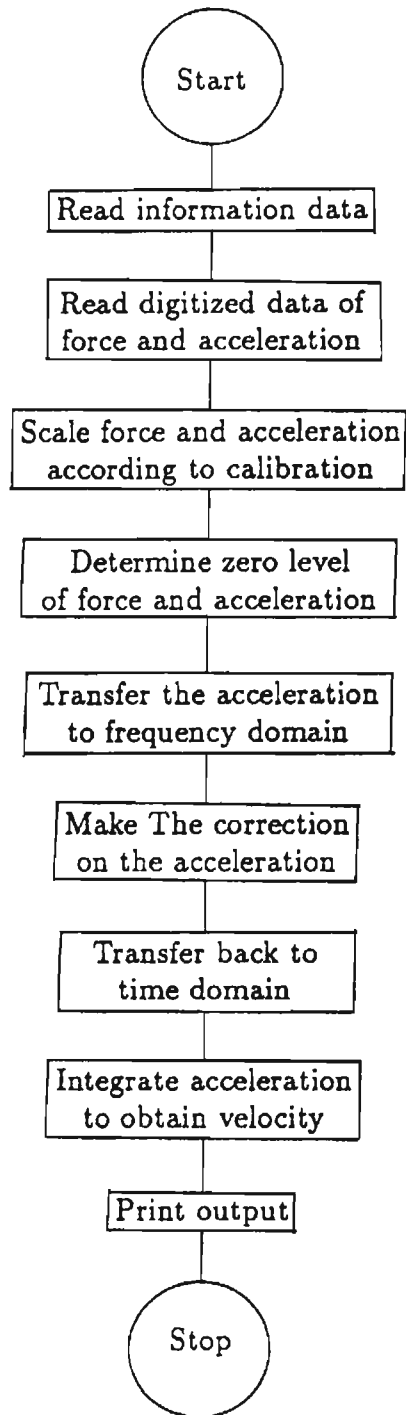


Figure 4.19: Flowchart for the Frequency Domain Processing Program.

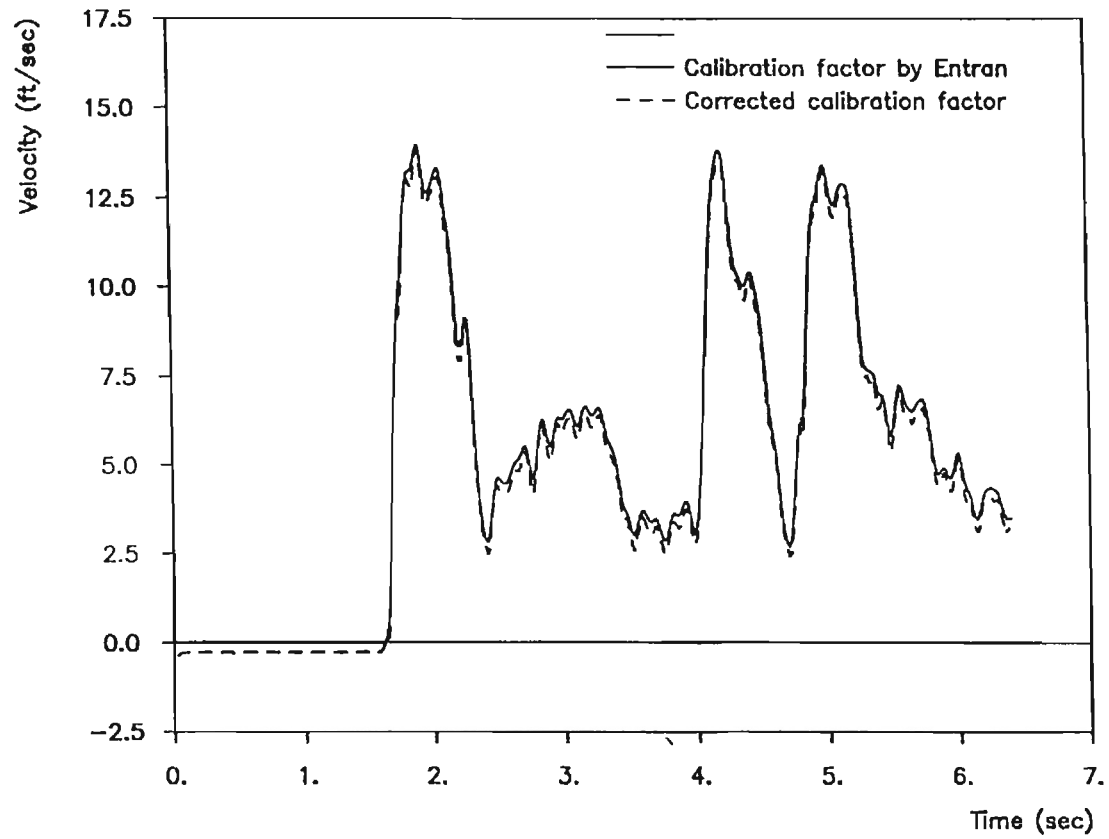


Figure 4.20: Comparison Between the Velocity Calculated Using the Calibration Function and the Velocity Calculated Using the Calibration Factor.

## CHAPTER V

### EVALUATION OF RESULTS

#### 5.1 Laboratory Tests

With the measuring system described in Chapter IV, dynamic measurements can be made on the SPT during a regular test. Before such measurements were taken in the field, the system was tested in the laboratory. A drawing of the laboratory set up is shown in Figure 5.1. The instrumented rod was connected to three five-foot rods to make a total rod length of twenty feet. At the bottom, a six inch long penetrometer was connected to the rod and it rested on a two-inch thick piece of plastic. This makes the length below the transducers 20 feet. In addition to the top measurements, bottom reaction and displacement were also measured. Strain gages mounted on the penetrometer were used to measure the bottom reaction and an LVDT, connected to the bottom, was used for displacement measurements. This system is described in greater detail by Chen (1990). The signal read by the bottom strain gages is the difference between the reflected tension wave and the incident compression wave. In the case of a free rod, the reflected tension wave would be of the same shape and magnitude as the incident compression wave and, thus, the signal from the bottom transducer would be zero. But in this case where a bottom resistance exists, the difference between the incident and the reflected waves is the soil resistance and, therefore, the reading from the bottom transducer is the bottom resistance.

In order to keep the rod standing after a hammer blow, its top was passed through a hole made in a steel plate that was held by two guides (Figure 5.1). The drill rod and the safety

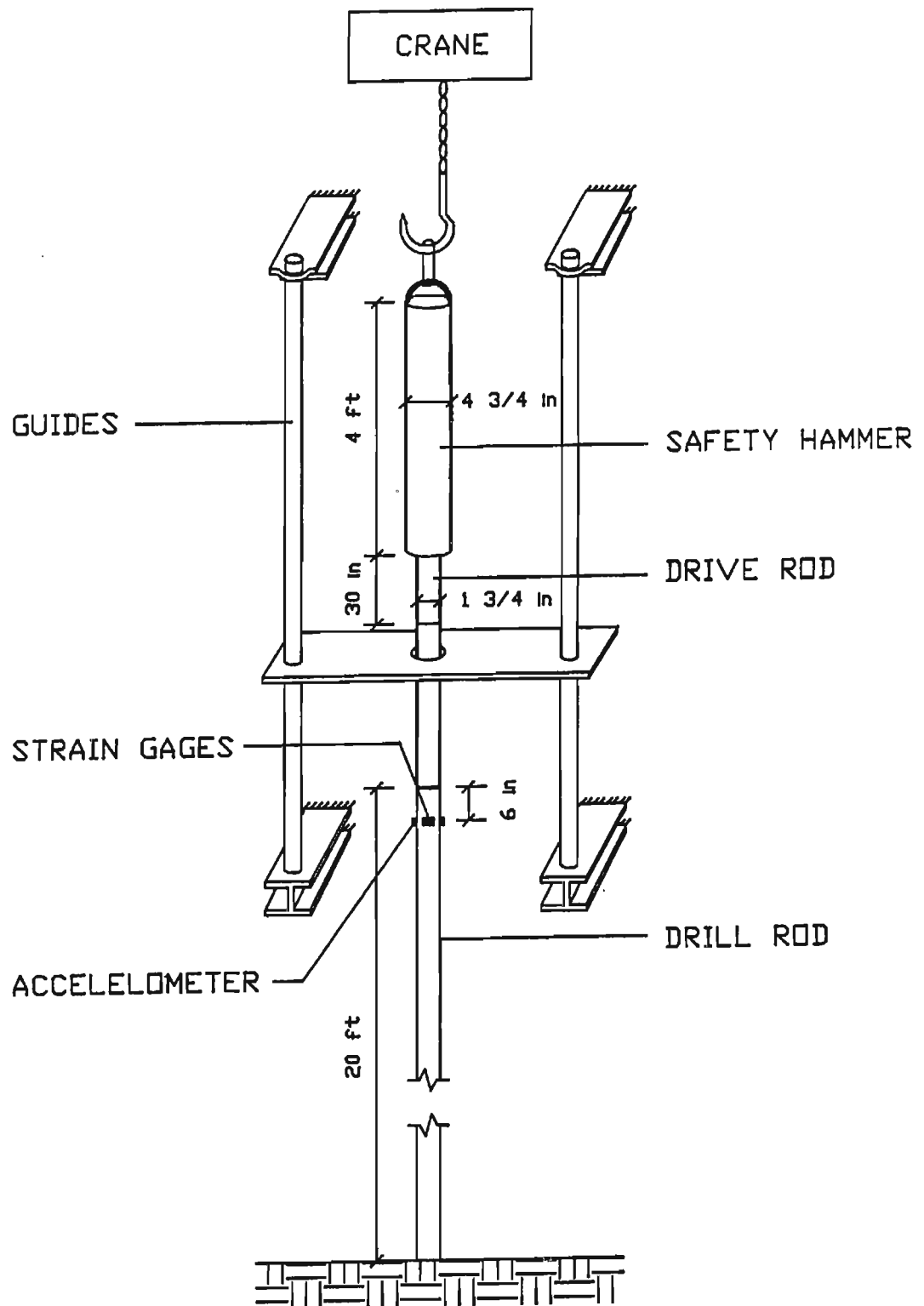


Figure 5.1: Drawing of the Laboratory Testing Setup.

hammer described in Chapter III were used in these tests and the measurements were made by the RC data acquisition system. The hammer was lifted to the prescribed height and then dropped, and measurements of force and acceleration were recorded and processed. Figures 5.2 and 5.3 show the results from two consecutive blows. The velocity is multiplied by the rod impedance,  $EA/c$ , in all figures to give the velocity in force units. Both blows are plotted to just past the  $4L/c$  time of the rod. Each  $2L/c$  time interval including the beginning of the record is marked on the time axis.

Focusing now on Figure 5.3, the proportionality between the two curves up to the  $2L/c$  time is good. A rapid rise in both force and velocity is observed, but the rise time of the velocity is greater than that of the force. This indicates that the frequency content in the force signal is higher than that in the velocity signal. The average magnitude of the first peak is about the same as the theoretical value, 26.4 kips. The length of this peak is the  $2L/c$  time of the drive rod and after that time it decreases to about 8 kips and then oscillates about this value to the  $2L/c$  time of the rod. At that time, the force rapidly becomes negative due to the reflected tension wave coming from the bottom while the velocity shows an increase in magnitude as expected. The same comments also apply to Figure 5.2.

From the energy curve, it can be seen that the energy delivered to the rod reaches its maximum at the  $2L/c$  time. The magnitude is 298 lb-ft or 85% of the 350 lb-ft theoretical energy calculated from the ram potential energy before dropping. The plot also shows that 70% of the maximum delivered energy is transmitted after the  $2L/c$  time of the drive rod. Calculation of the energy absorbed by the soil needs additional measurements of force and velocity at the bottom; such measurements and calculations are discussed later.

With these measurements the bottom resistance, velocity and displacement can be calculated using the methods described in Section 2.6. This type of calculation was done using

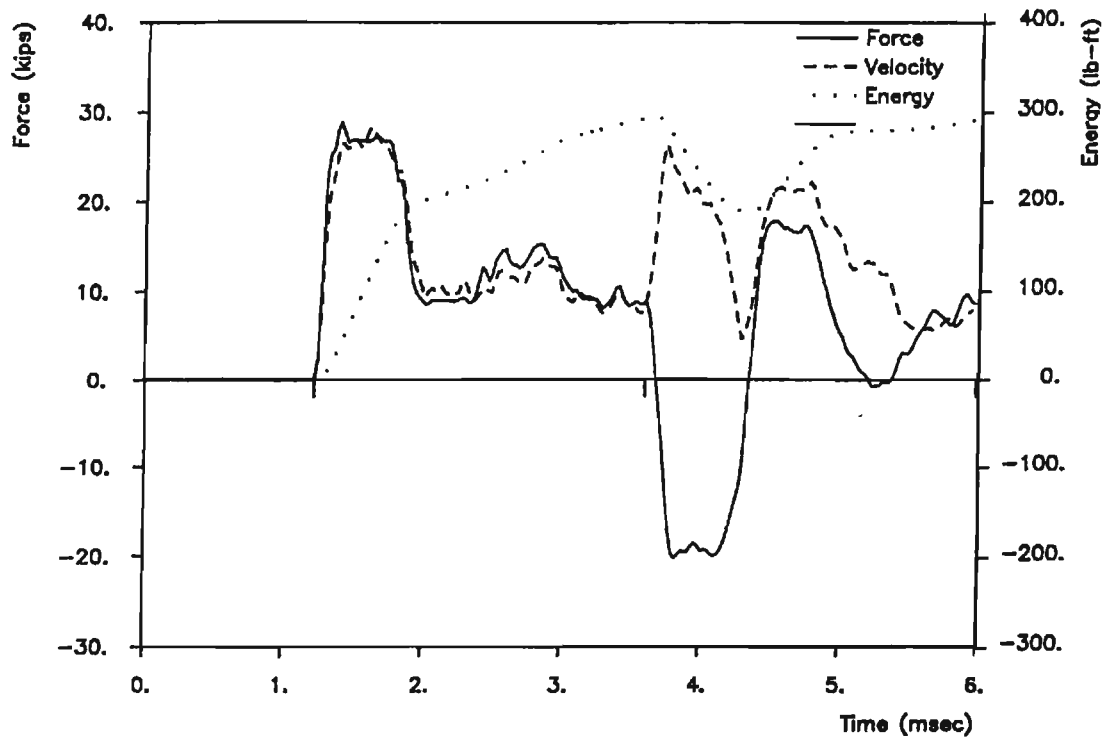


Figure 5.2: Laboratory Test Results, Test # 1.

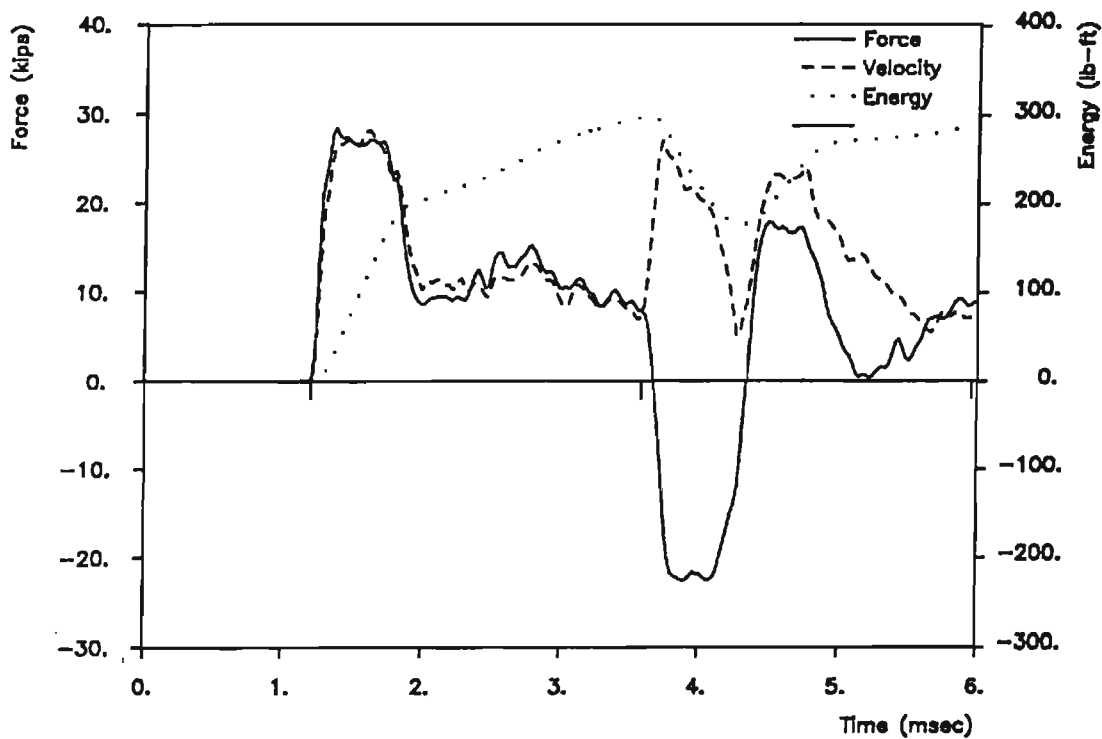


Figure 5.3: Laboratory Test Results, Test # 2.

the record shown in Figure 5.3. The free rod solution was obtained by substitution of the measured velocity in Equation 2.3. It was plotted on the same graph with the actual measured force in Figure 5.4. The difference represented by the shaded area in Figure 5.4 is the Delta Curve,  $F(t)$ , described in Section 2.6. Now, by substituting the values of  $F(t)$  into Equation 2.5, the bottom reaction is obtained and the plot is shown in Figure 5.5 along with the measured one. The spikes in the calculated bottom reaction are due to the difference in the frequency contents in the force and the velocity signals, but otherwise the two curves follow the same path. After calculating the bottom reaction, the bottom velocity can be calculated from Equation 2.6 then integrated to obtain the displacement (Eq. 2.7). The plot of the calculated and measured displacement along with the bottom velocity are shown in Figure 5.6. The displacement curves do not follow the same path, but the final displacement compare very closely.

### 5.1.1 Energy Absorbed by Soil

At any point on the rod, at any time, the force and the velocity in the rod have the value of the instantaneous sum of all incident and reflected waves reaching that point at that time. The top transducers provide a record of the incident compression wave, but only until its cutoff by the reflected tension wave shortly before  $2L/c$ . At the bottom, the force is measured by using the strain gages mounted on the penetrometer and the velocity is measured by mounting an accelerometer on the rod at one foot from the bottom. Shortly after  $L/c$  time the bottom force transducer provides a record of the subtraction of the reflected tension wave from the incident compression wave while the accelerometer provides the addition of the reflected and the incident waves. By subtracting the bottom force record from that of the top, one obtains the force in the reflected tension wave and by subtracting the top velocity record from that of the bottom, the velocity in the reflected wave would result. Now with the force and velocity records from the

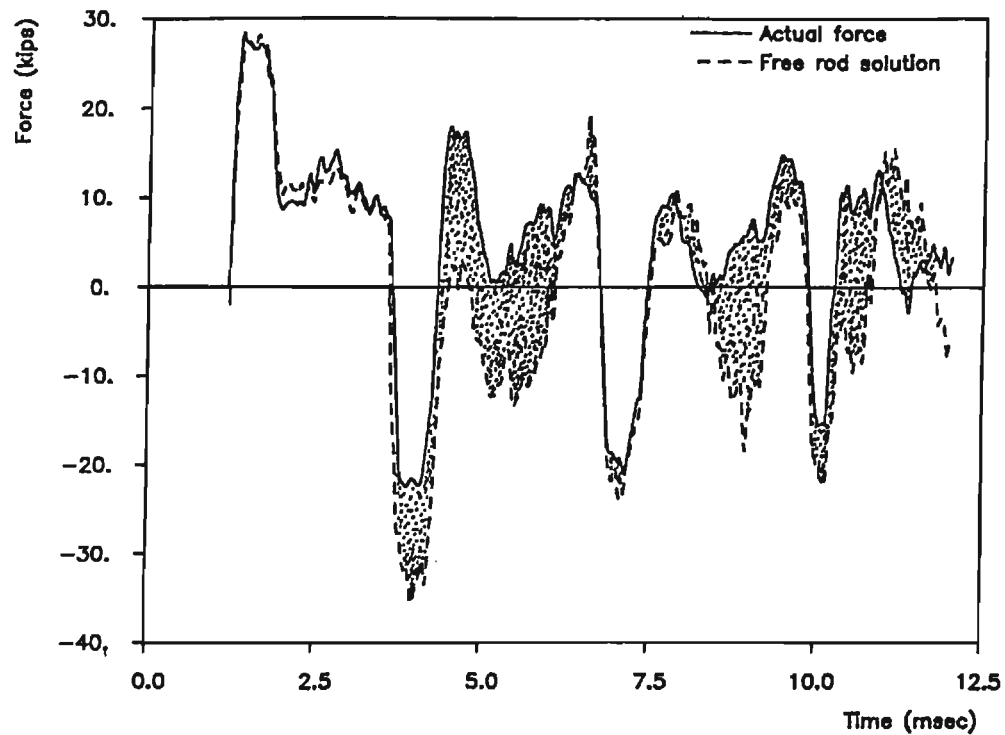


Figure 5.4: Comparison Between the Actual Rod and the Free Rod Solution.

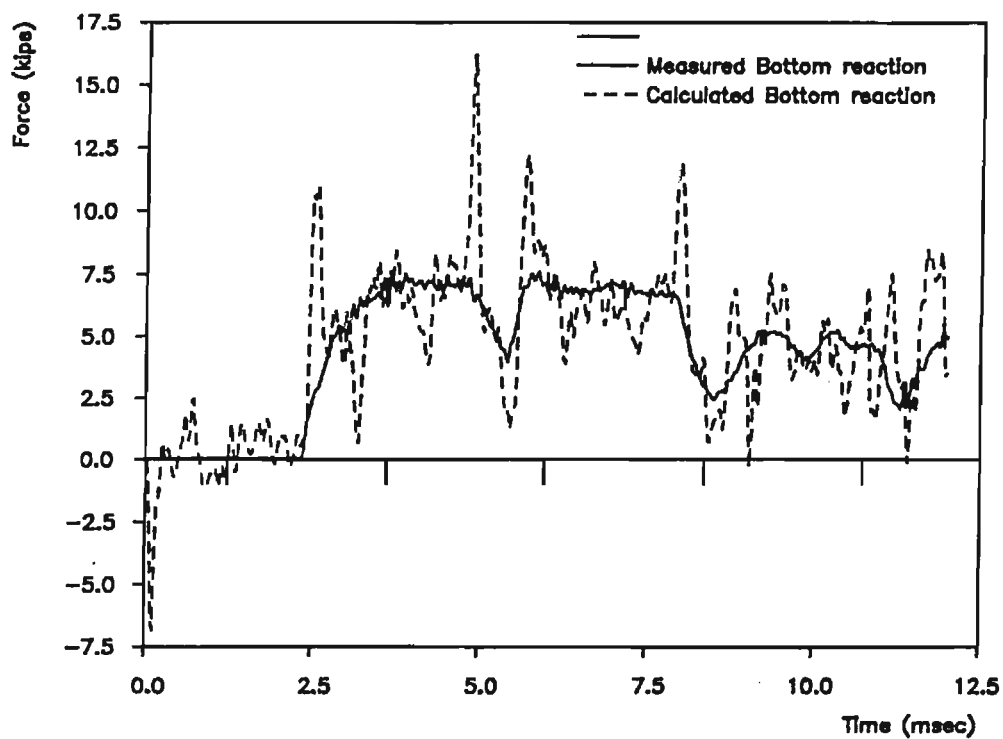


Figure 5.5: Comparison Between Calculated and Measured Bottom Reaction.

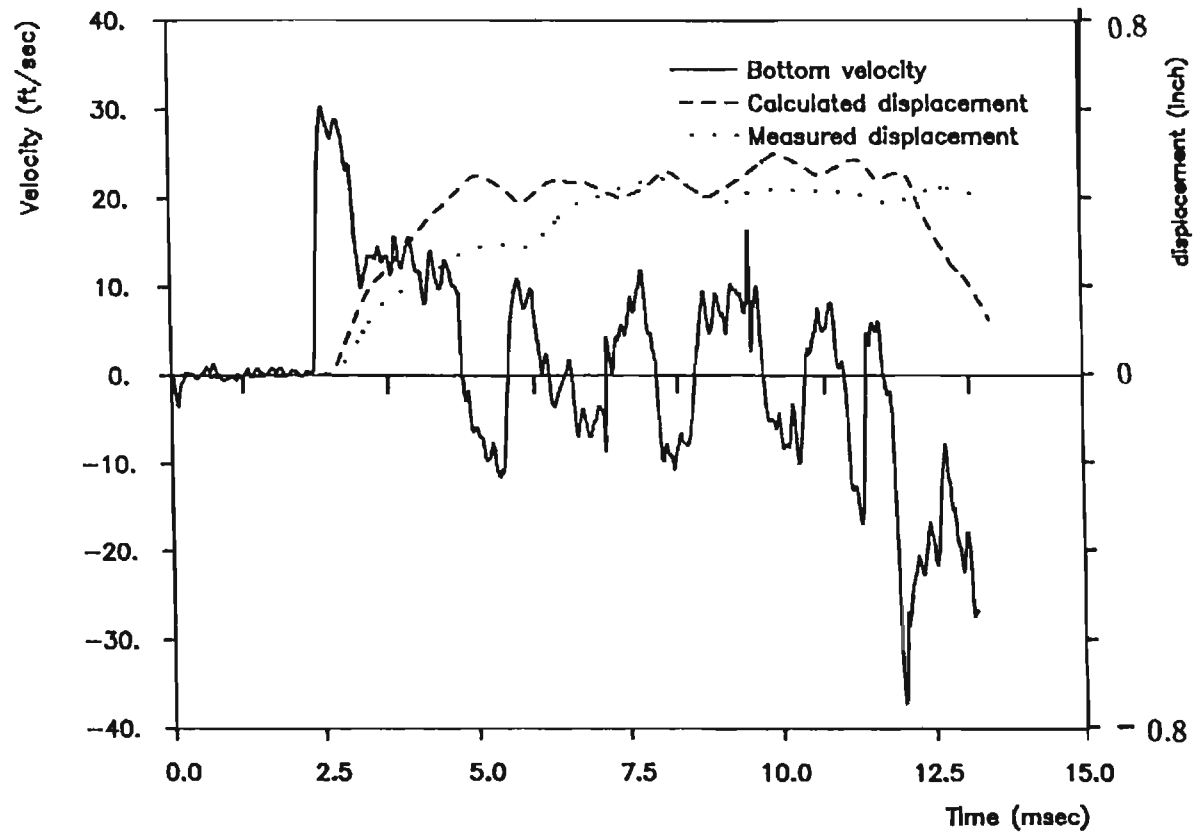


Figure 5.6: Bottom Velocity and Comparison Between Calculated and Measured Displacement.

top transducers one can use Equation 2.2 to calculate the incident compression wave energy entering the rod. And after calculating the force and the velocity in the reflected wave, one can use the same equation to get the energy in the reflected tension wave. By subtracting these two energies, the energy absorbed by the soil is obtained.

Figures 5.7 through 5.11 show the plots for an example of applying the analysis described above. Figure 5.7 shows the force and the velocity records obtained from the top transducers along with the energy in the incident compression wave. Figure 5.8 shows the superposed force records obtained from the top and bottom transducers and Figure 5.9 shows the same plot for the velocity records. The plot of the bottom records is shifted back by  $L/c$  time so that a better comparison can be made. The force and the velocity in the reflected wave, obtained by the subtraction discussed before, in addition to the reflected energy are shown in Figure 5.10. The energy delivered to the soil is obtained by subtracting the energy in Figure 5.10 from that of Figure 5.7 and the results are shown in Figure 5.11. In this case, the energy delivered to the rods is 85% of the 350 lb-ft theoretical energy,  $E_{th}$  and the one absorbed by the soil is 42% of  $E_{th}$ .

## 5.2 Field Tests

After good laboratory measurements were obtained, the system was tested in the field during actual SPT operations. Measurements were taken at sites in the Denver area at different depths, with different soil conditions and two different hammers. The CME Automatic and the Pilcon hammers were used in these tests. The load cell for the Binary Instruments measuring system was mounted on top of the instrumented rod which was connected to the drill rod. A picture of the data acquisition systems used in the field and described in Chapter IV is shown in Figure 5.12. Examples of results from these measurements are shown in Figures 5.13 through

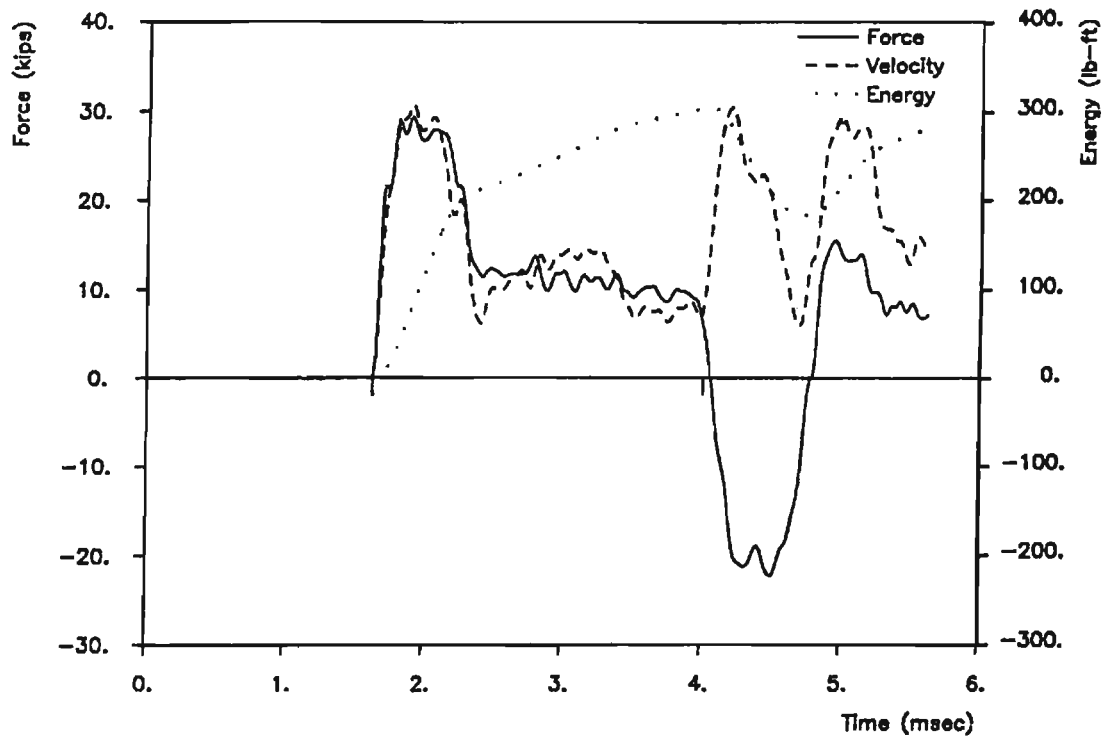


Figure 5.7: Force, Velocity and Energy Obtained from Top Transducers.

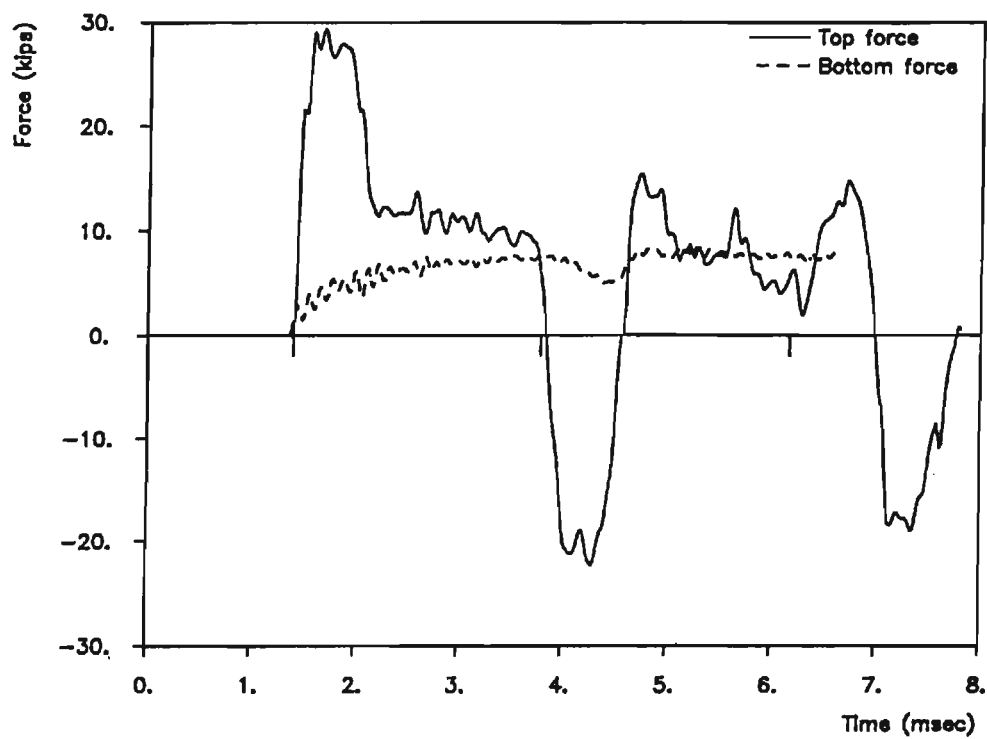


Figure 5.8: Superposed Force Records.

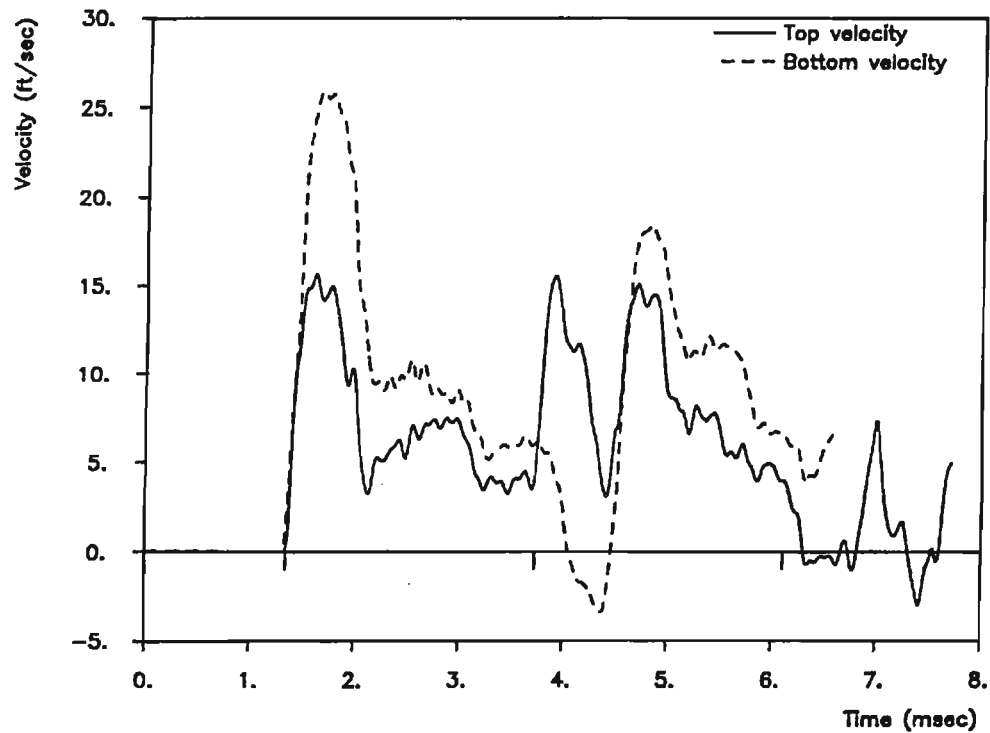


Figure 5.9: Superposed Velocity Records.

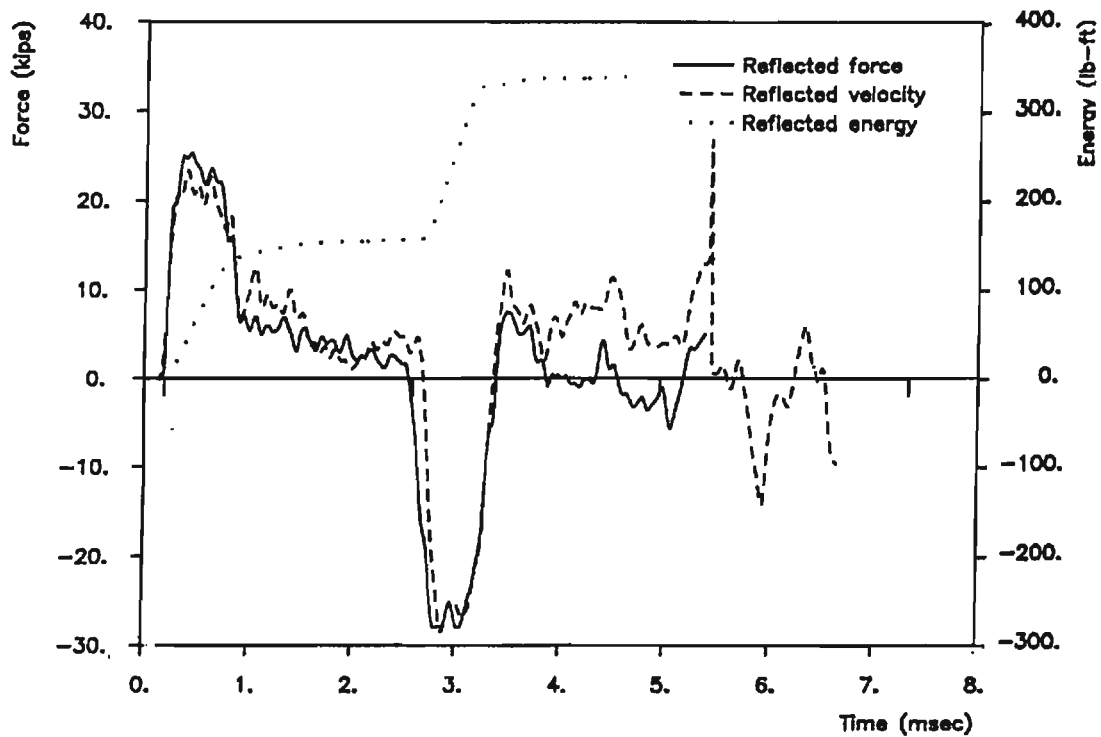


Figure 5.10: Force, Velocity and Energy Obtained from the Reflected Wave.

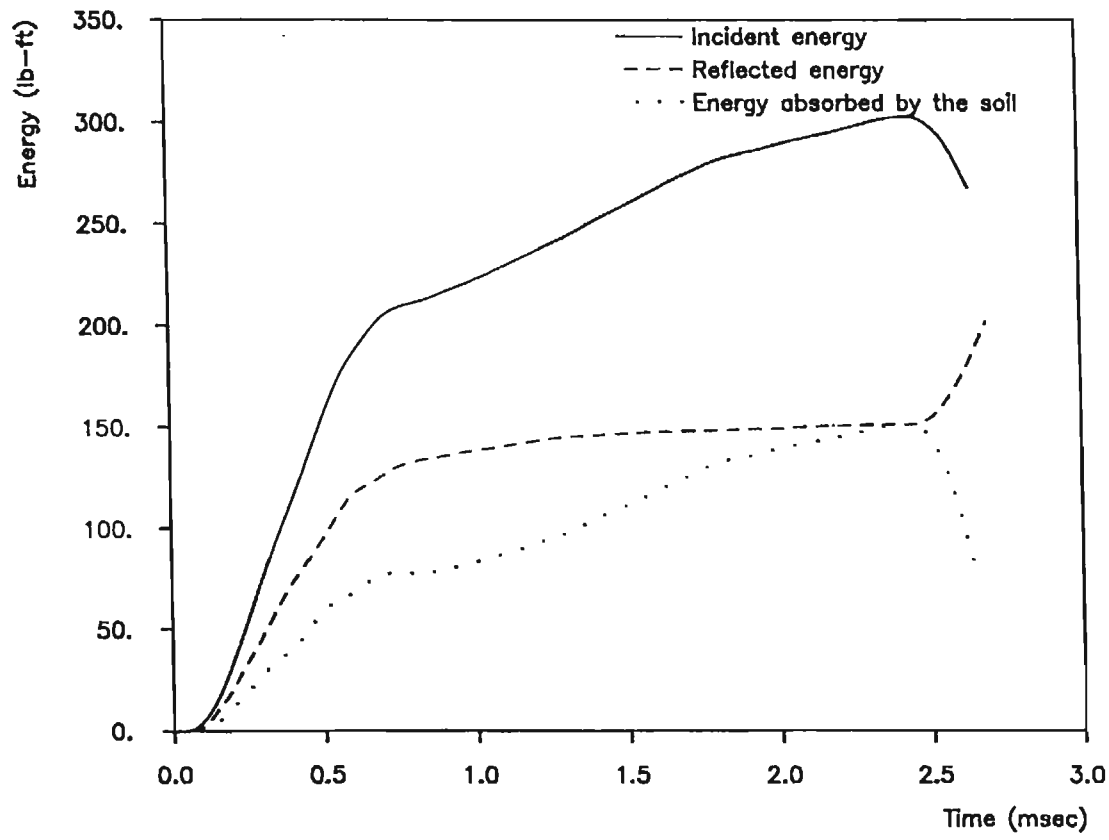


Figure 5.11: Calculation of the Energy absorbed by the Soil.

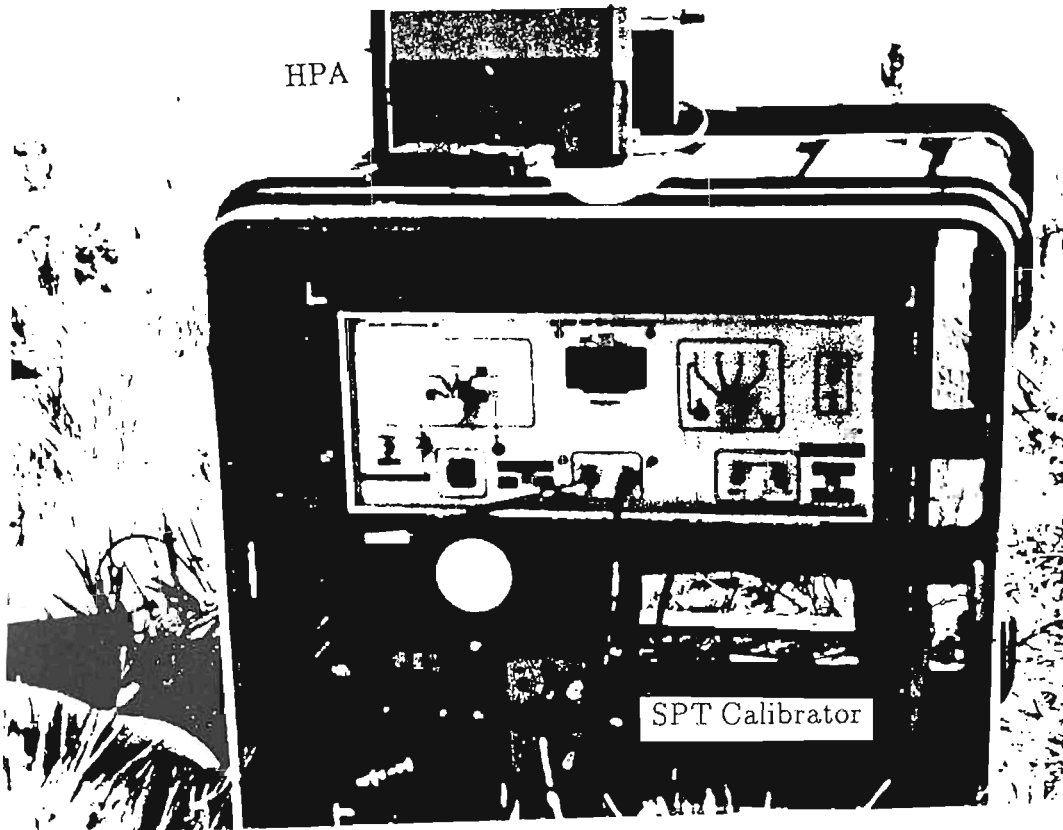
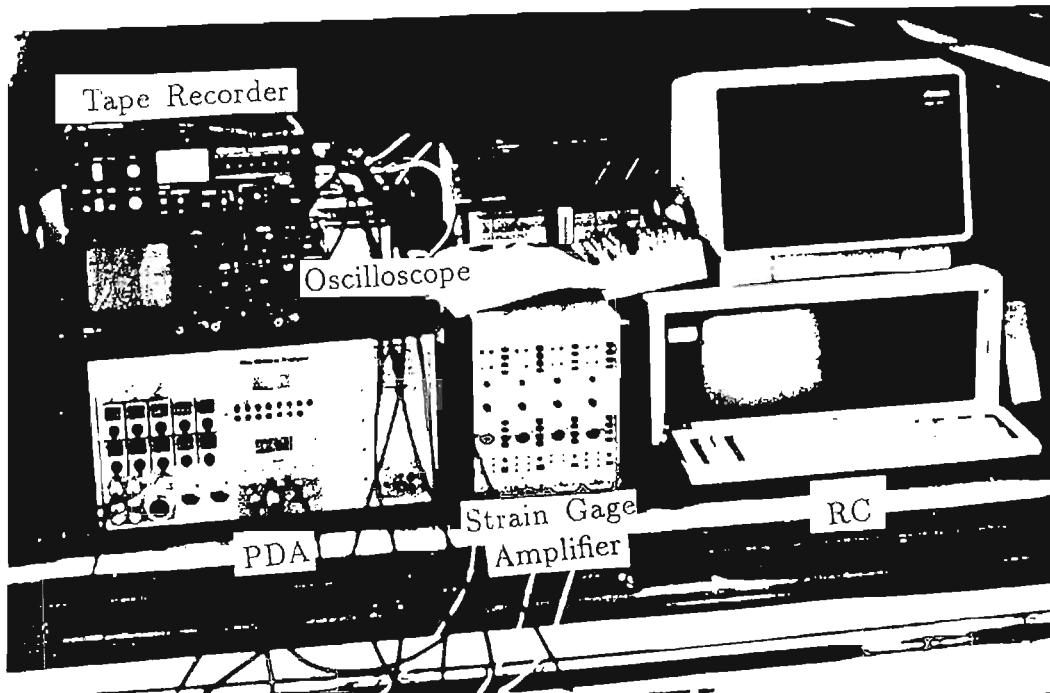


Figure 5.12: Picture of the Data Acquisition Systems Used in the Field Tests.

5.16. The first thing to notice here is the difference in the shape of the waves produced by each of the hammers in the field and the laboratory tests, and also the magnitude and length of the first peak. These differences are due to the difference in the geometric shapes of the hammers and impact block assemblies.

Figures 5.13 and 5.14 show a plot of the force, velocity and energy for two blows taken through the RC during the CME hammer test. The total length below gages for these blows was 77.5 feet, and the bottom was a soft rock. The SPT blow count (N-value) was ninety blows per foot. The effect of the sampler on the wave propagation can be easily noticed by looking at the behavior of the force and velocity at the  $2L/c$  time. The sampler has larger area than that of the drill rod and thus at the juncture between them a reflection and transmission takes place. Since an enlargement in the area is encountered, part of the incident compression wave will reflect back as compression, but the reflected velocity wave will have an opposite sign. These reflected waves propagate upwards for a  $2L_s/c$  time ( $L_s$  is the sampler length) before any reflection from the bottom arrives. This explanation can be seen in the two figures where, at  $2L/c$  time, the force increases sharply (indicates compression) while the velocity goes in the other direction. The length of these spikes is  $2L_s/c$ . Another thing to notice here is that the reflected wave is in compression and that is due to the hard material (soft rock) at the bottom. The impact velocity was recorded for every blow, and for the blows shown in Figures 5.13 and 5.14 was 12.2 and 12.1 ft/sec, respectively. Maximum energy calculated from Equation (2.2) (graph) and the energy obtained from the Binary Instruments measuring system are shown on each of the plots.

Figure 5.15 also shows the force, velocity and energy as a function of time for another blow taken through the RC during the CME performance tests. The length below gages was 47.5 feet, and the soil was sandy clay. The SPT blow count was four blows per foot. At the first peak, notice that the velocity is smaller than the force and then at about 5 milliseconds the

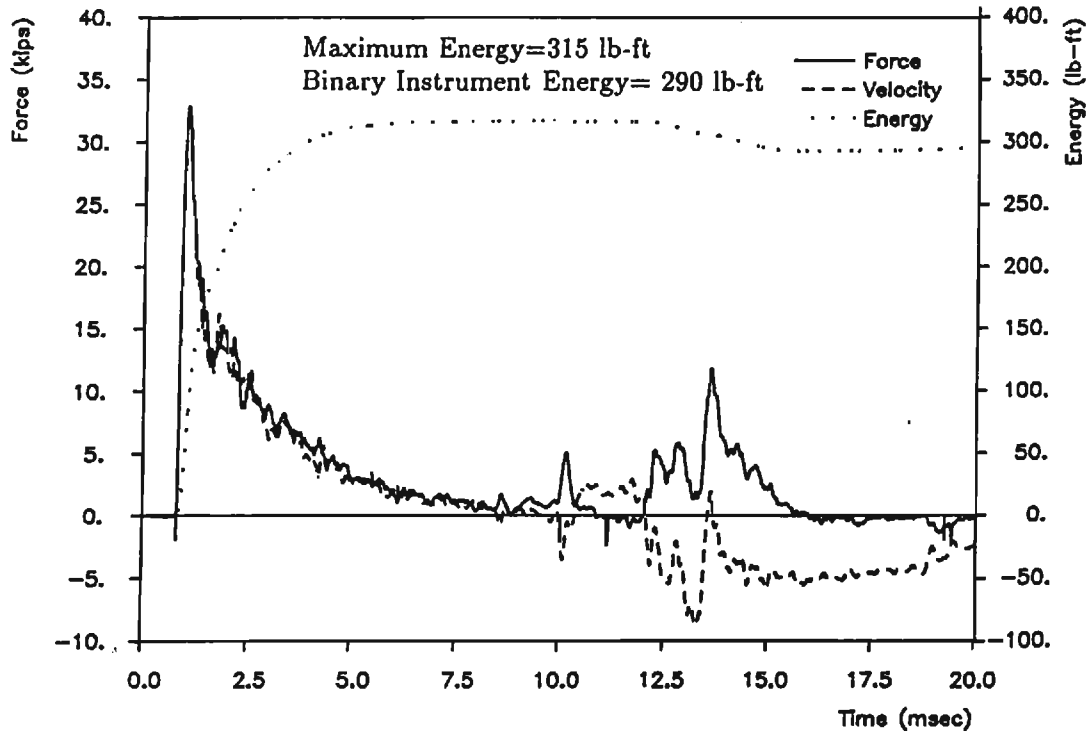


Figure 5.13: Field Test # 10, Blow No. 50, Length Below Gages is 77.5 ft, Taken Through the RC During the CME Automatic Hammer Performance, June 1990.

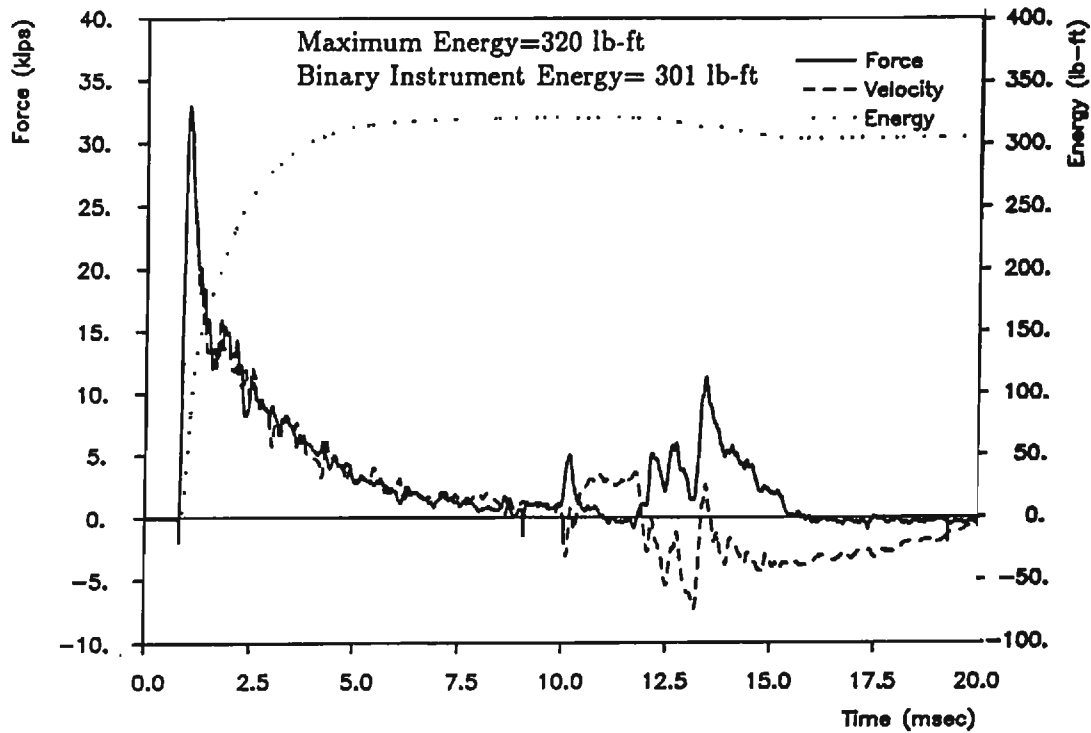


Figure 5.14: Field Test # 10, Blow No. 128, Length Below Gages is 77.5 ft, Taken Through the RC During the CME Automatic Hammer Performance, June 1990.

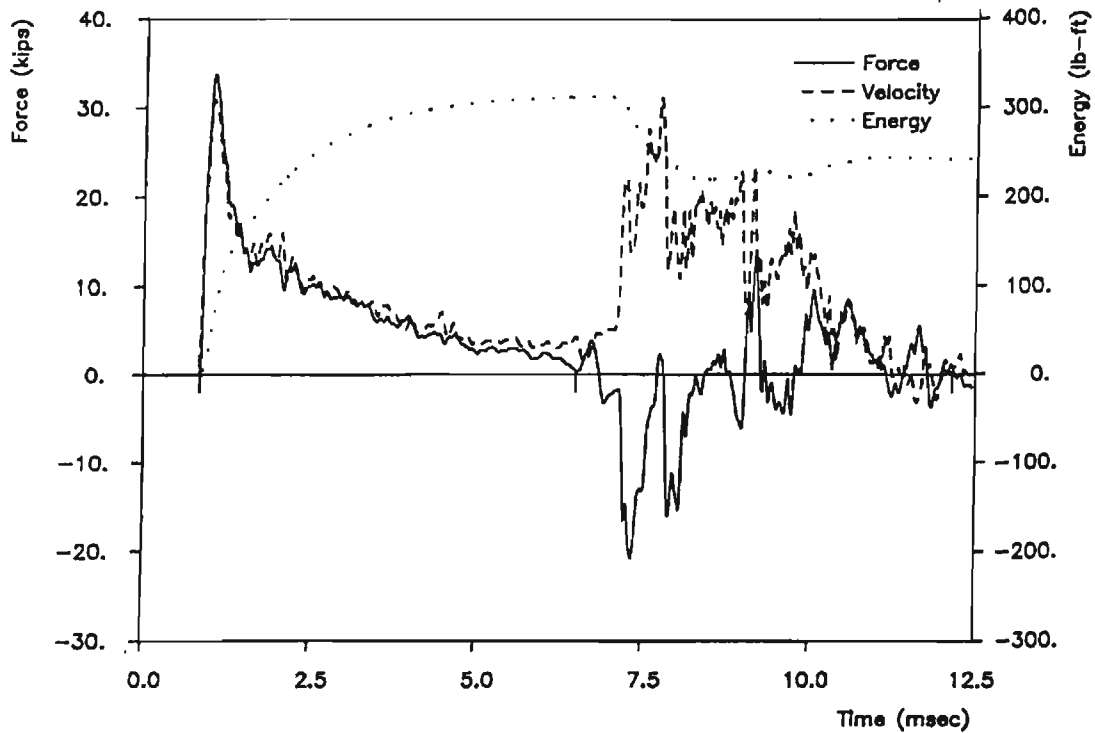


Figure 5.15: Field Test # 8, Blow No. 5, Length Below Gages is 47.5 ft, Taken Through the RC During the CME Automatic Hammer Performance, June 1990.

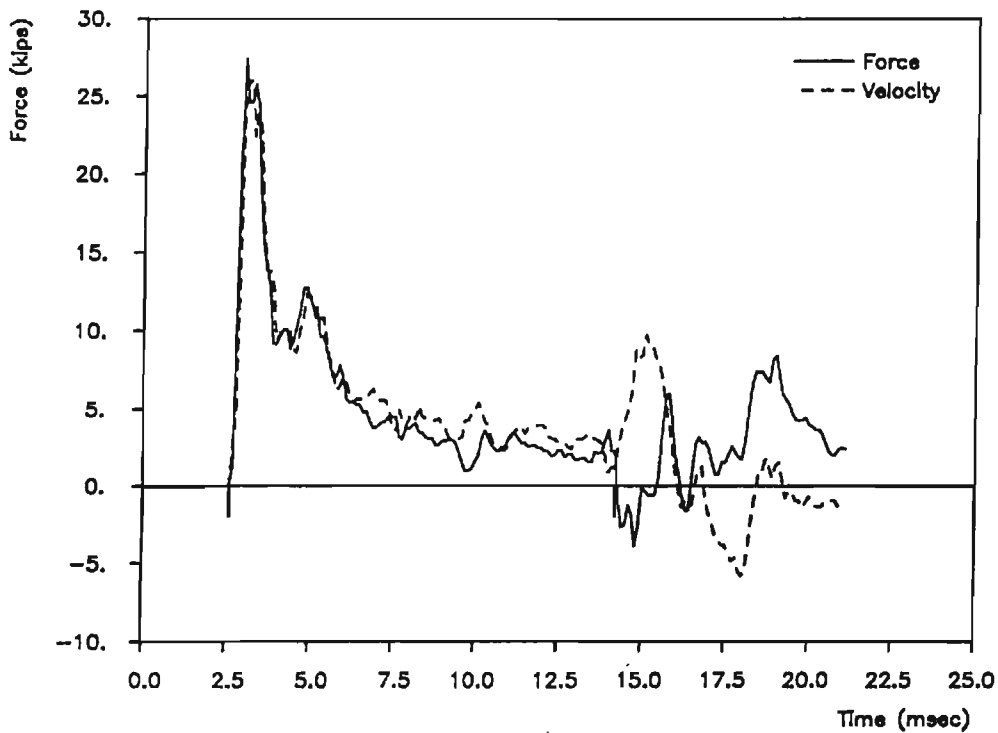


Figure 5.16: Field Test #8, Blow No. 9, Length Below Gages is 82.5 ft, Taken Through the PDA During the Pilcon Hammer Performance, August 1990.

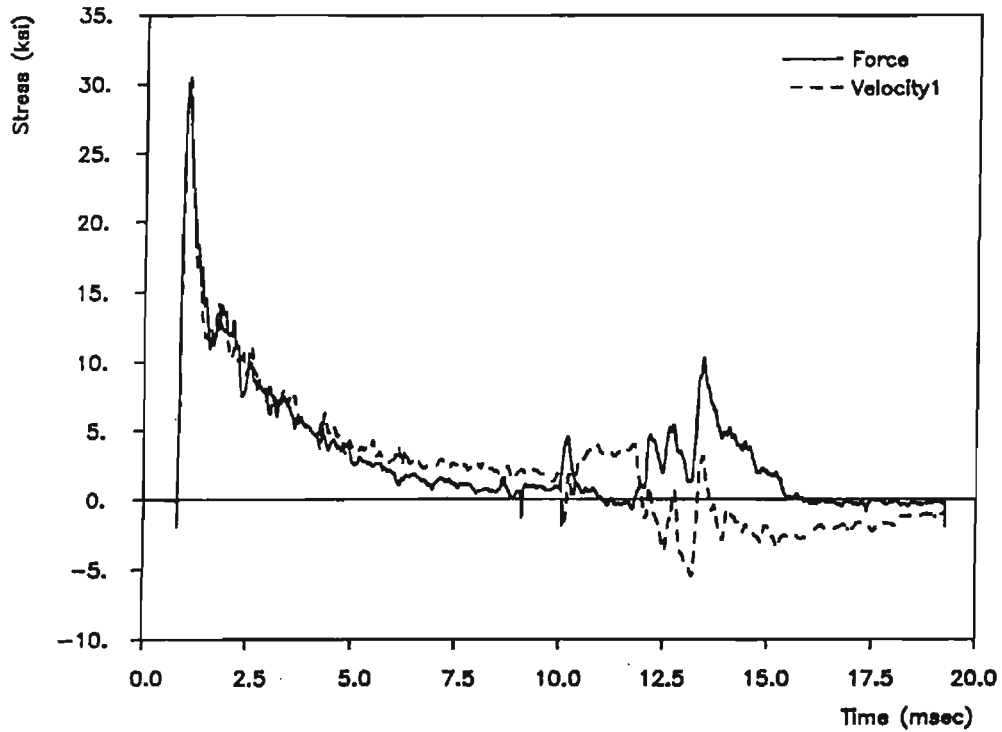
velocity goes above the force. This lack in proportionality is believed to be due to using one accelerometer only. That was because the connection of the lead wire to the plug of one of the accelerometers had been cut off. The effect of using one accelerometer is presented in Figure 5.17 where for the same blow shown in Figure 5.12 the velocities from each accelerometer were plotted separately along with the force. In both plots the proportionality is not as good as when both accelerometers were used.

In Figure 5.15, a different behavior of the force and the velocity can be observed, after the  $2L/c$  time, when driving in soft material. The reflected force wave is in tension while the velocity is reflected back with same sign as the incident one.

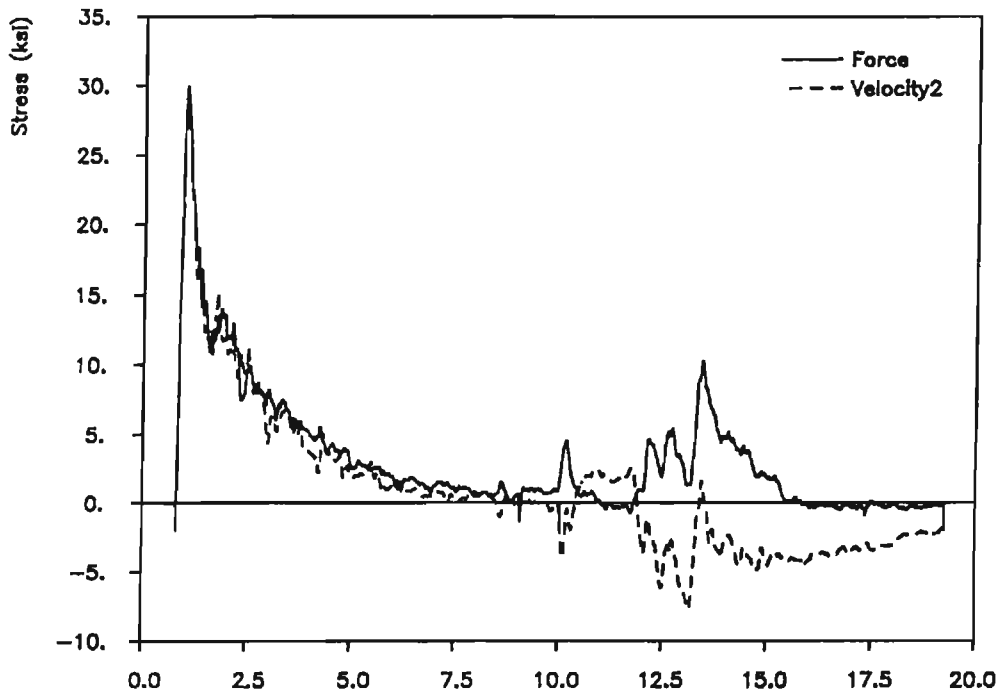
Figure 5.16 shows a plot of a record taken, at a different site, through the PDA during the Pilcon hammer performance test. The length below gages was 82.5 feet, and the soil consisted of soft rock. The N-value was one hundred twenty blows per foot. At about 9.5 milliseconds a sharp drop in the force and a rise in the velocity was appeared. This was found to be due to a loose connection at that depth. This loose connection delayed the wave propagation by 1.78 milliseconds and made the  $2L/c$  time 11.6 milliseconds instead of 9.82 milliseconds.

### 5.2.1 Stress Peak Evaluation

As can be seen from the previous results, the value of the stresses generated in the rod from a hammer blow is dependent on the hammer's geometric shape. The shape and the magnitude of a stress wave generated in the rod by the safety hammer was discussed in Chapter III. The maximum stress peak was  $1.06\sigma_i$ , where  $\sigma_i$  is the stress obtained from multiplying the impact velocity by  $E/c$  of the rod. This value is 6% higher than that if the hammer were a rigid mass and struck on the drill rod itself. If the anvil was removed and the hammer was dropped directly on the drill rod, the maximum stress would be  $0.8\sigma_i$ . The maximum stress value



Plot of the Same Record Shown in Figure 5.13, But Using One of the Two Accelerometers to Calculate the Velocity.



Plot of the Same Record Shown in Figure 5.13 Using the Second Accelerometer

Figure 5.17: Effect of Using One Accelerometer Instead of Two.

obtained while using the pilcon hammer was the same as that of the safety hammer, (see Figure 5.16) but different stresses were obtained during the CME hammer performance. This phenomena gave a reason for looking at the wave propagation when the CME hammer is used.

The CME automatic hammer is a single acting hammer which consists of a 140 lb ram that impacts on the top of an anvil connected to the drill rod. The dimensions of the ram and the anvil are shown in a drawing of the system in Figure 5.18. The ram and the anvil are of same material which means that their impedance ratio equals the ratio between their areas which in this case is 0.25. Just before impact the ram is moving as a rigid body with a velocity equal to the impact velocity,  $v$ . At impact, a part of this velocity is transferred to the anvil and a stress wave is generated, propagating downwards in the anvil and upwards in the ram. From Equation 3.6, the velocity transferred to the anvil is  $0.8v$  and the one reflected to the ram is  $0.2v$ . The same values would represent the stresses. The wave propagation in the system is shown in Figure 5.19. At the juncture between the anvil and the drill rod, transmission and reflection take place. The anvil and the drill rod are also of the same material and thus, the impedance ratio is equal to their area ratio which is 0.224. From Equation 3.2 the transmitted velocity is  $1.307v$  and the stress is  $1.307v$ . Therefore, this value is 30.7% larger than that if the drill rod was struck by a rigid mass. The reflected wave is in tension and moves up the anvil until it is reflected on top. The hammer is still in contact with the rod, a transmission and reflection takes place, and a reflected tension wave moves down the anvil and repeats the cycle of reflections and transmissions as described earlier. At the same time, the wave traveling up in the hammer would reflect at the free end and propagate down until another impact is felt by the anvil and repeats the cycle.

If the anvil were removed and the ram were dropped directly on the drill rod, the stresses generated from such a blow would be smaller than that if the anvil were used. The impedance

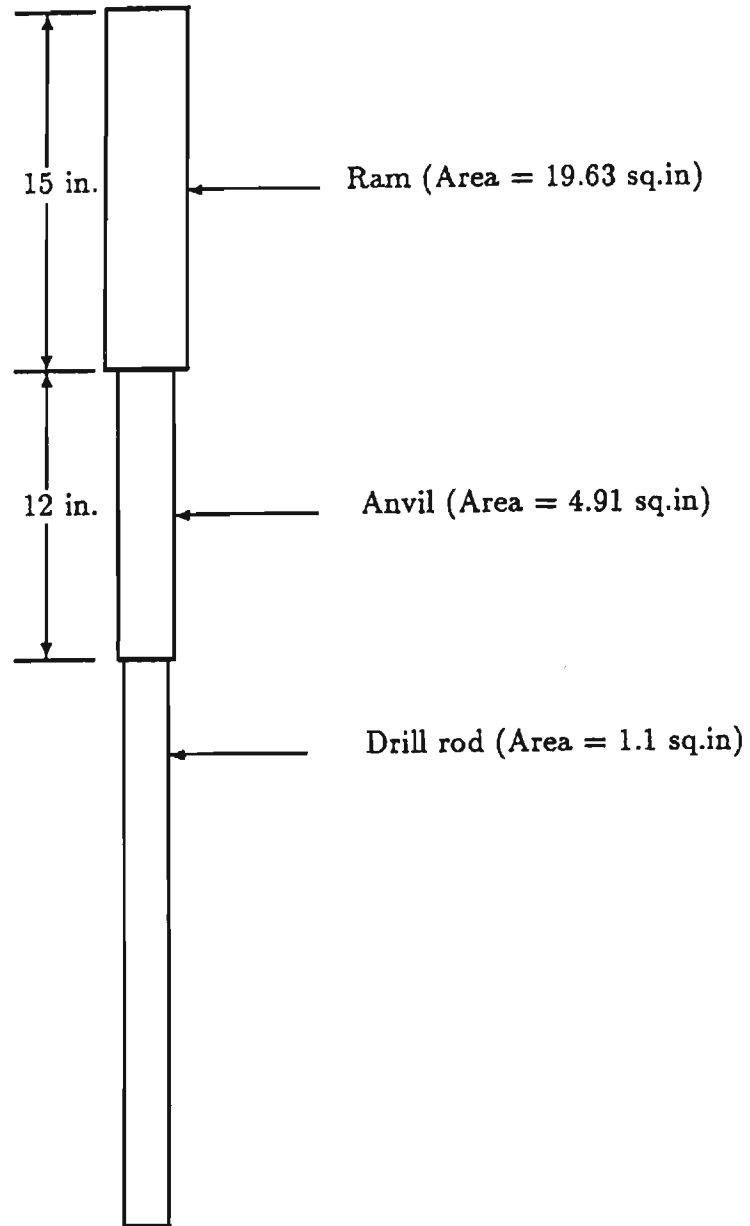


Figure 5.18: Dimensions of the CME Automatic Hammer System.

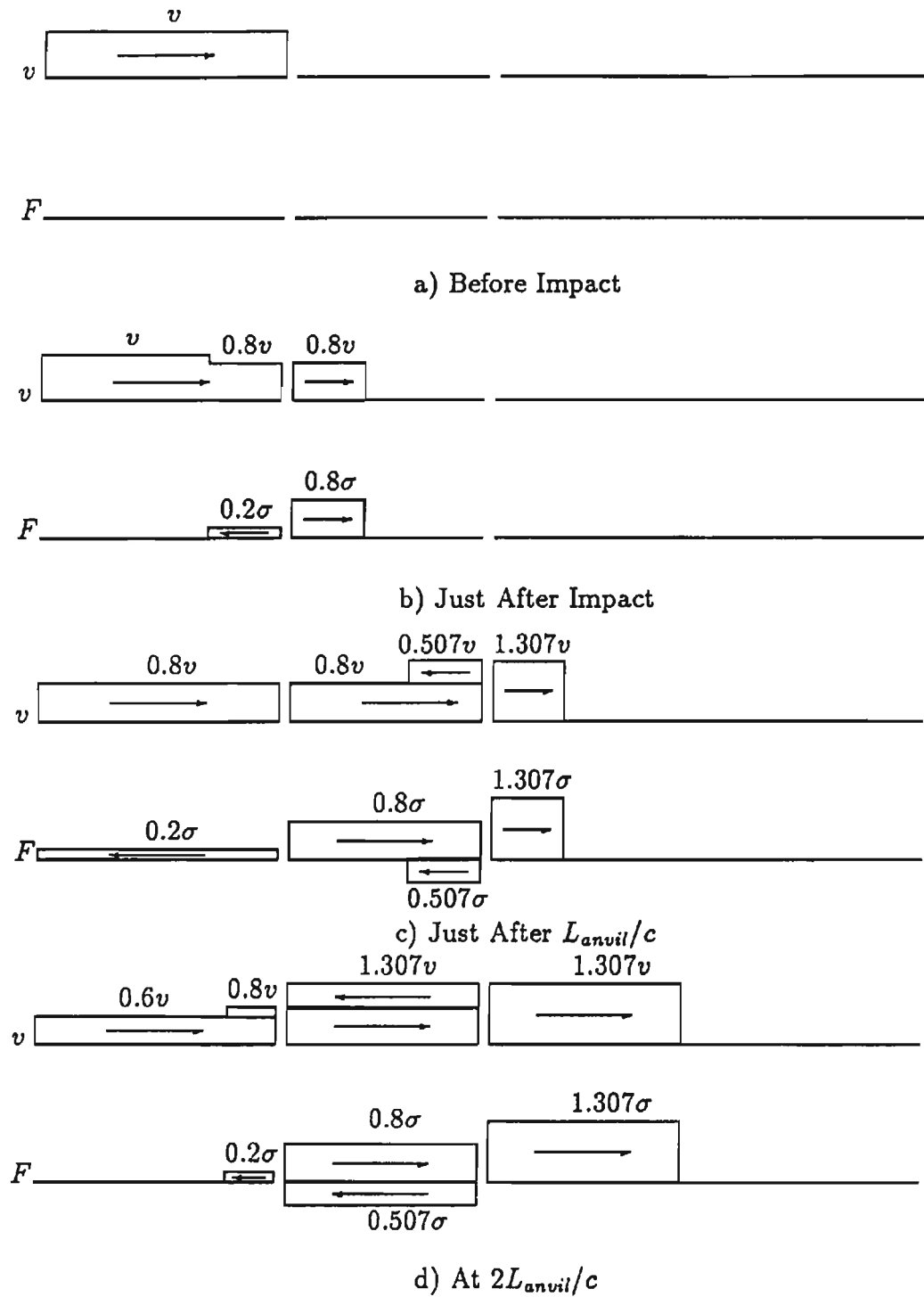


Figure 5.19: Wave Propagation in the CME Hammer System.

ratio between the hammer and the drill rod is the ratio between their areas which is 0.056. By substituting for this value in Equation 3.6, the stresses in the rod would be  $0.947\sigma_i$ .

It is of interest to note that the stress value of  $1.307\sigma_i$  is about 30 ksi for the velocities measured with the radar. This compares very well with the peak stress shown in Figure 5.17.

### 5.2.2 Bottom Analysis

As mentioned in Section 2.6, one can, from top measurements, calculate bottom quantities such as resistance, velocity and displacement as a function of time. These quantities give a better understanding of the soil behavior under a hammer blow. To demonstrate this, bottom analysis was made for two blows taken in different soil conditions. The first blow is the one shown in Figure 5.14 where the bottom consists of soft rock and the second was shown in Figure 5.15 where the soil was a soft, sandy clay. Figures 5.20 and 5.21 show the soil resistance calculated for each of the blows. In the sandy clay material where the blow count was very low, the soil resistance vanishes very rapidly and the sampler moves very easily, this movement is represented by the velocity and the displacement in Figure 5.22. The final displacement is 2.8 inches and that gives a blow count of four blows per foot which agrees with the N-value counted in the field. Different behavior is observed in the soft rock strata. The velocity vanishes quickly and gives small displacement (Fig. 5.22) while the bottom resistance is large. The displacement here is 0.2 inches which gives a blow count of 60 blows per foot whereas the blow count from the field was 90 blows per foot. Also, plots of the bottom reaction versus displacement gives a better explanation of the event and those are shown in Figures 5.24 and 5.25.

The other important thing that can be calculated from these bottom quantities is the energy delivered to the soil and this is obtained from the multiplication of the reaction by the displacement. Figure 5.26 shows the delivered energy as a function of time for the record shown

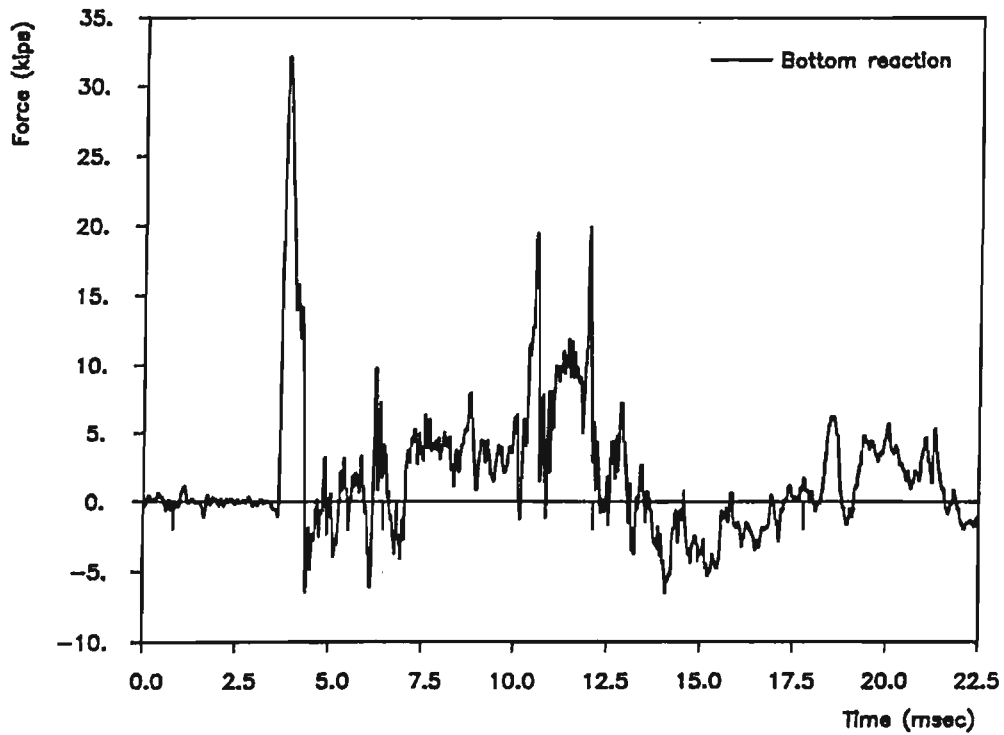


Figure 5.20: Bottom Resistance for the Blow Taken in the Sandy Clay Soil.

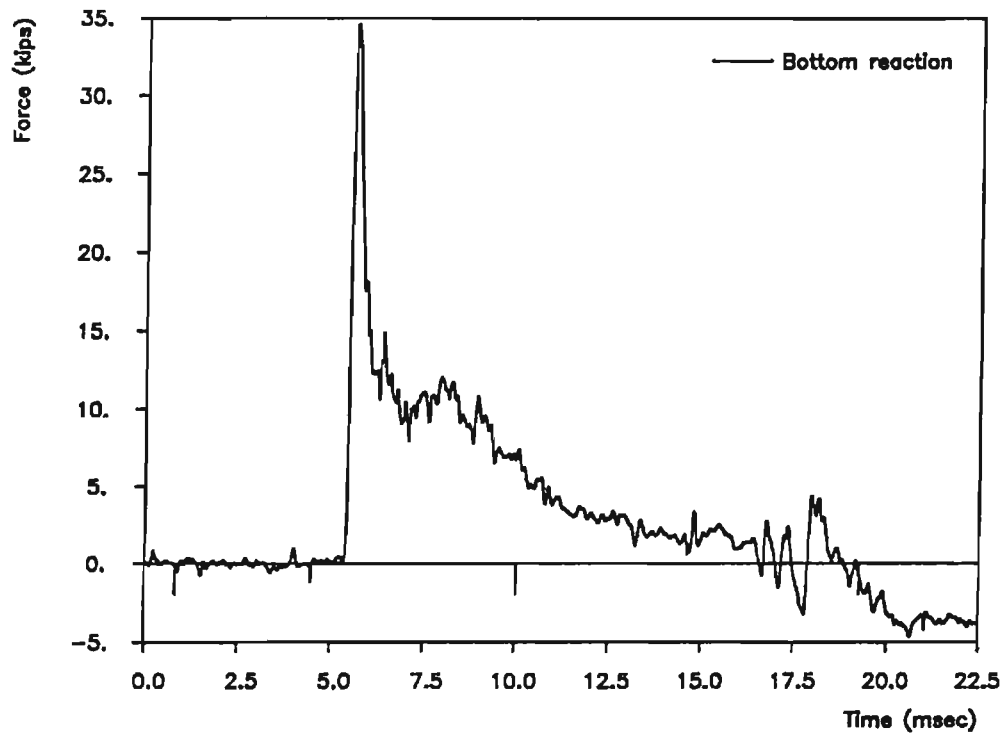


Figure 5.21: Bottom Resistance for the Blow Taken in the Soft Rock Strata.

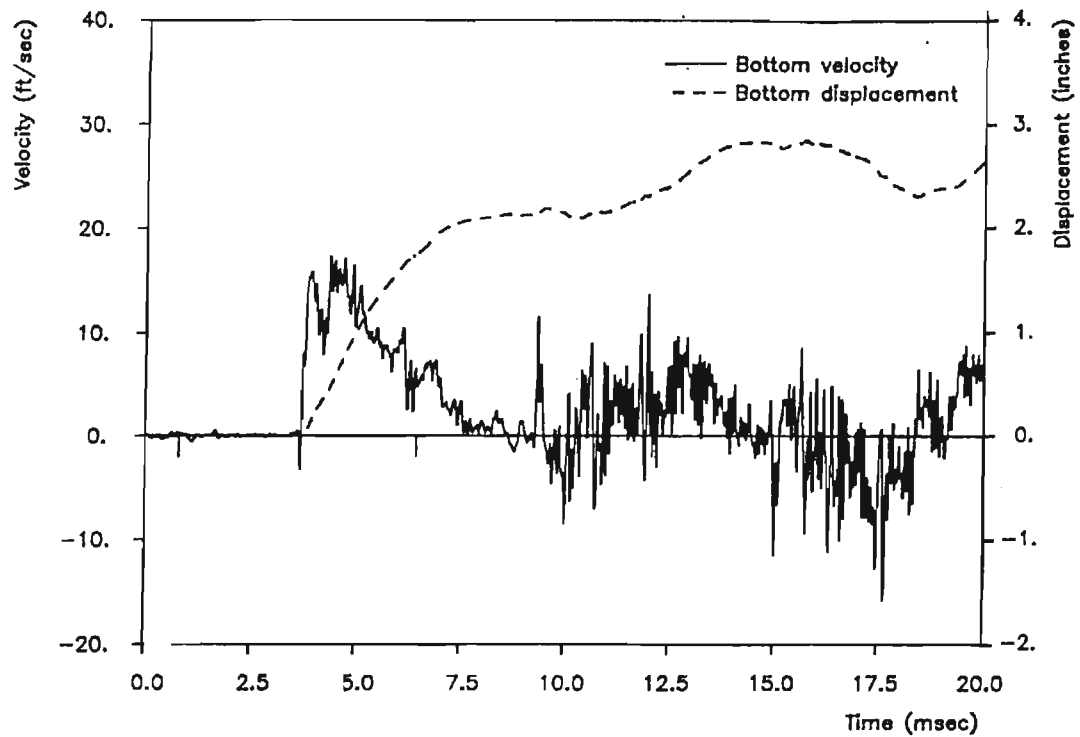


Figure 5.22: Bottom Velocity and Displacement of the Blow in the Sandy Clay.

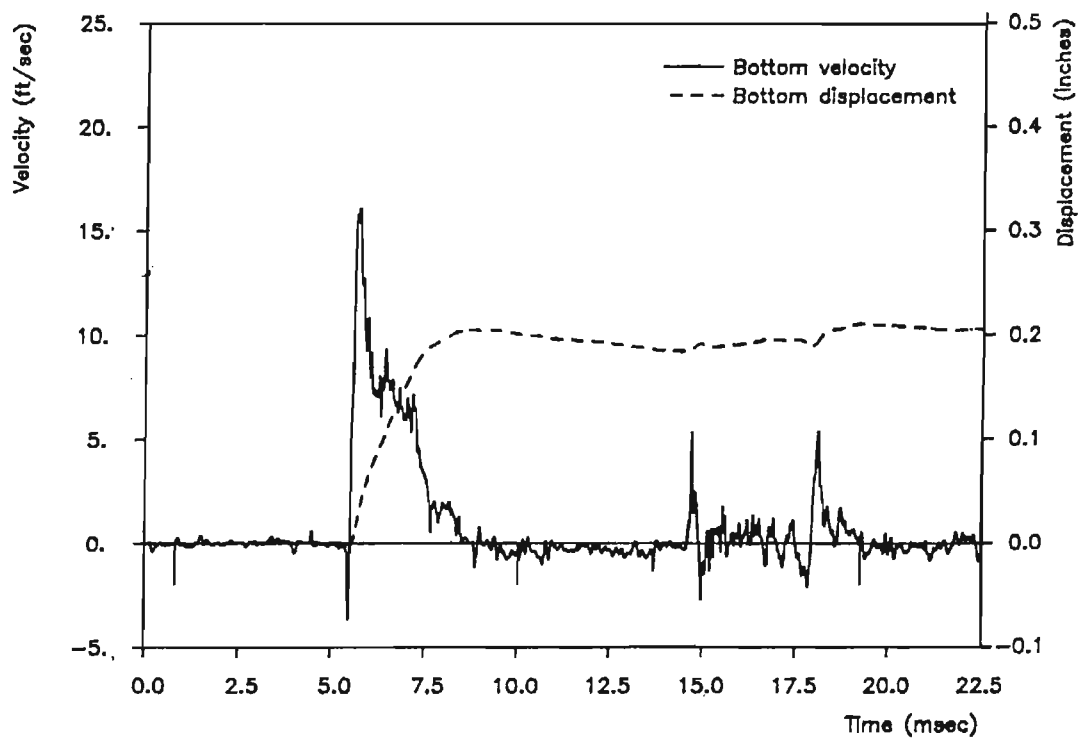


Figure 5.23: Bottom Velocity and Displacement for the Blow in the Soft Rock.

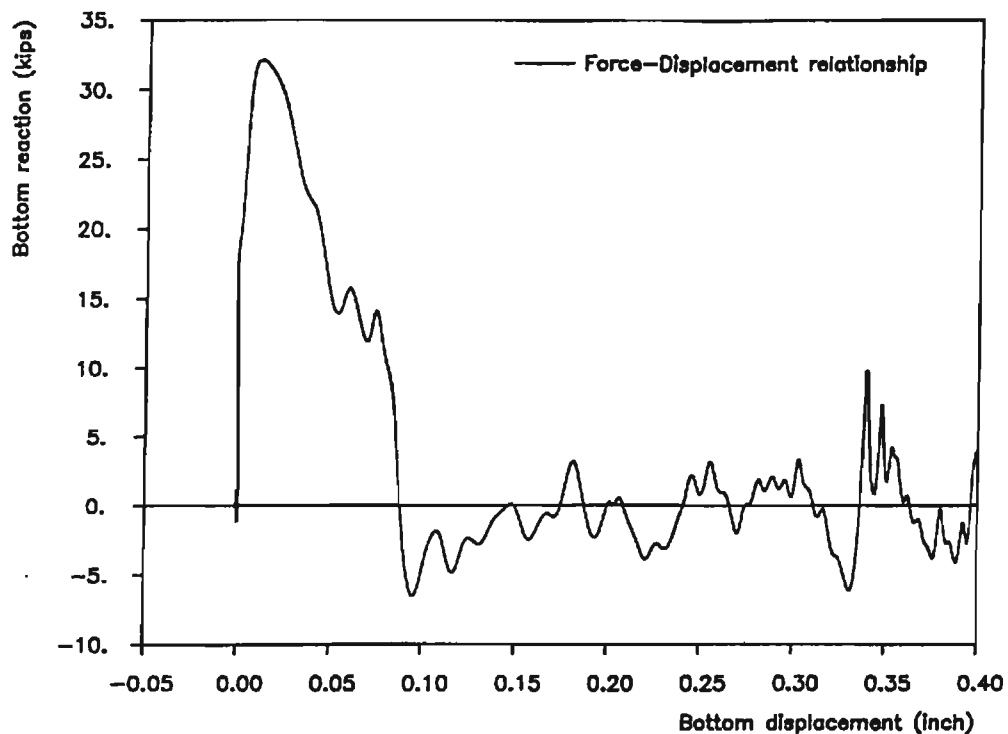


Figure 5.24: Bottom Reaction Versus Displacement for the Record Taken in the Sandy Clay Soil.

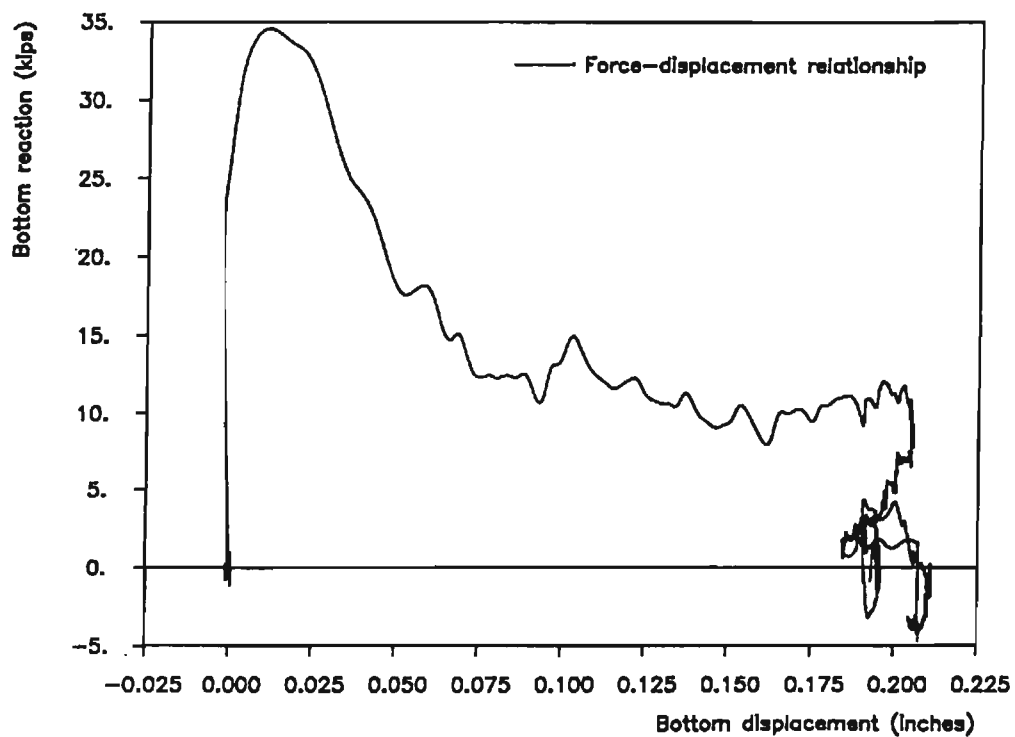


Figure 5.25: Bottom Reaction Versus Displacement of the Record Taken in the Soft Rock.

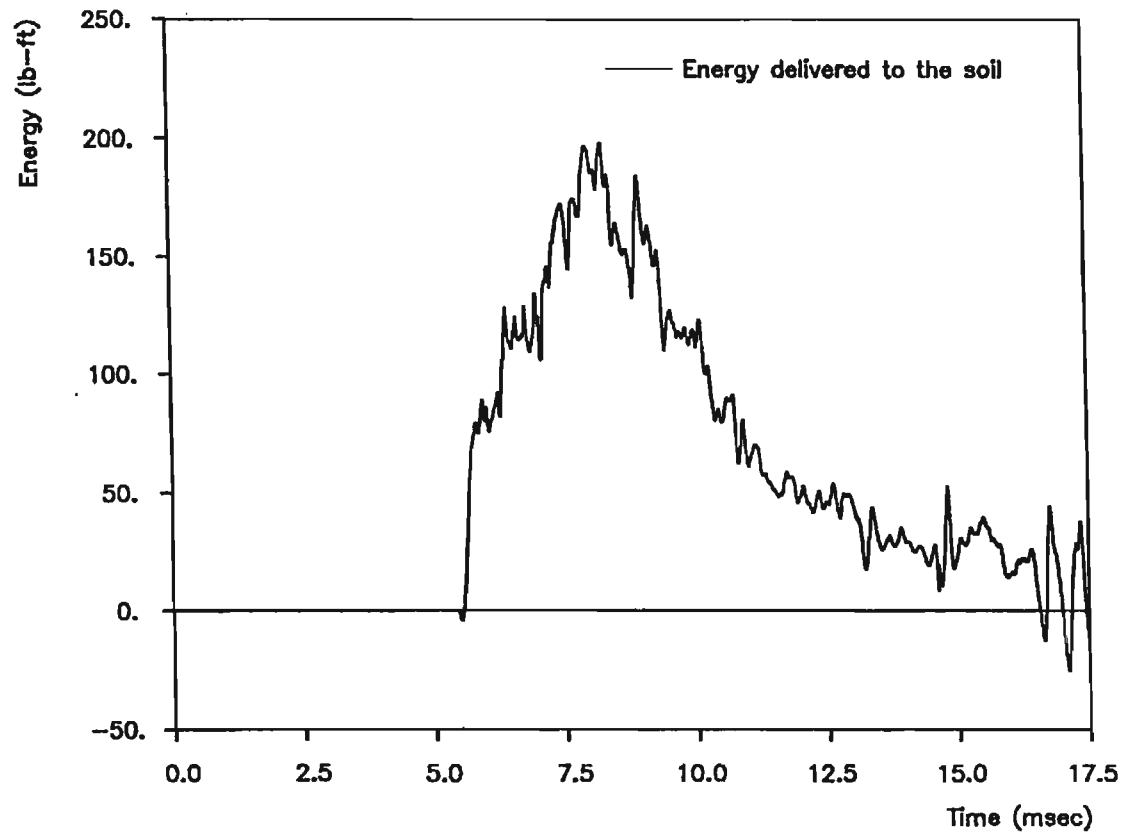


Figure 5.26: Energy Delivered to the Soil for the Record Taken in the Soft Rock.

energy delivered to the soil and this is obtained from the multiplication of the reaction by the displacement. Figure 5.26 shows the delivered energy as a function of time for the record shown in Figure 5.14. The maximum energy is about 175 lb-ft which is 55% of the energy transferred to the drill rods and 50% of the theoretical  $E_n$ .

This analysis describes the sampler behavior under a hammer blow in two different soil conditions and also provides a force-displacement relationship from which soil properties can be obtained. No attempt has been made to study the engineering properties of the soil or its correlation to the SPT blow count.

## CHAPTER VI

### CONCLUSIONS AND DISCUSSION

The experiments and testing described here have given a better insight to the measurement of the dynamics of the SPT. With the successful measurements of force and acceleration at the top, the door is opened for further analysis which may lead to a more accurate interpretation of the SPT in general, and also this might yield valuable information for pile driving analysis and capacity.

The main problem that has, in the past, faced the dynamic measurements on the SPT is the frequency response of the measuring system. In this project, the frequency response of the measuring system has been shown to be satisfactory. Both signals, the force and the acceleration, were filtered to have a frequency contents not more than 10 KHz. The accelerometers response for these frequency contents was found to be adequate and the sampling frequency of the data acquisition system is high enough to satisfy the needs. The calibration factor of the force measuring device obtained from static tests and that of the accelerometers provided by Entran were found to be incorrect and thus the system was recalibrated under dynamic load using the pendulum test. This test also gave a better understanding of the response of the measuring system.

From studying of the wave propagation in different systems used in the SPT procedure, it was found that the stresses generated in the rod from a hammer blow depends on the system that is used in this procedure. Stresses generated by using the safety hammer were lower than

that generated by the CME automatic hammer, but the difference in the systems seems to have no effect on the energy delivered to the rod. Also, changes in the system itself were shown to have an effect on the stress level in the rod. Removing the drive rod from the safety hammer system or the anvil from the CME system decreased the stresses in the rod, but no further study has been made to find if this fact has any effect on the blow count.

Analysis and calculations of bottom quantities from top measurements for laboratory and field tests are presented in Chapter V. This analysis is a demonstration for what one can obtain from the top force and acceleration measurements and it can be the key for further studies on the SPT of this aspect.

## References

- Casagrande, A. and Casagrande, L. (1968). "Foundation Investigations for the Donald E. Cook Nuclear Power Plant." Report to the American Electric Power Service Corporation, Amendment 5, Appendix G, Cambridge, MA.
- Chen, C., (1990). "Energy Transfer in the Standard Penetration Test," Thesis presented to University of Colorado at Boulder in partial fulfillment for Master of Science.
- Clough, R.G. and Penzien, J. (1975). *Dynamic of Structures*. McGraw Hill Book Co., New York, NY.
- De Mello, V. (1971). "The Standard Penetration Test: A-state-of-the-Art Report." *Fourth Pan American Conference on Soil Mechanics and Foundation Engineering*, International Society of Soil Mechanics and Foundation Engineering, I, Puerto Rico, 1-86.
- Fairhurst, C. (1961). "Wave Mechanics of Percussive Drilling," *Mine and Quarry Engineering*, March, 122-130, April, 167-178, July, 327-328.
- Fischer, H.C. (1984). "Stress Wave Theory For Pile Driving Applications," *Proceedings of the Second International Conference on the Application of Stress-Wave Theory on Piles*, Ottawa, Canada.
- Fletcher, G.F.A. (1975). "Standard Penetration Test: Its Uses and Abuses," *Journal of the Soil Mechanics and Foundation Division*, ASCE, 91(SM4), 67-75.
- Gibbs, H.J. and Holtz, W.G. (1957). "Research on Determining the Density of sands by spoon penetration testing," *Proceedings Fourth International Conference on Soil Mechanics and Foundation Engineering*, London, UK, I, 35-39.
- Goble, G.G., Likins, G.E. and Rausche, F. (1975). "Bearing Capacity of Piles from Dynamic Measurements," Final Report to the Ohio Department of Transportation, Case Western Reserve University.
- Goble, G.G. and Ruchti P. (1981) "Measurements of Impact Velocity on Penetration Testing Systems," Report to the Central Mine Equipment Company, University of Colorado, Boulder.
- Goble, G.G. (1988). "Wave Mechanics," Presented at the seminar on Testing Cast-in-Situ Piles for Capacity and Integrity, University of Colorado, Boulder.
- Hauge, K. (1979) "Evaluation of Dynamic Measurement System on the Standard Penetration Test," Report to the Central Mine Equipment Company, University of Colorado, Boulder.
- Kovacs, W.D., Griffith, A.H. and Evans, J.C. (1975). "A Comparative Investigation of the Mobile Drilling Company's Safe-T-Driver with the Standard Cathead with Manilla Rope for Performance of the Standard Penetration Test," Report from the School of Civil Engineering, Purdue University.
- Kovacs, W.D., Griffith, A.H. and Evans, J.C. (1978). "An Alternative to The Cathead and Rope for the Standard Penetration Test," *Geotechnical Testing Journal*, ASTM, I (2), 72-81.

- Marcuson, W.D. and Bieganovsky, W.A. (1977). "Laboratory Standard Penetration Tests on Fine Sand," *Journal of the Geotechnical Engineering Division*, ASCE, 103(GT6), 565-588.
- Meyerhof, G.G. (1976). "Bearing Capacity and Settlement of Pile Foundation," *Journal of the Geotechnical Engineering Division*, ASCE, 102(GT3), 195-228.
- Oran, B.E. (1988). *The Fast Fourier Transform And Its Applications*, Avanteck, Inc., New Jersey.
- Rausche, F. (1988). "A Short Introduction to Continuous and Discrete Wave Mechanics," Presented at the seminar on Testing Cast-In-Situ Piles for Capacity and Integrity, University of Colorado, Boulder.
- Schmertmann, J.H. (1977). "Use the SPT to Measure Dynamic Soil Properties? - Yes, but...!", Symposium on Dynamic Field and Laboratory Testing of Soil and Rock, ASTM, Denver Colorado.
- Schmertmann, J.H., Smith, T.V. and Ho, R. (1978). "Example of an Energy Calibration Report on a Standard Penetration Test (ASTM, 1,(1)1, 57-61.
- Schmertmann, J.H. and Palacios, A. (1979). "Energy Dynamics of SPT," *Journal of the Geotechnical Engineering Division*, ASCE, 105(GT8).
- Teferra, W. (1977). "Dynamic Study of Steel Piles with High Driving Stresses," Thesis presented to Case Western Reserve University in partial fulfillment for the degree of Master of Science.
- Seed, H.B., Mori, K. and Chan, C.K. (1977). "Influence of Seismic History on Liquefaction of Sands," *Journal of the Geotechnical Engineering Division*, ASCE, 103(GT4), 257-270.
- Terzaghi, K. and Peck, R.B. (1967). *Soil Mechanics in Engineering Practice*, John Wiley and Sons, Inc., New York.

## APPENDIX A

### ONE DIMENSIONAL STRESS WAVE MECHANICS

#### IN A ROD UNDER IMPACT

##### A.1 Derivation of the Wave Equation

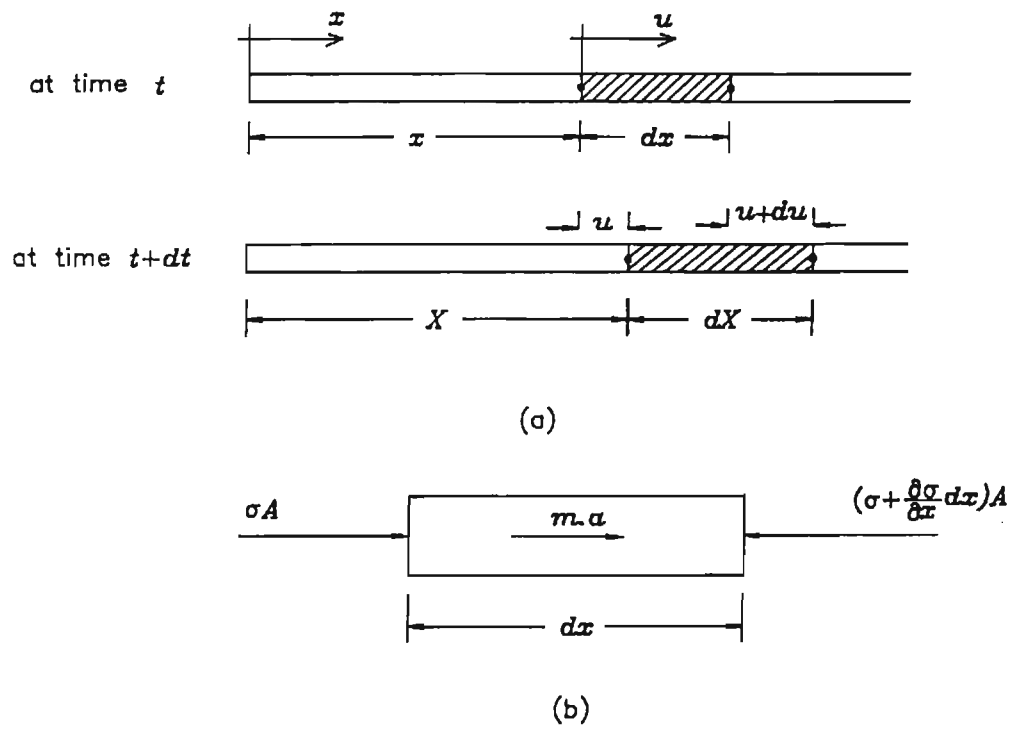
In order to study the characteristics of the stress wave, the displacement due to the strain associated with the passage of the stress wave will be considered. Let the displacement of a particle in a uniform, elastic rod at distance  $x$  from a fixed coordinate origin at time  $t$  to be  $u(x,t)$ . After a time  $dt$  the point at the distance  $x$  will move a distance  $u$  to a new position  $X$  and the neighboring point at  $x+dx$  will displace by  $u+du$  to a position of distance  $X+dX$  (Fig. A.1a). The change in length of the portion  $dx$  is :

$$dX - dx = du = \frac{\partial u}{\partial x} dx$$

and therefore,

$$\epsilon = \frac{dX - dx}{dx} = \frac{\partial u}{\partial x}$$

Now, considering the free body shown in Fig. A.1b and using Newton's second law ( $F = ma$ ) the following relation can be obtained:



$$F = m \cdot a \quad m = A \cdot \rho \cdot dx \quad a = \frac{\partial^2 u}{\partial t^2}$$

$$\left(\sigma + \frac{\partial \sigma}{\partial x} dx\right) A - \sigma A = m \cdot a = (A \cdot \rho \cdot dx) \frac{\partial^2 u}{\partial t^2}$$

$$\frac{\partial \sigma}{\partial x} = \rho \frac{\partial^2 u}{\partial t^2}$$

Figure A.1: Derivation of Wave Equation.

$$\frac{\partial \sigma}{\partial x} = \rho \frac{\partial^2 u}{\partial t^2} \quad (\text{A.1})$$

But,

$$\sigma = E \cdot \varepsilon \quad \text{and} \quad \varepsilon = \frac{\partial u}{\partial x}$$

Therefore,

$$\sigma = E \frac{\partial u}{\partial x} \quad \text{or} \quad \frac{\partial \sigma}{\partial x} = E \frac{\partial^2 u}{\partial x^2} \quad (\text{A.2})$$

Substitute (A.2) into (A.1), and the governing differential equation, the so-called wave equation, is obtained

$$\frac{\partial^2 u}{\partial t^2} = c^2 \frac{\partial^2 u}{\partial x^2} \quad (\text{A.3})$$

Where  $c^2 = E/\rho$ .  $E$  and  $\rho$  are Young's modulus and mass density of the rod, respectively. The general solution of Equation (A.3) is

$$u(x,t) = f(x + ct) + g(x - ct) \quad (\text{A.4})$$

which is easily checked by back substitution. The solution  $u(x,t) = f(x+ct)$  represents a wave traveling in the negative  $x$ -direction and  $u(x,t) = g(x-ct)$  represents a wave traveling in the positive  $x$ -direction.

## A.2 Wave Propagation

The displacement of a point at distance  $x$ , at time  $t$ , is given by

$$u(x_1, t_1) = f(x_1 + ct_1) + g(x_1 - ct_1)$$

After a time  $t = t_1 + \Delta t$  the wave propagating in the positive x-direction travels a distance  $\Delta x$  while the wave propagating in the negative direction travels a distance  $-\Delta x$  and therefore

$$u(x,t) = f(x_1 - \Delta x + c[t_1 + \Delta t]) + g(x_1 + \Delta x - c[t_1 + \Delta t]) \quad (\text{A.5})$$

Now, if  $c$  is defined as the speed of the wave propagation, then  $\Delta x$  equals  $c\Delta t$ . Substitute for  $\Delta x = c\Delta t$  in Equation (A.5) and simplify

$$u(x,t) = f(x_1 + ct_1) + g(x_1 - ct_1)$$

or,

$$u(x,t) = u(x_1, t_1)$$

This shows that after time  $\Delta t$  the stress wave, which is represented by the displacement, propagates a distance  $\Delta x = c\Delta t$  with a velocity  $c$  keeping its shape and magnitude. Notice that the earlier definition of  $c$  shows that it only depends on the material properties of the rod.

### A.3 Relation between Force and Velocity

Differentiating Equation (A.4) with respect to time leads to an expression for the velocity  $v(x,t)$  of a particle

$$v(x,t) = \frac{\partial}{\partial t} u(x,t) = c \left( \frac{\partial f(\eta)}{\partial \eta} - \frac{\partial g(\mu)}{\partial \mu} \right) \quad (\text{A.6})$$

where  $\eta = x + ct$  and  $\mu = x - ct$ . The above equation can be written as

$$v(x,t) = v_f(x + ct) + v_g(x - ct)$$

thus,  $v$  can also be described by two waves,  $v_f$  and  $v_g$ , which travel in opposite directions.

Now, suppose that the shape of the function  $f$  and  $g$  and, therefore,  $u(x,t)$  is known at a certain time  $t$ . Then the strain  $\epsilon$  is obtained by differentiating  $u(x,t)$  with respect to  $x$

$$\epsilon(x,t) = \frac{\partial u}{\partial x} = \frac{\partial}{\partial x} [f(x + ct) + g(x - ct)]$$

or,

$$\epsilon(x,t) = \frac{\partial f(\eta)}{\partial \eta} + \frac{\partial g(\mu)}{\partial \mu} = \frac{1}{c}(v_f - v_g) \quad (\text{A.7})$$

The advantage of using derivatives with respect to  $\eta$  or  $\mu$  becomes apparent since these derivatives express the behavior of the derivative with respect to both  $x$  and  $t$ . Using the rod cross-sectional area  $A$  and taking compressive forces positive, the force  $F(x,t)$  in the wave can be calculated.

$$F(x,t) = -\frac{AE}{c} [v_f(x + ct) - v_g(x - ct)] \quad (\text{A.8})$$

Thus, there exists a simple relation between particle velocity and force in a stress wave; the force is proportional to the velocity by a factor  $AE/c$ . From Equation (A.8) it can be seen that the force will be compressive when the velocities of particles and wave propagation have the same direction and it will be a tension force otherwise.

#### A.4 Boundary Conditions

So far, only the homogeneous differential equation has been considered and nothing has been said about boundary conditions or external forces. In a uniform, elastic rod, where no external forces act, the stress gradient will travel through the rod without being changed in magnitude. In the above derivations an infinite rod was assumed. An important consideration is to deal with what happens if there are any external forces acting along the rod or when a stress wave arrives at the end of a rod. The one dimensional wave equation is linear and superposition

is valid, so that a case of complicated boundary conditions can be split into several basic types of easily solvable problems. If the boundary conditions were nonlinear, then a result can be obtained by assuming piecewise linear boundary conditions and superimposing their effects. A wave reaching the end of the rod might encounter either prescribed force or displacement conditions. This problem can be split into the case where the wave travels in a rod with homogeneous (i.e. zero force or displacement) boundary conditions plus the case where no wave is present with non-zero end forces or displacements. The case where external forces are acting along the rod may also be treated separately and then superimposed onto the homogeneous solution. Prescribed displacements have to be considered at the end of the rod only. Therefore, four basic conditions must be treated:

- Wave approaching a free end
- Wave approaching a fixed end
- Prescribed force acting at a point along the rod
- Prescribed displacement at the end of the rod.

#### A.4.1 Wave Approaching a Free End

Consider Figure A.2a where on the left a stress wave  $\sigma_1(x-ct)$  is shown approaching the free end ( $x=L$ ) of the rod. The condition of zero stress must be maintained at all times at that end. This condition may be satisfied by a second stress wave  $\sigma_2(x+ct)$  propagating towards the left, which, when superposed on the incident wave, cancels the end-section stresses. Expressing this concept mathematically

$$\sigma_{x=L} = 0 = E \frac{\partial f_1}{\partial x}(L - ct) + E \frac{\partial f_2}{\partial x}(L + ct)$$

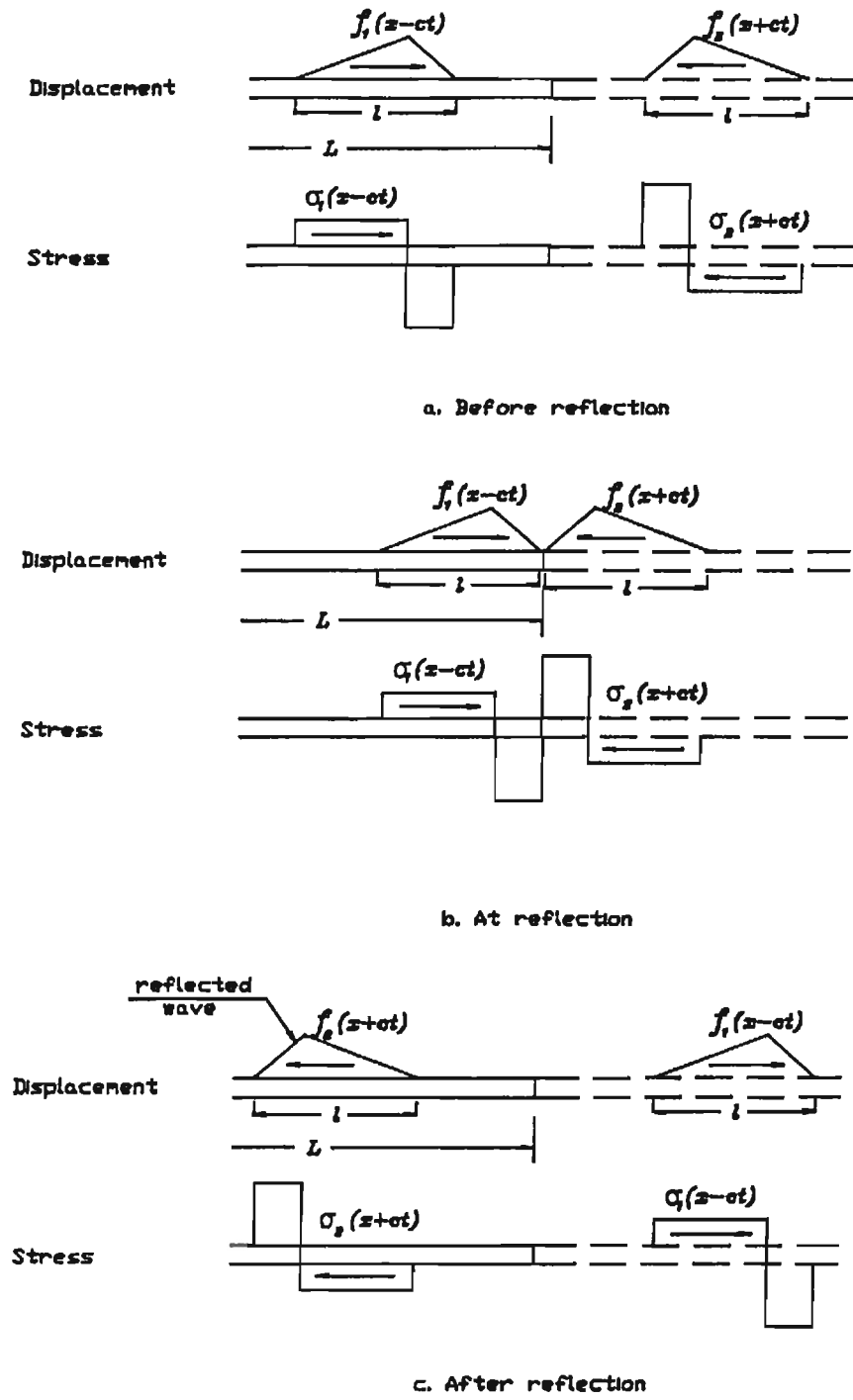


Figure A.2: Reflection of Displacement and Stress Waves at Free End.

from which

$$\frac{\partial f_1}{\partial x}(L - ct) = -\frac{\partial f_2}{\partial x}(L + ct)$$

Hence it is evident that the slope  $\partial u/\partial x$  of the left propagating wave must be the negative of the slope of the forward-propagating wave as each part of the waves passes the end of the rod. The displacement waves shown in Fig. A.2b demonstrate this condition, and the corresponding stress waves show clearly how the stresses at the tip are canceled.

Although the concept of a left-moving wave coming from beyond the end of the rod makes it easier to visualize the mechanism by which the boundary condition is satisfied, it should be understood that this wave actually is created at the end of the bar as the forward-propagating wave reaches that point. In other words, the incident wave is reflected at the free end; the reflected wave has the same deflection as the incident wave, but the stresses are reversed.

#### A.4.2 Wave Approaching a Fixed End

To consider now the case where the right end at the bar is fixed rather than free, the condition of zero displacement must be satisfied. Therefore, the displacement at  $x = L$  can be expressed mathematically as

$$u_{x=L} = 0 = f_1(L - ct) + f_2(L + ct)$$

from which the reflected wave may be expressed in terms of the incident wave as

$$f_2(L + ct) = -f_1(L - ct)$$

Thus the displacement waves in this case are seen to have opposite signs, and by analogy with the preceding discussion it can be inferred that the incident and reflected stress wave have the same sign, as shown in Fig. A.3. Hence, in satisfying the required zero-displacement condition, the reflected wave produces a doubling of stress at the fixed end of the rod.

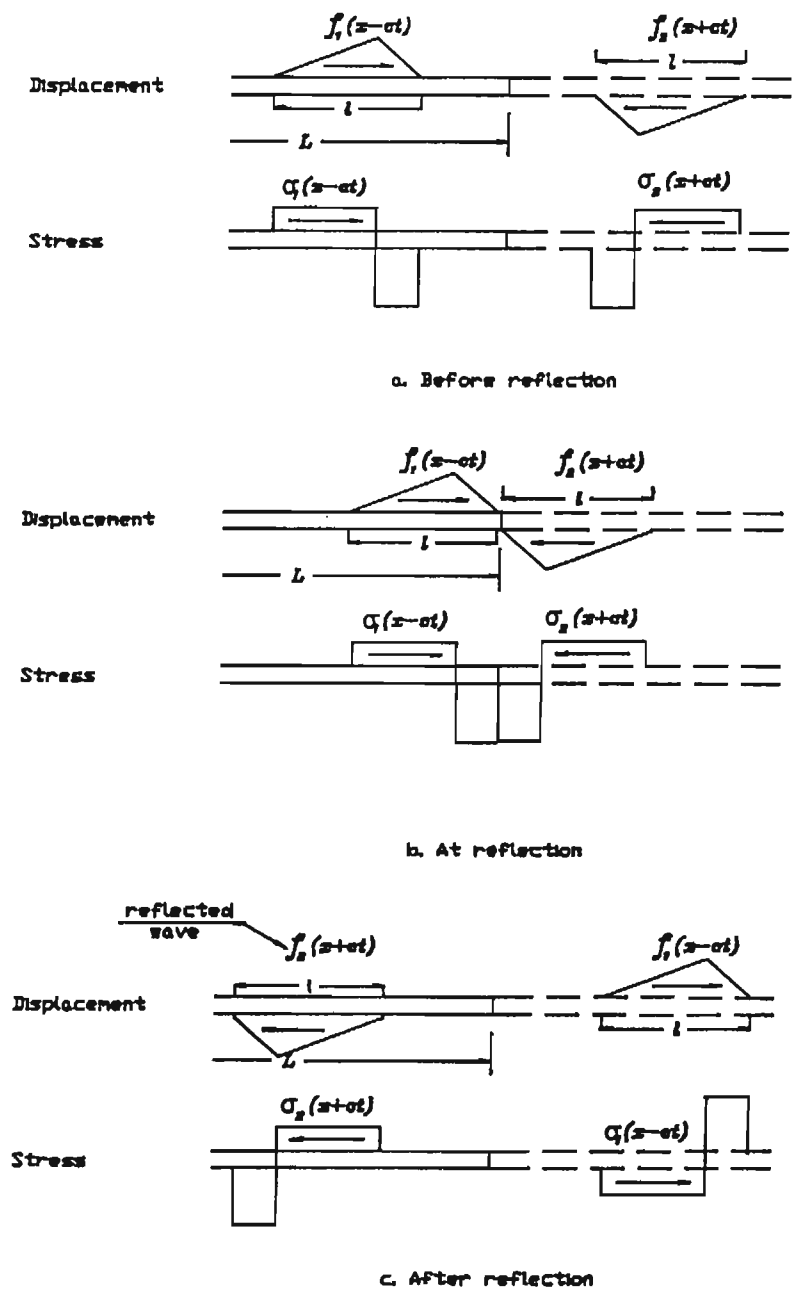


Figure A.3: Reflection of Displacement and Stress Waves at Fixed End.

### A.4.3 Prescribed Force Acting at a Point Along the Rod

If a force is applied at  $x = x'$  along the rod, then the continuity condition requires

$$u(x'_L, t) = u(x'_R, t)$$

where  $x'_L$  and  $x'_R$  are on the left and the right side of the loaded cross-section, respectively (Figure A.4). This can also be written in terms of velocity,

$$\frac{\partial u(x'_L, t)}{\partial t} = \frac{\partial u(x'_R, t)}{\partial t} \quad (\text{A.10})$$

Also the equilibrium condition has to be satisfied, i.e.,

$$AE \left( \frac{\partial u(x'_L, t)}{\partial t} - \frac{\partial u(x'_R, t)}{\partial t} \right) = F_A(x', t) \quad (\text{A.11})$$

where  $F_A(x', t)$  is the applied force at  $x = x'$  and time  $t$ . Now recalling Equations A.6 and A.7, Equations A.10 and A.11 can be satisfied by choosing

$$\left. \frac{\partial f(\eta)}{\partial \eta} \right|_{x=x'_L} = \left. \frac{\partial g(\mu)}{\partial \mu} \right|_{x=x'_R} = \frac{1}{2} F_A(x', t) / EA$$

and

$$\left. \frac{\partial f(\eta)}{\partial \eta} \right|_{x=x'_R} = \left. \frac{\partial g(\mu)}{\partial \mu} \right|_{x=x'_L} = 0$$

Substituting these two conditions in Equation A.10 leads to

$$c \left( \frac{1}{2} F_A(x', t) / EA + 0 \right) = c \left( 0 + \frac{1}{2} F_A(x', t) / EA \right)$$

thus, satisfying the continuity condition.

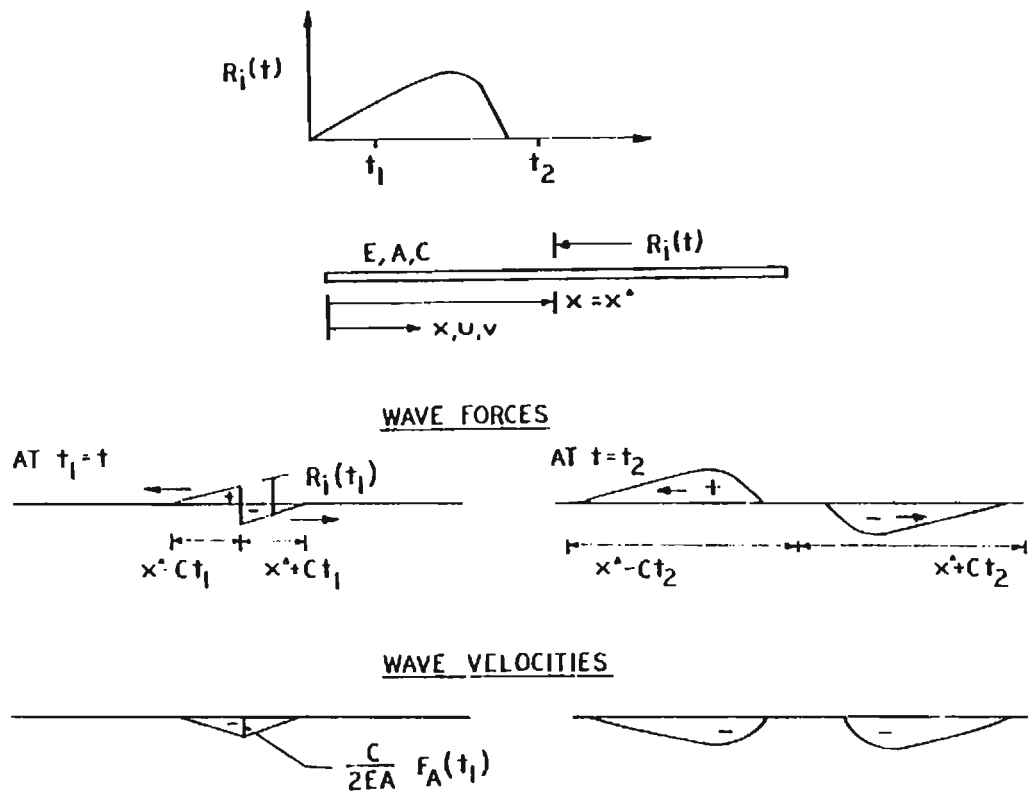


Figure A.4: Impact Force Applied at an Intermediate Point along the rod.

Similarly it proves that the equilibrium condition is satisfied. Figure A.4 shows that both waves carry a force of one-half of the applied force while the velocities are the same in both waves having the same direction as the applied force and magnitude,  $1/2FA(x',t)c/EA$ .

The case where the force is acting at the end of the rod can be deduced since one of the half-waves is immediately reflected and superimposed on the other. Therefore, a wave will travel away from the end with particle velocity,

$$\frac{\partial u(x,t)}{\partial t} = cF_A \left( t - \frac{L-x}{c} \right)$$

and strain

$$\varepsilon(x,t) = \frac{1}{AE} F_A \left( t - \frac{L-x}{c} \right)$$

#### A.4.4 Prescribed Displacements at the End of the Rod

The case of a prescribed displacement condition at a point along the rod will not be discussed since this is equivalent to a rod of shorter length with prescribed end displacement. A displacement prescribed at the end of a rod is equivalent to a prescribed velocity,  $v_A(L,t)$ . From the force-velocity proportionality relation this can be considered a force condition where the force has to be chosen as  $F_A(L,t) = v_A(L,t)EA/c$ . Thus the previous case can be applied.

#### A.5 Superposition of Waves

In this leftline certain special cases will be treated where the findings of the previous sections are applied. These special cases will be needed in treating problems where external forces act along the pile together with prescribed end conditions.

### A.5.1 Free Rod Under Known Velocity at the Top

Suppose a velocity,  $v_t(t)$ , which is zero for  $t < 0$ , is imposed on the top of a rod of length,  $L$ . It is desired to know the top force necessary to maintain this velocity when no other forces are acting along the rod.

As long as the wave created by  $v_t(t)$ , has not yet reached the free end (i.e., for  $t < L/c$ ) a rod particle at a point has velocity,

$$v_i(t) = v_t\left(t - \frac{x_i}{c}\right)$$

At time  $t = L/c$  the wave reaches the free end of the rod and the free end reflection case applies. Thus, a reflection wave having velocities of the same sign and forces of opposite signs will travel back up the rod. The velocity at a station  $x = x_i$  becomes

$$v_i(t) = v_t\left(t - \frac{2L - x_i}{c}\right) + v_t\left(t - \frac{x_i}{c}\right) \quad (\text{A.12})$$

for  $t \leq (2L - x_i)/c$ .

A new reflection wave will be generated when this up-traveling wave reaches the top since here the velocity is prescribed. The case of a fixed end reflection describes this fixed end situation. This second reflection requires a force; therefore, the proportionality between applied velocity and top forces will no longer hold. The force at the top of the free rod may be denoted by  $F_f(t)$ ; then for  $t < 2L/c$ ,

$$F_f(t) = \frac{EA}{c} v_t(t)$$

and for  $2L/c \leq t < 4L/c$

$$F_f(t) = \frac{EA}{c} [v_i(t) - 2v_i(t - \frac{2L}{c})] \quad (\text{A.13})$$

At a time  $t = 3L/c$  the wave will again be reflected at the bottom end. (It had been reflected at the top at time  $2L/c$ ). At time  $t = 4L/c$  the wave has to be reflected again at the top but this time it has the opposite stress due to the previous reflection at the free end. In general, for  $2Lr/c \leq t \leq 2L/c (r+1)$ ,

$$F_f(t) = \frac{EA}{c} \left[ v_i(t) + 2 \sum_{j=1}^r v_i(t - j\frac{2L}{c})(-1)^j \right] \quad (\text{A.14})$$

where  $r = 0,1,2,\dots$ , refers to the time interval considered. Equation A.18 gives the exact solution for a given top velocity and no reaction forces. If this solution is subtracted from the measured force, the Measured Delta curve is obtained as defined in Chapter II.

Equation A.12 gives an expression for the velocity at some point in the rod for times  $t < (2L + x_i)/c$ . The equation can be extended for time  $(2Lr + x_i)/c \leq t < (2L(r + 1) + x_i)/c$ ,  $r = 0,1,2,\dots$ ,

$$v_i(t) = \sum_{j=0}^r (-1)^j \left[ v_i \left( t - \frac{2jL + x_i}{c} \right) - v_i \left( t - \frac{(j + 1)2L - x_i}{c} \right) \right] \quad (\text{A.15})$$

### A.5.2 External Force Acting on a Rod with Fixed Top and Free Bottom

The force denoted by  $R_i(t)$ , is assumed to act upwards. If it is acting at  $x = x_i$ , then the results of Section A.4.3 apply. Thus, two waves are introduced traveling in opposite directions and having particle velocities (at  $x = x_i$ , and time  $t$ ),

$$v_r(t) = -\frac{c}{2EA} R_i(t)$$

The forces in the waves are

$$F_r(t) = \pm \frac{1}{2R(t)}$$

i.e., a compression in the upwards and tension in the downwards traveling wave. The reaction force  $F_{top}(t)$  on the fixed top of the rod due to this velocity will be a compression force of twice the magnitude of the force in the wave. The upwards traveling wave will arrive at the top at a time  $x_i/c$  after it is applied. Hence

$$F_{top}(t) = R_i(t - \frac{x_i}{c})$$

which is valid for a time as long as it takes the initially downwards traveling wave to reach the top after reflection at the bottom. This reflection at the free bottom end causes the initially downwards traveling wave to change the sign in force and therefore, is also a compression wave after reflection. Reaching the top at a time  $(2L-x_i)/c$  after it was generated by the resistance force, this wave also will produce twice the force at the top which it was propagating. The next wave to arrive at the top will be the initially upwards traveling wave, its sign will be converted so that a tension wave arrives.

This way the reaction at the fixed rod top due to  $R_i(t)$  can be calculated for

$$0 \leq t < 4L/c,$$

$$F_{top}(t) = R_i(t - \frac{x_i}{c}) + R_i(t - \frac{2L - x_i}{c}) - R_i(t - \frac{2L + x_i}{c}) - R_i(t - \frac{4L - x_i}{c})$$

For later times it can be observed that all the waves which arrived at a time  $t_i$  at the top have in the meantime changed their sign twice, thus, arriving again with the same sign at a time  $t_i + 4L/c$ . This result can be expected since a pile of length  $L$  has a lowest natural frequency of  $c/4L$ ,

inferring that in the absence of external forces a harmonic behavior can be observed. Therefore, for times  $4rL/c \leq t < (r + 1)4L/c$ ,

$$F_{top}(t) = \sum_{j=0}^r \left[ R_i(t - \frac{x_i}{c} - j\frac{4L}{c}) + R_i(t - \frac{2L-x_i}{c} - j\frac{4L}{c}) \right] \\ \left[ -R_i(t - \frac{2L+x_i}{c} - j\frac{4L}{c}) - R_i(t + \frac{x_i}{c} - (j+1)\frac{4L}{c}) \right] \quad (A.16)$$

and  $r = 0, 1, 2, \dots, n$  indicates the time interval considered.

The problem of obtaining the particle velocities at a point  $x = x_h$  when the load,  $R_i(t)$ , is acting at  $x = x_i$  is somewhat more complicated. It can be split in two parts, first considering the wave which is initially moving upwards and then the wave which is initially moving downwards. Both of these waves have a particle velocity  $-(c/2EA)R_i(t)$ . In order to facilitate the derivation it is further assumed that  $x_h > x_i$ . Then the velocity  $v_{h,up}(t)$  at  $x = x_h$  due to the upwards traveling wave obtains its first contribution after a time  $(x_h + x_i)/c$ , i.e. the time necessary for the wave to reach the top and upon reflection the station  $x = x_h$ . The wave will again be reflected at the bottom end with no sign change in velocities and reach  $x = x_h$  a second time with the same sign in the velocities. Thus, when observing the wave's action at  $x = x_h$  for a time  $t < 4L/c$ ,

$$v_{h,up}(t) = \frac{c}{EA} \left[ R_i(t - \frac{x_h + x_i}{c}) + R_i(t - \frac{2L + x_i - x_h}{c}) \right] \\ \left[ -R_i(t - \frac{2L + x_h + x_i}{c}) - R_i(t - \frac{4L - x_i - x_h}{c}) \right] \quad (A.17)$$

similarly the influence on the velocity at  $x = x_h$  of the initially downwards traveling wave can be determined.

$$v_{h,down}(t) = \frac{c}{2EA} \left[ -R_i(t - \frac{x_h - x_i}{c}) - R_i(t - \frac{2L - x_i - x_h}{c}) \right] \\ \left[ + R_i(t - \frac{2L + x_h - x_i}{c}) + R_i(t - \frac{4L - x_i - x_h}{c}) \right] \quad (A.18)$$

Observing that the waves arrive with the same sign of force and velocity after every  $4L/c$ , then superimposing the results from Equation A.17 and A.18, the velocity  $v_h(t)$  due to  $R_i(t)$  becomes, for  $4rL/c \leq t \leq (r+1)4L/c$ ,

$$v_h(t) = \frac{c}{2EA} \sum_{j=0}^r \left[ R_i(t - \frac{x_h + x_i}{c} - j\frac{4L}{c}) + R_i(t - \frac{2L + x_i - x_h}{c} - j\frac{4L}{c}) \right] \\ - R_i(t - \frac{2L + x_h + x_i}{c} - j\frac{4L}{c}) - R_i(t - \frac{x_i - x_h}{c} - (j+1)\frac{4L}{c}) \\ - R_i(t - \frac{x_h - x_i}{c} - j\frac{4L}{c}) - R_i(t - \frac{2L - x_i - x_h}{c} - j\frac{4L}{c}) \\ \left[ + R_i(t - \frac{2Lx_h - x_i}{c} - j\frac{4L}{c}) + R_i(t - \frac{-x_i - x_h}{c} - (j+1)\frac{4L}{c}) \right]$$

where again  $r = 0,1,2,\dots$ , indicates the time interval considered.

### A.5.3 Free Rod with a Known Force at the Top

In this case a force  $F_A(t)$  is prescribed at the top and no forces act along the rod. It is desired to obtain an expression for the velocity at the rod top  $v_{top}(t)$ , due to this force. The reflections of waves at both ends of the pile have force but no displacement restrictions. Thus, if the applied wave induces compressive strains, then all the reflection waves will have tensile velocities. Reflections will always add to the top velocity on every wave arrival at the top. From proportionality and due to the discussed reflections the result can be readily obtained.

$$v_{top}(t) = \frac{c}{EA} \left[ F_A(t) + 2F_A\left(t - \frac{2L}{c}\right) + 2F_A\left(t - \frac{4L}{c}\right) + \dots \right]$$

or using the notion the above equation can be rewritten to yield for  $2rL/c \leq t \leq (r+1)2L/c$ ,

$$v_{top}(t) = \frac{c}{EA} \left( F_A(t) + 2 \sum_{j=1}^r F_A\left(t - j\frac{2L}{c}\right) \right)$$

#### A.5.4 External Force Acting on a Rod with Free Top and Bottom

The external force may again be denoted by  $R_i(t)$  and act at  $x = x_i$ . The reflections will be of such a nature that the waves arriving at the top always add to the top velocity  $v_{top}(t)$  if  $R_i(t)$  does not change sign. Hence for  $0 \leq t < 2L/c$ ,

$$v_{top}(t) = -\frac{c}{EA} \left[ R_i\left(t - \frac{x_i}{c}\right) + R_i\left(t - \frac{2L - x_i}{c}\right) \right]$$

and for  $2rL/c \leq t \leq (r+1)2L/c$ ,

$$v_{top}(t) = -\frac{c}{EA} \sum_{j=0}^r \left[ R_i\left(t - \frac{x_i}{c} - j\frac{2L}{c}\right) + R_i\left(t - \frac{2L - x_i}{c} - j\frac{2L}{c}\right) \right]$$

#### A.6 Discontinuity in Bar Properties

The wave reflection which takes place at the fixed or free end of a uniform bar may be considered as special cases of general reflection and transmission phenomena occurring at any discontinuity in the bar properties. The conditions of equilibrium and compatibility which must be satisfied at all points along the bar require that additional reflected and refracted waves be generated at the juncture between bars of different properties in response to the action of any

incident wave.

Consider, for example, the juncture between Bars 1 and 2 shown in Fig. A.5. The properties of the bars on each side of the juncture are characterized by their mass per unit length  $\bar{m}$  and axial stiffness  $EA$ . Also, the wave propagation velocity on each side is given by

$$c = \sqrt{\frac{E}{\rho}}$$

A forward propagating wave,  $u_a$ , which arrives at the juncture in Bar 1 is reflected as  $u_b$  which travels in the negative direction in Bar 1, and at the same time creates a refracted wave  $u_c$  which propagates forward in Bar 2.

Continuity and equilibrium conditions are imposed at the juncture:

$$\begin{array}{lll} \text{Displacement:} & u_1 = u_2, & u_a + u_b = u_c \\ \text{Force:} & F_1 = F_2, & F_a + F_b = F_c \end{array}$$

Where the fact that both incident and reflected waves act in Bar 1 has been indicated. Because this continuity condition must always be satisfied

$$\frac{\partial u_a}{\partial t} + \frac{\partial u_b}{\partial t} = \frac{\partial u_c}{\partial t} \quad (\text{A.19})$$

but the incident wave can be expressed in the form

$$u_a = f(x - ct) = f(\eta)$$

Now, the derivatives of  $u_a$  can be expressed as

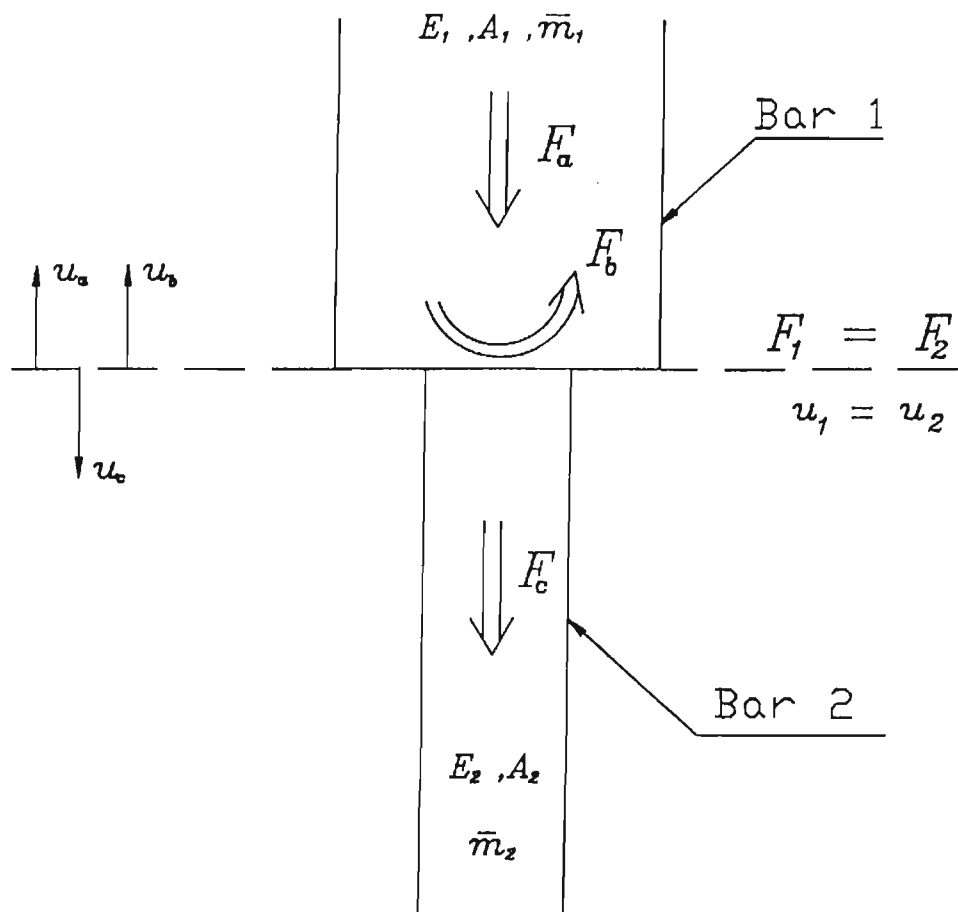


Figure A.5 Wave Reflection and Refraction at Discontinuity.

$$\frac{\partial u_a}{\partial x} = \frac{\partial f}{\partial \eta} \cdot \frac{\partial \eta}{\partial x} = \frac{\partial f}{\partial \eta}$$

$$\frac{\partial u_a}{\partial t} = \frac{\partial f}{\partial \eta} \cdot \frac{\partial \eta}{\partial t} = -c_1 \frac{\partial f}{\partial \eta}$$

from which it is evident that the time and position derivatives are related by the velocity of propagation

$$\frac{\partial u_a}{\partial t} = -c_1 \frac{\partial u_a}{\partial x} \quad (\text{A.20})$$

similarly

$$\frac{\partial u_b}{\partial t} = +c_1 \frac{\partial u_b}{\partial x} \quad (\text{A.21})$$

$$\frac{\partial u_c}{\partial t} = -c_2 \frac{\partial u_c}{\partial x} \quad (\text{A.22})$$

where the positive sign in Eq. A.21 is due to negative direction of the reflected wave.

Substituting Eqs. (A.20), (A.21) and (A.22) into Eq. A.19 yields

$$-c_1 \frac{\partial u_a}{\partial x} + c_1 \frac{\partial u_b}{\partial x} = -c_2 \frac{\partial u_c}{\partial x} \quad (\text{A.23})$$

but the strains

$$\frac{\partial u_a}{\partial x} = \varepsilon_a \quad \text{etc.}$$

can be expressed in terms of forces acting in the bars

$$\epsilon_a = \frac{\sigma_a}{E} = \frac{F_a}{A_1 E_1} \quad \text{etc.}$$

Thus Eq. (1.23) can be expressed as

$$-\frac{c_1}{A_1 E_1} F_a + \frac{c_1}{A_1 E_1} F_b = -\frac{c_2}{A_2 E_2} F_c$$

or more simply

$$F_c = \alpha(F_a - F_b)$$

where

$$\alpha = \frac{c_1 A_2 E_2}{c_2 A_1 E_1}$$

or

$$\alpha = \frac{Z_2}{Z_1}$$

where  $Z_1$  and  $Z_2$  are impedances of Bar 1 and 2 respectively. From which

$$F_b = F_a \left( \frac{\alpha - 1}{\alpha + 1} \right)$$

$$F_c = F_a \left( \frac{2\alpha}{\alpha + 1} \right)$$

These relations show that the transmitted wave always has the same sign as the incident one. The sign of the force in the reflected wave is dependent on the material ratio  $\alpha$ . For a wave approaching a decrease in area,  $\alpha < 1$ , the sign of the reflected stress will be opposite to that of the incident wave. For a wave approaching an increase in area,  $\alpha > 1$ , the opposite condition

will result. For  $\alpha = 1$ , that is, there is no change in relative material constant, there is of course no reflection and the transmitted wave equals the incident. It is here also interesting to note that in the extreme cases when  $\alpha = 0$  or infinity, we have reflection at free and fixed end respectively.

## APPENDIX B

### ACCELEROMETER CALIBRATION FACTOR

#### B.1 Calibration Factor

The EGCS-240D accelerometer consists of four semiconductor strain gages bonded to a simple cantilever beam which is end loaded with a mass (See Figure B.1). The strain gages are connected to make a fully active Wheatstone Bridge. Damping is achieved by using a viscous fluid medium. Under acceleration, the force on the cantilever is created by the acceleration effect on the mass ( $F=ma$ ). The accelerated mass creates a force which in turn provides a bending moment to the beam. This moment creates a strain which results in a bridge unbalance. With an applied voltage, this unbalance produces a voltage deviation at the bridge output, which is proportional to the acceleration vector.

In order to study the effect of the frequency on the accelerometer calibration factor, the accelerometer was modeled as a damped single degree of freedom system of mass  $m$ , stiffness  $k$ , and viscous damping coefficient  $c$ . The model is shown in Figure B.2. If  $x(t)$  is the displacement of the mass  $m$  and  $y(t)$  the displacement of the vibrating body, the equation of motion of  $m$  is

$$m\ddot{x} + c(\dot{x} - \dot{y}) + k(x - y) = 0 \quad (\text{B.1})$$

Letting the relative displacement of the mass  $m$  and the case attached to the vibrating body be  $z = (x - y)$  then,

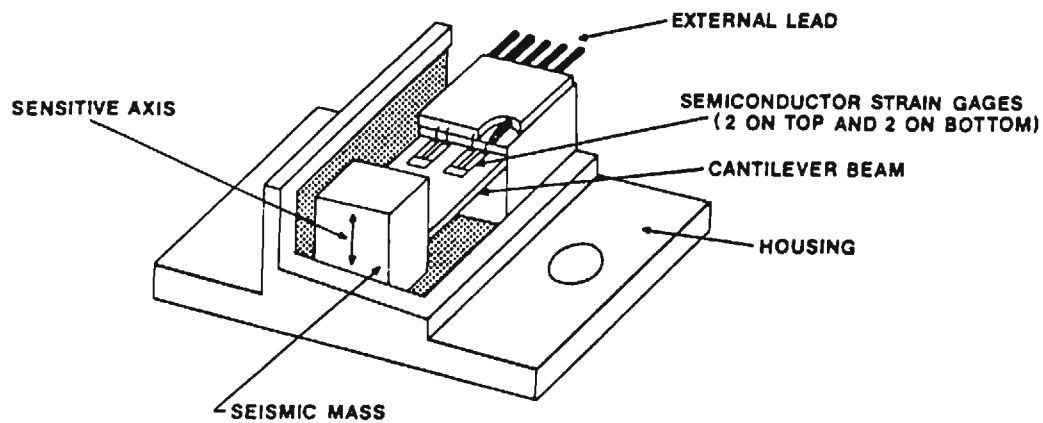


Figure B.1: Entran's EGCS-240D Accelerometer Cutaway.

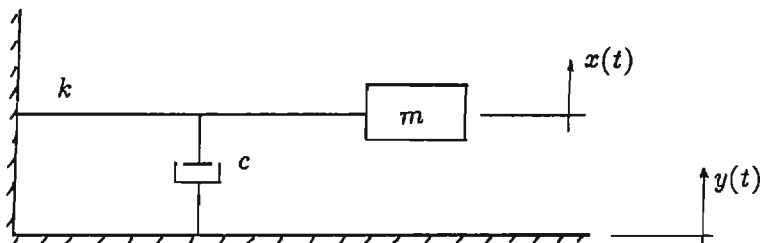


Figure B.2: Accelerometer Model.

$$\dot{z} = (\dot{x} - \dot{y})$$

and

$$\ddot{z} = \ddot{x} - \ddot{y} \quad \text{or} \quad \ddot{x} = \ddot{z} + \ddot{y}$$

Now, by substituting for  $(x - y)$ ,  $(\dot{x} - \dot{y})$  and  $\ddot{x}$  in Eq.(B.1) the following equation of motion is obtained

$$m(\ddot{z} + \ddot{y}) + c\dot{z} + kz = 0$$

or

$$m\ddot{z} + c\dot{z} + kz = -m\ddot{y} \quad (\text{B.2})$$

The motion of the vibrating body is considered to be periodic, then  $y$  can be expressed in terms of Fourier series as

$$y = \sum_{j=1}^{\infty} Y_j e^{i\omega_j t}$$

and therefore,

$$\ddot{y} = - \sum_{j=1}^{\infty} \omega_j^2 Y_j e^{i\omega_j t}$$

substitute for  $y$  in Eq.(B.2)

$$m\ddot{z} + c\dot{z} + kz = m \sum_{j=1}^{\infty} \omega_j^2 Y_j e^{i\omega_j t} \quad (\text{B.3})$$

Equation (B.3) represents the equation of motion of the mass  $m$  with respect to the case of the accelerometer. The steady-state solution of this equation is

$$z = \sum_{j=1}^{\infty} Z_j e^{i\omega_j t}$$

from which,

$$\dot{z} = i \sum_{j=1}^{\infty} \omega_j Z_j e^{i\omega_j t} = i\omega_j z$$

$$\ddot{z} = i^2 \sum_{j=1}^{\infty} \omega_j^2 Z_j e^{i\omega_j t} = -\omega_j^2 z$$

and

$$\sum_{j=1}^{\infty} e^{i\omega_j t} = \frac{z}{Z_j}$$

Substitute for these values in Eq. (B.3) to get

$$-m\omega_j^2 z + ic\omega_j z + kz = m\omega_j^2 \frac{Y_j}{Z_j} z$$

divide by  $mz$

$$-\omega_j^2 + i\frac{c}{m}\omega_j + \frac{k}{m} = \omega_j^2 \frac{Y_j}{Z_j} \quad (\text{B.4})$$

But,

$$\frac{k}{m} = \omega_o^2 \quad \text{and} \quad \frac{c}{m} = 2\xi\omega_o$$

where,  $\omega_o$  is the natural frequency

$\xi$  is the damping ratio

Now, Eq.(B.4) can be rewritten as

$$-w_j^2 + 2i\xi w_o w_j + w_o^2 = w_j^2 \frac{Y_j}{Z_j}$$

divide by  $w_o^2$  and let  $r = w_j / w_o$

$$(1 - r^2) + 2i\xi r = r^2 \frac{Y_j}{Z_j}$$

or

$$\frac{Z_j}{Y_j} = \frac{r^2}{(1 - r^2) + 2i\xi r}$$

multiply the numerator and the denominator by  $\{(1 - r^2) - 2i\xi r\}$  and arrange we get

$$\frac{Z_j}{Y_j} = \frac{r^2(1 - r^2)}{(1 - r^2)^2 + (2\xi r)^2} - i \frac{2\xi r^3}{(1 - r^2)^2 + (2\xi r)^2}$$

or

$$\frac{Z_j}{Y_j} = A + iB$$

where,

$$A = \frac{r^2(1 - r^2)}{(1 - r^2)^2 + (2\xi r)^2}$$

$$B = -\frac{2\xi r^3}{(1 - r^2)^2 + (2\xi r)^2}$$

$Z_j$  and  $Y_j$  are both complex numbers, then the ratio of their magnitude is

$$\frac{\bar{Z}_j}{\bar{Y}_j} = \left| \frac{z_j}{y_j} \right| = \sqrt{A^2 + B^2} = \frac{r^2}{\sqrt{(1 - r^2)^2 + (2\xi r)^2}}$$

Therefore,

$$\bar{Z}_j = \frac{r^2 \bar{Y}_j}{\sqrt{(1 - r^2)^2 + (2\xi r)^2}} = R r^2 \bar{Y}_j = \frac{R w_j^2 \bar{Y}_j}{w_o^2} \quad (\text{B.5})$$

where,

$$R = \frac{1}{\sqrt{(1 - r^2)^2 + (2\xi r)^2}}$$

$w_j^2 \bar{Y}_j$  is the amplitude of the acceleration of the vibrating body and  $w_o^2$  is constant because  $w_o$  is a property of the system; therefore the relative motion  $z$  is proportional to the acceleration  $y$  if the magnification factor  $R$  is constant for all ranges of operation.

A periodic vibration generally has a number of harmonic components, each of which gives a corresponding value of  $r$ . Amplitude distortion occurs if the magnification factor  $R$  changes with the harmonic components. It is evident then that the parameters involved are the frequency ratio  $r$  and the damping factor  $\xi$ . Figure B.3 shows a plot of  $R$  for various values of damping ratio  $\xi$ . The diagram shows that the useful frequency range of the undamped accelerometer is somewhat limited. However, with  $\xi = 0.7$  the useful frequency range is  $0 \leq w/w_n \leq 0.2$  with a maximum error less than 0.01 percent.

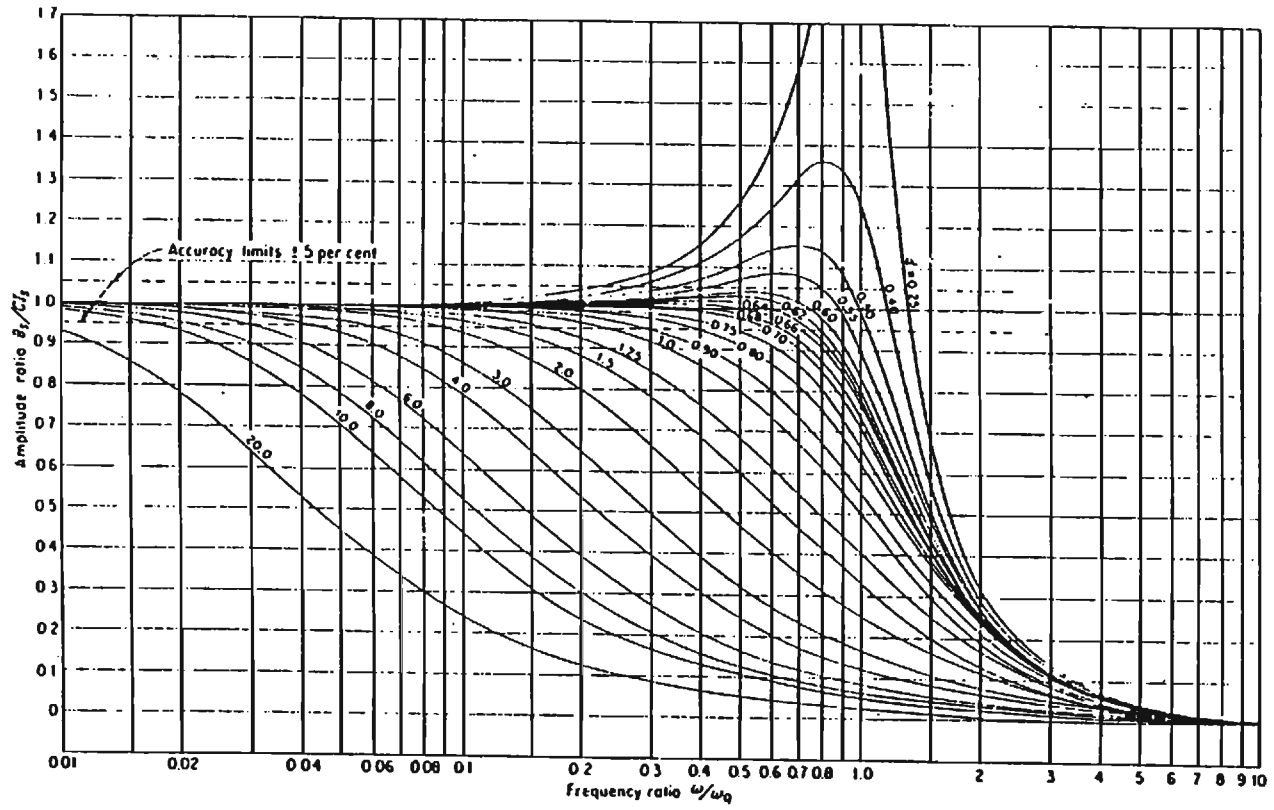


Figure B.3: Plot of the Magnification Factor  $R$  for Various Values of the Damping Ratio  $\xi$ .

## B.2 Correction

When the frequency of the vibrations to be measured is higher than that of the useful frequency of the accelerometer, the magnification factor  $R$  becomes a nonlinear function in the frequency ratio  $r$ . Thus, the relative motion  $z$  becomes non-linearly proportional to the acceleration.

To get the actual acceleration of the vibrating body a different procedure must be used. The measured displacement  $z$  is a complex function in  $t$  and by using Fast Fourier Transform (FFT), it can be transferred to another complex function in  $\omega_j$ . For each value of  $\omega_j$  the magnification factor  $R$  can be evaluated and then the acceleration can be computed from Eq.(2.5)

$$\ddot{y}_j(\omega_j) = \frac{Z_j(\omega_j)}{R_j(\omega_j)} \quad j = 1 \quad \text{to} \quad N$$

where,  $N$  is the number of sampling points.

Now, the acceleration can be transferred to the time domain using inverse Fast Fourier Transform. The results are in complex form, but the interest is in the magnitude which is the real values.